



**Fabrication and Characterization of Bioactive Ceramic Materials for  
Bone Tissue Applications**

**Hnin Nandar Soe**

**A Thesis Submitted in Fulfillment of the Requirements for the  
Degree of Doctor of Philosophy in Mining and Materials Engineering  
Prince of Songkla University**

**2023**

**Copyright of Prince of Songkla University**



**Fabrication and Characterization of Bioactive Ceramic Materials for  
Bone Tissue Applications**

**Hnin Nandar Soe**

**A Thesis Submitted in Fulfillment of the Requirements for the  
Degree of Doctor of Philosophy in Mining and Materials Engineering  
Prince of Songkla University  
2023**

**Copyright of Prince of Songkla University**

**Thesis Title**            Fabrication and Characterization of Bioactive Ceramic  
Materials for Bone Tissue Applications  
**Author**                    Miss Hnin Nandar Soe  
**Major Program**        Mining and Materials Engineering

---

**Major Advisor**

.....  
(Assoc. Prof. Dr. Matthana Khanghamano)

**Examining Committee :**

.....Chairperson  
(Assoc. Prof. Dr. Weerachai Sangchay)

**Co-advisor**

.....  
(Assoc. Prof. Dr. Jirut Meesane)

.....Committee  
(Assoc. Prof. Dr. Matthana Khanghamano)

.....Committee  
(Assoc. Prof. Dr. Jirut Meesane)

.....Committee  
(Asst. Prof. Dr. Vishnu Rachpech)

.....Committee  
(Assoc. Prof. Dr. Somjai Janudom)

The Graduate School, Prince of Songkla University, has approved this thesis as fulfillment of the requirements for the Doctor of Philosophy Degree in Mining and Materials Engineering.

.....  
(Asst. Prof. Dr. Kawinbhat Sirikantisophon)  
Acting Dean of Graduate School

This is to certify that the work here submitted is the result of the candidate's own investigations. Due acknowledgement has been made of any assistance received.

.....Signature  
(Assoc. Prof. Dr. Matthana Khanghamano)  
Major Advisor

.....Signature  
(Assoc. Prof. Dr. Jirut Meesane)  
Co-advisor

.....Signature  
(Hnin Nandar Soe)  
Candidate

I hereby certify that this work has not been accepted in substance for any degree, and is not being currently submitted in candidature for any degree.

.....Signature  
(Hnin Nandar Soe)  
Candidate

<b>Thesis Title</b>	Fabrication and Characterization of Bioactive Ceramic Materials for Bone Tissue Applications
<b>Author</b>	Miss Hnin Nandar Soe
<b>Major Program</b>	Mining and Materials Engineering
<b>Academic Year</b>	2023

## ABSTRACT

Carbon-based nanomaterials, including carbon nanotubes, graphene, and carbon dots, have emerged as promising candidates for applications in bone tissue regeneration and engineering due to their benefits of being light weight, mechanical stability, and remarkable ability for bone repair. However, their toxicity and dispersity are the most significant concern and greatly limiting their suitability for clinical applications. In this thesis, the surface modification of carbon black particles (CBs) based on core-shell structure design as promising candidate materials for bone tissue engineering applications has been fabricated. This work not only focuses on the synthesis of TiC/TiO<sub>2</sub>/SrCO<sub>3</sub>-coated carbon black particles through molten-salt synthesis and hydrothermal processes, but also the fabrication of a porous structure of mixed oxide phases with titanium carbide on CBs through molten-salt synthesis and calcination at various temperatures. The main objective of this study was to investigate the effect of temperature on crystal structure, morphologies, surface wettability, and biological functions of the prepared particles. Phase compositions and morphologies were characterized by X-ray diffraction (XRD), energy-dispersive X-ray spectroscopy (EDX), and field-emission scanning electron microscope (FE-SEM). Core-shell structure was observed by transmission electron microscope (TEM). Furthermore, the biological properties of as-synthesized bioceramic particles were evaluated using the osteoblast (MG-63) cell line. Cell viability, cell proliferation, alkaline phosphatase activity (ALP), calcium deposition, and protein synthesis of the particles were assessed to gain insights into the interactions between the particles and bone cells. The results demonstrated that reaction temperature played a pivotal role in determining the bioactive properties of the synthesized bioceramic particles. Specifically, increased

hydrothermal and thermal treatment temperatures lead to enhanced crystallite size, surface roughness, wettability, and biological functions of the as-synthesized particles. In addition, the investigation pointed that the development of novel and improved bioceramic materials with enhanced bioactivity not only results in more effective treatments for bone defects but also contributes significantly to the advancement of regenerative approaches in bone tissue engineering applications.

## ACKNOWLEDGEMENTS

I am profoundly grateful to the individuals who provided invaluable support throughout my Ph.D. journey. I extend my sincere appreciation to my advisor, **Assoc. Prof. Dr. Matthana Khangkhamano**, whose unwavering inspiration and invaluable guidance have been instrumental in the completion of this study. Her insightful suggestions and advice have played a vital role in shaping this thesis. Without her exceptional mentorship, limitless patience, and unwavering encouragement throughout the entire year, the successful completion of this thesis would not have been possible. I am immensely grateful to **Assoc. Prof. Dr. Jirut Meesane** for his unwavering support, guidance, and co-supervision throughout the entire duration of my thesis research. His kind assistance, valuable advice, thought-provoking discussions, thorough explanations, and expert guidance have been indispensable in the successful completion of this thesis. Without his continuous support, this research endeavor would not have been possible.

I would also like to extend my gratitude to **Asst. Prof. Dr. Rungrote Kokoo** for his kindness and assistance throughout my thesis journey. His support and input have been invaluable in shaping the direction of my research and overcoming various challenges along the way. Furthermore, I express my appreciation to my dissertation committee members, **Assoc. Prof. Dr. Weerachai Sangchay**, **Asst. Prof. Dr. Vishnu Rachpech**, and **Assoc. Prof. Dr. Somjai Janudom** for their helpful advice and being an integral part of my committee. Their expertise and insights have significantly enriched the quality of my work.

I would also like to extend my heartfelt thanks to all the teachers in my department for their continuous support, knowledge sharing, and encouragement. Their expertise and dedication have played a significant role in shaping my academic journey. Additionally, I would like to express my gratitude to **Dr. Supaporn Sangkert** from the faculty of medicine for her kind instruction in the field of biological testing.

A special thanks to my parents and my younger sister for their love, support, and encouragement throughout my academic journey. Their constant presence, understanding, and belief in my abilities have been a source of strength and motivation.

I would like to extend my sincere gratitude to **Miss. Benjaporn Nooklay** and the technicians at the scientific equipment center for their invaluable assistance in conducting XRD, FE-SEM, and TEM characterizations. Their expertise and technical support have been instrumental in obtaining accurate and valuable data for my research.

I am profoundly thankful to the National Science, Research and Innovation Fund (NSRF), the faculty of engineering, the faculty of medicine, and the Graduate School at Prince of Songkla University for their financial support. Additionally, I am sincerely grateful to my dear friends for their support throughout my academic endeavors. Their contributions have played a significant role in shaping my Ph.D. experience and have been instrumental in my personal and professional growth.

Miss Hnin Nandar Soe

## CONTENTS

	<b>Page</b>
COVER	i
APPROVAL PAGE	ii
CERTIFICATE OF ORIGINAL WORK	iii
CERTIFICATE OF THESIS FOR SUBMIT PH.D. DEGREE	iv
ABSTRACT	v
ACKNOWLEDGEMENT	vii
CONTENTS	ix
LIST OF TABLES	xii
LIST OF FIGURES	xiii
LIST OF ABBREVIATIONS AND SYMBOLS	xv
LIST OF PAPERS	xvii
PERMISSION FROM PUBLISHERS	xviii
1. INTRODUCTION	1
2. OBJECTIVES	4
3. SIGNIFICANT RESULTS AND DISCUSSION	5
3.1 TiC/ TiO <sub>2</sub> /SrCO <sub>3</sub> coating on carbon black particles	5
3.1.1 Preparation of TiC/ TiO <sub>2</sub> /SrCO <sub>3</sub> coating on carbon black particles	5
3.1.2 Phase composition and crystallinity of core-shell composite particles	6

3.1.3	Structural study of core-shell composite particles	8
3.1.4	Wettability measurement of the core-shell composite particles	10
3.2	Biological functions of core-shell composite particles	11
3.2.1	Cell proliferation	11
3.2.2	Cell viability	12
3.2.3	Calcium deposition	15
3.3	Core-shell porous mixed oxide phases with TiC coating on CBs	16
3.3.1	Preparation of core-shell porous mixed oxide phases with TiC coating on CBs	16
3.3.2	Phase composition and crystallinity of core-shell porous particles	17
3.3.3	Structural study of core-shell porous particles	18
3.3.4	Wettability measurement of core-shell porous particles	20
3.4	Biological functions of core-shell porous particles	22
3.4.1	Cell proliferation	22
3.4.2	Protein synthesis	23
3.4.3	ALP activity	24
3.4.4	Calcium deposition	25
4.	CONCLUSIONS	26
4.1	Core-shell structure of TiC/TiO <sub>2</sub> /SrCO <sub>3</sub> coating on carbon black particles	26

4.2	Core-shell porous bioactive compound of mixed oxide phases with TiC on carbon black particles	27
4.3	Conclusion remarks	28
5.	BIBLIOGRAPHY AND REFERENCES	29
	APPENDIX I – PUBLICATION 1	36
	APPENDIX II – PUBLICATION 2	50
	APPENDIX III –EXPERIMENTAL PROCEDURES AND MECHANISM	66
	VITAE	70
	LIST OF PUBLICATIONS	71

**LISTS OF TABLES**

<b>Table 1</b>	Sample ID and synthesis conditions	6
<b>Table 2</b>	Phase composition, crystallite size, and surface roughness of the samples	10
<b>Table 3</b>	Sample ID and fabricating conditions	17
<b>Table 4</b>	The crystalline size, surface roughness and contact angle measurement of the samples	21

## LISTS OF FIGURES

<b>Figure 1</b>	XRD results of (a) as-received CBs, (b) TCBs, (c) HT180, (d) SrHT180, (e) SrHT200, (f) SrHT225, and (g) SrHT250	7
<b>Figure 2</b>	FE-SEM images of (a) as-received CBs, (b) TCBs, (c) HT180, (d) SrHT180, (e) SrHT200, (f) SrHT225, and (g) SrHT250	9
<b>Figure 3</b>	Contact angle measurements of bare CBs, TiC coating on CBs (TCBs), and hydrothermally treated samples at various temperatures. The insets FE-SEM images show the surface features of the samples	11
<b>Figure 4</b>	Cell proliferation of samples after measured with PrestoBlue® on day 1, 3, 5 and 7	12
<b>Figure 5</b>	Cell viability on the samples after day 1 and 5	14
<b>Figure 6</b>	Calcium deposition of samples on day 7, 14 and 21	15
<b>Figure 7</b>	XRD results of the samples; (a) CBs, (b) TCBs, (c) TCBs100, (d) TCBs150, (e) TCBs200, and (f) TCBs250	18
<b>Figure 8</b>	FE-SEM images of the samples; (a) CBs, (b) TCBs, (c) TCBs100, (d) TCBs150, (e) TCBs200, and (f) TCBs250	20
<b>Figure 9</b>	TEM images of TCBs250: at magnification of (a) 25 000x and (b) 100 000x. The insert in (a) is SAED pattern of particles	20
<b>Figure 10</b>	Cell proliferation of the samples measured with PrestoBlue® on day 1, 3, 5 and 7	22

<b>Figure 11</b>	Protein synthesis of the samples on day 7, 14 and 21	23
<b>Figure 12</b>	ALP activity of the samples on day 7, 14, and 21	24
<b>Figure 13</b>	Calcium deposition of samples on day 7, 14 and 21	25
<b>Figure 14</b>	Schematic diagram of sample preparation procedure via molten salt synthesis method	67
<b>Figure 15</b>	Schematic diagram of sample preparation procedure by hydrothermal method	67
<b>Figure 16</b>	Schematic diagram of formation mechanism of the core-shell TiC/TiO <sub>2</sub> /SrCO <sub>3</sub> -coated CBs via molten salt synthesis method and hydrothermal treatment	68
<b>Figure 17</b>	Schematic diagram of sample preparation procedure via calcination	69
<b>Figure 18</b>	Schematic diagram of formation mechanism of core-shell porous mixed oxide phases with TiC on CBs via calcination	69

**LIST OF ABBREVIATIONS AND SYMBOLS**

°C	Degree Celsius
μl	Microliter
g	Gram
s	second
min	minute
h	hour
%	Percentage
mg/ml	Milligram/ milliliter
mm	Millimeter
nm	Nanometer
CBs	Carbon Black Particles
TiC	Titanium Carbide
TCBs	Titanium Carbide-Coated Carbon Black Particles
MSS	Molten Salt Synthesis
XRD	X-Ray Diffraction
SEM	Scanning Electron Microscope
FE-SEM	Field Emission Electron Microscopy
TEM	Transmission Electron Microscopy
EDX	Energy Dispersive X-Ray Spectroscopy
CA	Contact Angle

OD	Optical Density
OS	Osteogenic Supplement
FDA	Fluorescein Diacetate
PBS	Phosphate-Buffered Saline
ALP	Alkaline Phosphatase Activity

## LIST OF PAPERS

This thesis is based on the following papers:

- Paper 1.** Soe, H.N., Meesane, J, Kokoo, R, Khangkhamano, M. Bioactive core–shell structure of TiC/TiO<sub>2</sub>/SrCO<sub>3</sub> coating on carbon black particles for bone tissue formation: Fabrication, characterization, and biological functions. J Am Ceram Soc; Vol. 106: pp. 2689-2701, 2023. <https://doi.org/10.1111/jace.18942>
- Paper 2.** Soe, H.N., Khangkhamano, M., Meesane, J. et al. A material-based core–shell bioactive compound of mixed oxide phases with TiC on carbon black particles for bone augmentation in oral and maxillofacial surgery. Journal of Materials Research; Vol. 38: pp. 3504–3518, 2023. <https://doi.org/10.1557/s43578-023-01074-x>

## PERMISSION FROM PUBLISHERS

7/9/23, 8:56 PM

Gmail - Thank you for your order with RightsLink / John Wiley and Sons



Hnin Nandar Soe &lt;muethit1991@gmail.com&gt;

---

### Thank you for your order with RightsLink / John Wiley and Sons

1 message

---

**no-reply@email.copyright.com** <no-reply@email.copyright.com>  
To: muethit1991@gmail.com

Fri, Jun 2, 2023 at 2:00 PM



### Thank you for your order!

Dear Miss. Hinn Nandar Soe,

Thank you for placing your order through Copyright Clearance Center's RightsLink® service.

#### Order Summary

Licensee: Department of Mining and Materials Engineering, Faculty of Engineering,  
Prince of SONGKLA University  
Order Date: Jun 2, 2023  
Order Number: 5560640475341  
Publication: Journal of the American Ceramic Society  
Bioactive core-shell structure of TiC/TiO<sub>2</sub>/SrCO<sub>3</sub> coating on carbon black  
particles for bone tissue formation: Fabrication, characterization, and  
biological functions  
Title: Bioactive core-shell structure of TiC/TiO<sub>2</sub>/SrCO<sub>3</sub> coating on carbon black  
particles for bone tissue formation: Fabrication, characterization, and  
biological functions  
Type of Use: Dissertation/Thesis  
Order Total: 0.00 USD

(Original Order Number: 501820198)

View or print complete details of your order and the publisher's terms and conditions.

Sincerely,

Copyright Clearance Center

7/9/23, 8:55 PM

Gmail - Thank you for your order with RightsLink / Springer Nature



Hnin Nandar Soe &lt;muethit1991@gmail.com&gt;

---

**Thank you for your order with RightsLink / Springer Nature**

1 message

---

**no-reply@email.copyright.com** <no-reply@email.copyright.com>  
To: muethit1991@gmail.com

Sun, Jul 9, 2023 at 8:45 PM

**SPRINGER NATURE****Thank you for your order!**

Dear Miss. Hinn Nandar Soe,

Thank you for placing your order through Copyright Clearance Center's RightsLink® service.

**Order Summary**

Licensee: Department of Mining and Materials Engineering, Faculty of Engineering,  
Prince of SONGkla Universtiy  
Order Date: Jul 9, 2023  
Order Number:5584800574261  
Publication: Journal of Materials Research  
Title: A material-based core-shell bioactive compound of mixed oxide phases  
with TiC on carbon black particles for bone augmentation in oral and  
maxillofacial surgery  
Type of Use: Thesis/Dissertation  
Order Total: 0.00 USD

View or print complete [details](#) of your order and the publisher's terms and conditions.

Sincerely,

Copyright Clearance Center

customer@copyright.com  
<https://myaccount.copyright.com>



## 1. INTRODUCTION

All over the world, a number of patients suffer from bone defects due to delayed implant replacement after tooth loss, trauma, cysts, caries, tumor resection, and various other disorders [1-2]. In severe cases, patients require treatment with the use of bioactive materials or implants, to enhance bone healing. Different types of biomaterials have been used to treat bone injuries, including metals, polymers, and ceramic materials [3]. Nevertheless, their clinical applications have been limited. For example, metals/alloys can lead to the extended release of ions during prolonged usage, potentially causing allergic reactions and adverse responses due to corrosion-related problems [4]. Biopolymers have appropriate fixation, but they are likely to release monomers when implanted due to the degradation of implants [5]. Bioactive ceramics, including hydroxyapatite (HA), beta-tricalcium phosphate ( $\beta$ -TCP), and bioactive glasses, are commonly employed for bone regeneration [6-7].  $\beta$ -TCP has been recognized as a suitable material for promoting bone formation and replacement when utilized as a bone implant material [8]. However, certain studies have indicated that  $\beta$ -TCP alone may not effectively stimulate sufficient bone growth [9-10]. HA exhibits greater biocompatibility and stability within bone tissue when compared to  $\beta$ -TCP [11]. Yet, HA has limitations in terms of its capacity for remodeling, making it unsuitable as a bone defect treating material for bone healing [12]. On the other hand, some investigations have reported that bioactive glasses demonstrate superior osteoconductive properties, contributing to bone regeneration [13-14]. Nonetheless, the notable lack of resorption of bioactive glasses represents a drawback in their use for bone regeneration [15].

In recent years, there has been a growing interest in utilizing various carbon-based materials, including carbon nanotubes, graphene, and carbon dots, for applications in bone tissue engineering [16]. These materials possess unique structures and properties such as excellent mechanical strength, adjustable surface functionalities, high biocompatibility, and commercial availability. Consequently, they offer remarkable potential for bone tissue regeneration, cell proliferation, and osteogenic differentiation.

While carbon black particles (CBs) have been extensively studied as a representative carbonaceous toxicant in air pollution research and have shown size-dependent effects on in vitro cultures [17], their use in bone tissue engineering remains uncertain. Ultrafine CBs with sizes below 100 nm have been found to exhibit toxicity and pose potential risks to various biological systems, leading to adverse health effects including respiratory, lung diseases, allergic immune responses, and vascular effects [18-24]. The toxic nature of nanoscale CBs can be attributed to their high surface area, surface reactivity, and ability to adsorb toxic substances.

The effects of nanosized CBs on bone health and osteogenesis are not well understood, and only a limited number of studies have been reported in this area. For example, Shen et al. [25] examined the impact of nanosized CBs on the osteogenesis of mesenchymal stem cells (MSCs) and found that CBs inhibited osteogenic differentiation, reduced alkaline phosphatase activity, and disrupted mitochondrial fusion and fission during osteogenesis. Furthermore, the dispersion of CBs in liquid media posed challenges due to their high aggregation and poor wettability. Similarly, Kim et al. [26] investigated the dispersion of CBs in various solutions, including distilled water, Krebs-Ringer solution (KR), physiological salt solution (PSS), and biological buffer solutions such as cell culture media and blood plasma. Their results revealed that nanosized CBs exhibited a higher degree of agglomeration and incomplete dispersion in KR, PSS, and biological buffer solutions compared to larger-sized particles. Moreover, Sahu et al. [27] demonstrated that nano-sized CBs (~50 nm) induced greater toxicity and inflammatory responses in human monocytes compared to micron-sized CBs (~500 nm). These findings underscore the need for further exploration of the effects of nanosized CBs on bone health and osteogenesis, as well as addressing challenges related to their dispersion and aggregation in liquid media.

Based on findings, nanosized CBs elicit a more pronounced inflammatory response compared to coarse ones. However, those carbon black particles were used in the forms of both nanoscale and bare surfaces, which were found to be highly aggregated, poorly dispersed, and exhibited high surface reactivity and toxicity. In this study, submicron CBs with surface modification were used to minimize those adverse effects on wettability and biological systems as well as to create lightweight bioactive

materials as reinforcing agents for bone tissue engineering applications. This thesis focuses on the surface modification of CBs and is divided into two main parts. The first part involves the designation of a coating layer composed of a TiC/TiO<sub>2</sub>/SrCO<sub>3</sub> nanocomposite. This nanocomposite is coated onto CB surfaces using molten salt synthesis (MSS), followed by hydrothermal process at various temperatures. The second part focuses on core-shell porous mixed oxide phases containing TiC on CBs. This is achieved through MSS and calcination at different temperatures. The presence of multiphases on CBs could enhance both physical and biological properties. Moreover, TiC could improve surface wettability, hardness, wear resistance, compressive strength, biocompatibility, and osseointegration [29]. On the other hand, mixed oxides (TiO<sub>2</sub>, Ti<sub>2</sub>O<sub>3</sub>, Ti<sub>3</sub>O<sub>5</sub>) provide biocompatibility, low cytotoxicity, stability in body fluids, and corrosion resistance, favorable molecular response, and osseointegration [30-31]. SrCO<sub>3</sub> enhances bioactivity, biocompatibility, bone repair, and the formation of new bone [32]. Furthermore, porous shell layer promotes bone tissue regeneration, and integration with the surrounding bone tissue [33-34]. Interestingly, there are only a few studies focusing on the fabrication of core-shell structure with multiphases coating on CBs for bone regeneration. The aim of this work is therefore to create such structured particles and to investigate the effect of temperature on phase composition, crystal structure, morphologies, surface roughness, wettability, and biological functions of the fabricated particles for bone tissue engineering applications.

## 2. OBJECTIVES

1. To prepare core-shell structure of TiC/TiO<sub>2</sub>/SrCO<sub>3</sub> coating on carbon black particles via molten salt synthesis and hydrothermal process at different temperatures.
2. To fabricate core-shell porous structure of mixed oxide phases with TiC on carbon black particles by molten salt synthesis and calcination at different temperatures.
3. To investigate the effect of temperature on crystal structure, phase composition, morphologies, surface roughness, wettability, and biological functions of the prepared particles for bone tissue engineering applications.

### 3. SIGNIFICANT RESULTS AND DISCUSSION

#### 3.1 TiC/ TiO<sub>2</sub>/SrCO<sub>3</sub> coating on carbon black particles

The study on this topic, including the experimental details and the discussion of the significant results, is presented in the form of an academic article that has been published in Journal of American Ceramic Society, Volume 106, Pages. 2689-2701 as attached in Appendix A. The significant results are phase composition, morphology, wettability measurement, and biological functions of the core-shell composite particles as follows.

##### 3.1.1 Preparation of TiC/ TiO<sub>2</sub>/SrCO<sub>3</sub> coating on carbon black particles

TiC-coated carbon black particles (TCBs) were prepared via molten salt synthesis. Ti powders were mixed with CBs in a molar ratio of 1:8. The resulting mixture was then combined with potassium chloride (KCl) in an agitate mortar. Next, the mixture was transferred to an alumina crucible and covered with a lid. The crucible was placed inside an alumina-tube furnace, and fired at 900°C for 4 h in an argon protected atmosphere with heating and cooling rates of 3°/min. Once the furnace cooled down, the solidified mass was repeatedly washed with distilled water, to remove residual salt, and then oven-dried overnight. The sample gained from this process was designated as TCBs.

The TCBs were used as a raw material for fabricating TiC/TiO<sub>2</sub>/SrCO<sub>3</sub> on carbon black particles via hydrothermal process. As-synthesized TCB powder of 0.5 g was loaded into a 0.1M (SrNO<sub>3</sub>)<sub>2</sub> solution and sonicated for 15 min to obtain a homogeneous suspension. The suspension was loaded into a Teflon container (10 ml volume), placed in an autoclave reactor, sealed tightly, and heated to 180, 200, 225, and 250°C for 2 h. The samples were filtrated and thoroughly washed with distilled water prior to drying in an oven. All samples were labelled according to reaction temperature as presented in Table 1. The obtained samples were used for characterization, contact angle and biological properties test.

**Table 1** Sample ID and synthesis conditions.

Samples	Details
CBs	As-received carbon black particles
TCBs	TiC-coated carbon black particles via molten salt synthesis at 900°C for 4 h
HT180	Hydrothermally treated TCBs in distilled water at 180°C
SrHT180	Hydrothermally treated TCBs in a 0.1M (SrNO <sub>3</sub> ) <sub>2</sub> solution at 180°C
SrHT200	Hydrothermally treated TCBs in a 0.1M (SrNO <sub>3</sub> ) <sub>2</sub> solution at 200°C
SrHT225	Hydrothermally treated TCBs in a 0.1M (SrNO <sub>3</sub> ) <sub>2</sub> solution at 225°C
SrHT250	Hydrothermally treated TCBs in a 0.1M (SrNO <sub>3</sub> ) <sub>2</sub> solution at 250°C
Control	Agarose hydrogel solution without particles

### 3.1.2 Phase composition and crystallinity of core-shell composite particles

Phase identification and crystallinity of the product powders were examined by X-ray diffraction (XRD, X'Pert MPD, PHILIPS, Netherlands). Figure 1 shows XRD patterns of as-received CBs and as-prepared samples of TCBs, HT180, SrHT180, SrHT200, SrHT225, and SrHT250. Two broad peaks of C phase (ICDD card 00-041-1487) were observed, without any other impurity phases, on the uncoated CBs at  $2\theta = 25.18^\circ$  and  $43.5^\circ$  attributing to an amorphous nature of as received CB particles (Figure 1a). After MSS, the presence of TiC (ICDD card 01-076-7070) and carbon (C) phases was identified (Figure 1b). Notably, no unreacted titanium (Ti) or intermediate phases were detected, indicating the successful and complete formation of TiC through the molten salt synthesis method. After hydrothermal treatment of TCBs with and without Sr(NO<sub>3</sub>)<sub>2</sub>, additional phases were observed based on the synthesis temperature. At 180°C, TiC was the major phase, accompanied by minor phases including anatase TiO<sub>2</sub> (ICDD card 01-075-2547), rutile TiO<sub>2</sub> (ICDD card 01-079-6029), Ti<sub>2</sub>O<sub>3</sub> (ICDD card 01-074-0324), and Ti<sub>3</sub>O<sub>5</sub> (ICDD card 01-083-7068) (Figure 1c). For the sample treated with Sr(NO<sub>3</sub>)<sub>2</sub>, the presence of orthorhombic SrCO<sub>3</sub> (ICDD card 01-078-4340) was additionally observed at 180°C, and crystallinity noticeably increased with temperature (Figure 1d). The appearance of titanium oxide phases was attributed to the oxidation of

TiC during the hydrothermal treatment, while the presence of SrCO<sub>3</sub> resulted from the reaction between Sr<sup>2+</sup> and CO<sub>2</sub> in the reaction solution [35]. Furthermore, compared to HT180, SrHT180 exhibited significantly higher and sharper Ti<sub>2</sub>O<sub>3</sub> and Ti<sub>3</sub>O<sub>5</sub> peaks with a decrease in TiC peak intensity, suggesting an accelerating oxidation of TiC under the presence of Sr(NO<sub>3</sub>)<sub>2</sub>. At 200°C (SrHT200), phase composition remained the same (Figure 1e). Interestingly, at 225°C, rutile TiO<sub>2</sub>, Ti<sub>2</sub>O<sub>3</sub>, and Ti<sub>3</sub>O<sub>5</sub> disappeared, while TiC became more prominent (Figure 1f). This phenomenon could be attributed to the instability of those intermediate compounds under the hydrothermal conditions at or above 225°C, leading to the production of TiC through a carbothermal reduction pathway: TiO<sub>2</sub> → Ti<sub>3</sub>O<sub>5</sub> → Ti<sub>2</sub>O<sub>3</sub> → Ti(C<sub>x</sub>O<sub>y</sub>) → TiC [36]. Upon further increasing the temperature to 250°C (Figure 1g), the intensity of SrCO<sub>3</sub> and anatase TiO<sub>2</sub> peaks increased due to crystal growth, while the intensity of TiC decreased due to its increased oxidation rate. In addition, the crystalline sizes were estimated using the Scherrer equation and are presented in Table 2. It was observed that the crystallite size increased with the reaction temperature. Therefore, the synthesis temperature played a significant role on the phase composition and crystallite size of the nanocomposites.

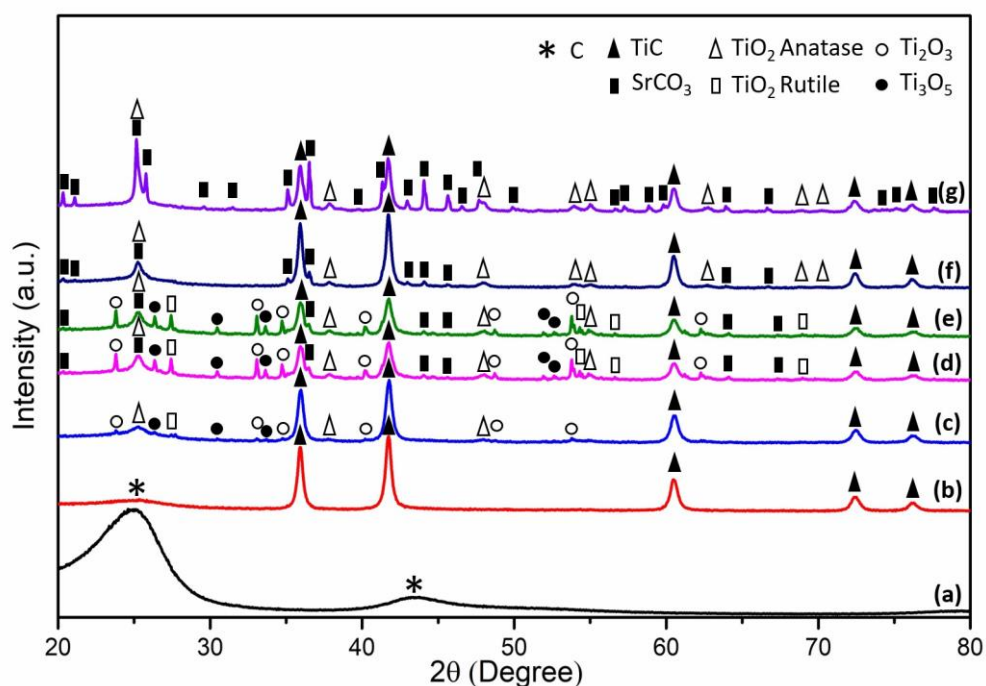


**Figure 1.** XRD results of (a) as-received CBs, (b) TCBs, (c) HT180, (d) SrHT180, (e) SrHT200, (f) SrHT225, and (g) SrHT250.

### 3.1.3 Structural study of core-shell composite particles

Figure 2 shows FE-SEM images of the as-received CBs, as-synthesized TCBs, HT180, SrHT180, SrHT200, SrHT225, and SrHT250. Before MSS, as-received CBs exhibit a spherical shape with an approximate diameter of 400 nm and smooth surfaces (Figure 2a). After molten salt synthesis, (TCBs) (Figure 2b) remained spherical shapes, and sizes of 400 nm, while their surfaces became rough due to the formation of dense TiC nanocrystals (shell) coating on carbon surfaces (core). This observation suggests the formation of core-shell structure after molten salt synthesis process. After hydrothermal processing at temperatures ranging from 180 to 250°C (Figure 2c-g), shapes and sizes of the materials remain unaltered, indicating that variation in hydrothermal temperature has no effect on shapes and sizes of the CBs. However, surface features, crystallite size and roughness were observed to be modified depending on hydrothermal temperature. As shown in Table 2, crystallite size of the coating components: TiC, TiO<sub>2</sub>, and SrCO<sub>3</sub> appeared to be increased with temperature. Not only that but also coating of CBs with TiC significantly increased the surface roughness from 8 nm (the uncoated CBs) to 17 nm (the TCBs). After oxidation, a notable increase in roughness was observed with temperature from 23 nm (the SrHT180) to 43 nm (the SrHT250). The observations indicated the influence of temperature on both crystallite size and roughness of the products. Furthermore, formation of nanosized holes was noticed on the hydrothermal product particles since the temperature was 180°C. This revealed clearly the fresh C (core) underneath the crystalline coating (shell) as indicated by arrows in (Figure 2d). The core was attributed to only unreacted C, while the shell was composed of TiC along with its oxidation products and SrCO<sub>3</sub>.

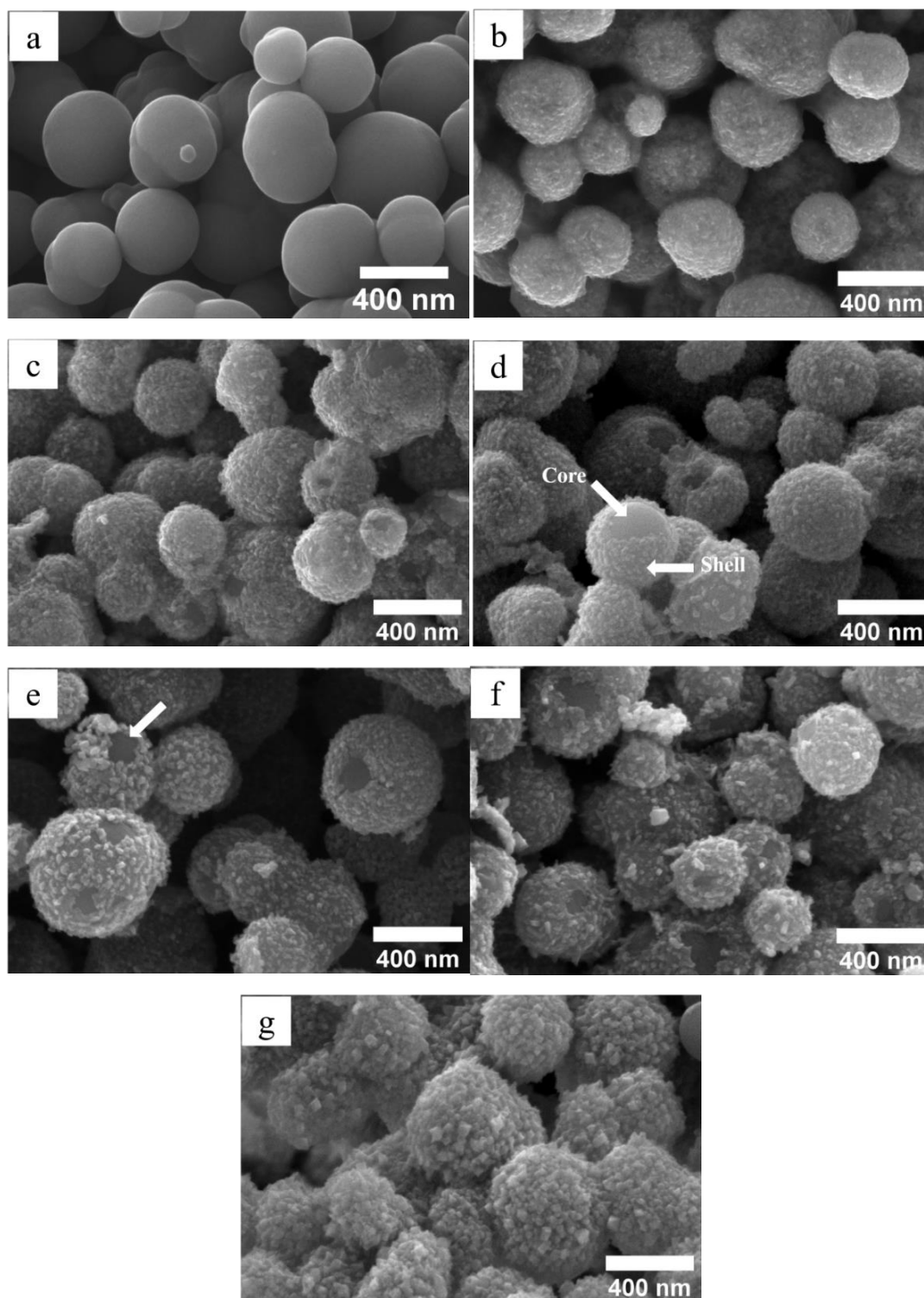


**Figure 2.** FE-SEM images of (a) as-received CBs, (b) TCBs, (c) HT180, (d) SrHT180, (e) SrHT200, (f) SrHT225, and (g) SrHT250.

**Table 2** Phase composition, crystallite size, and surface roughness of the samples.

Samples	Crystallite size (nm)			Surface roughness (nm)
	TiC	TiO <sub>2</sub> Anatase	SrCO <sub>3</sub>	
CBs	-	-	-	8
TCBs	39.54	-	-	17
HT180	19.35	28.38	-	21
SrHT180	27.48	32.91	57.53	23
SrHT200	28.97	35.13	71.02	25
SrHT225	33.61	36.33	71.39	30
SrHT250	42.44	38.08	76.85	43

#### 3.1.4 Wettability measurement of the core-shell composite particles

The measurement of sample wettability was conducted using an OCA-15EC contact angle (CA) meter. The contact angle is a reliable parameter used to assess the hydrophobic or hydrophilic nature of a surface. Contact angle measurements were performed on the as-received CBs, TCBs, HT180, SrHT180, SrHT200, SrHT225, and SrHT250 samples (Figure 3). The CBs served as the control group. The contact angles for the CBs and TCBs were  $49.5 \pm 2.47^\circ$  and  $34.4 \pm 1.72^\circ$ , respectively, indicating an improved wettability of the CB particles when coated with TiC. After hydrothermal treatment, the wettability of the samples exhibited significant enhancements compared to the control. The degree of improvement increased with the rise in hydrothermal temperature. At 180°C (SrHT180), the contact angle value was  $33.8 \pm 1.69^\circ$ , while at 250°C (SrHT250), it reduced further to  $24.1 \pm 1.20^\circ$ . Moreover, even at the same reaction temperature, particles containing SrCO<sub>3</sub> (SrHT180) exhibited superior wettability compared to those without SrCO<sub>3</sub> (HT180). It was also suggested that the presence of anatase TiO<sub>2</sub> nanocrystals on the particle surfaces contributed to increased wettability, as reported by He et al. [37], who observed better surface wettability for anatase TiO<sub>2</sub> compared to the rutile phase. Therefore, the significant changes in contact angle values were attributed to factors such as crystallite size, surface roughness, and phase composition, which were influenced by the reaction temperature. It is important to note

that the wettability behavior of materials can be tailored by adjusting the reaction temperature, and such surface properties play a crucial role in cell adhesion.

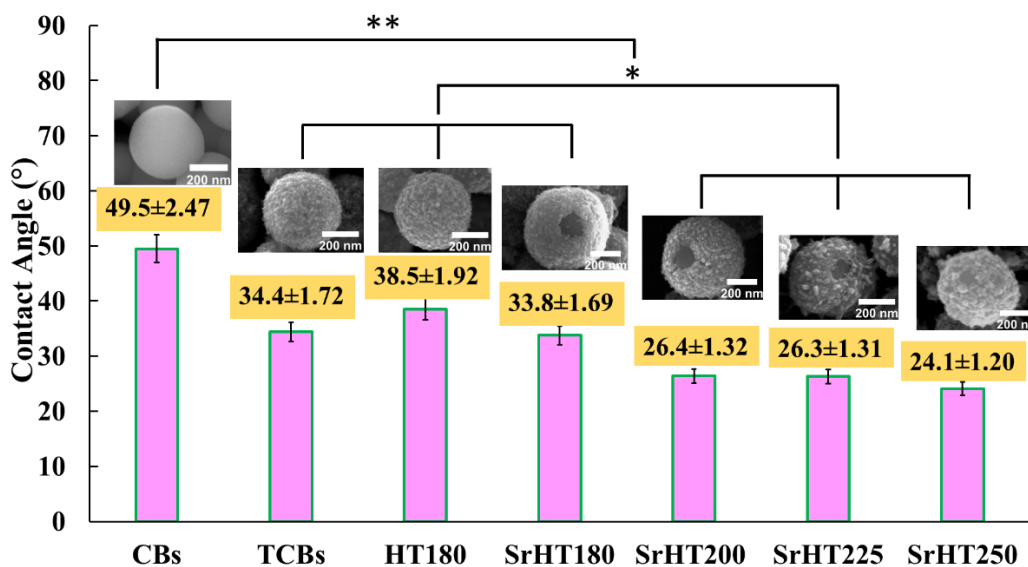


**Figure 3.** Contact angle measurements of bare CBs, TCBs, and hydrothermally treated samples at various temperatures. The insets FE-SEM images show the surface features of the samples.

### 3.2 Biological functions of core-shell composite particles

#### 3.2.1 Cell proliferation

To evaluate cell proliferation and biocompatibility, the PrestoBlue assay (PrestoBlue® Cell Viability Reagent, Invitrogen, USA) was employed on day 1, day 3, day 5, and day 7. Cell proliferation plays a crucial role in the biological aspect, influencing the promotion of osseointegration in bone implant materials [38]. To assess the bioactivity of the samples within each group, the PrestoBlue® reagent was utilized over a period of seven days, as depicted in Figure 4. On day 1, the SrHT250 group exhibited greater cell proliferation compared to the control, HT180, SrHT180, SrHT200, and SrHT225 groups. On day 3, the SrHT250 group displayed significantly higher cell proliferation than the other groups: the control, HT180, SrHT180, SrHT200, and SrHT225. On the fifth day, both the HT180 and SrHT180 groups demonstrated

similar results, which were significantly lower than those of the SrHT200, SrHT225, and SrHT250 groups. HT180 group exhibited less proliferation than the other groups, except for the control group on day 7. It is worth noting that cell proliferation substantially increased from the first to the seventh day within each group. Intriguingly, the SrHT250 group consistently exhibited the highest cell proliferation on all tested days, attributed to its elevated roughness, wettability, and high crystallinity of anatase TiO<sub>2</sub> and SrCO<sub>3</sub>. According to Wang et al. [39], anatase TiO<sub>2</sub> demonstrated superior cell behaviors such as adhesion, proliferation, and differentiation. Our findings support that the combined properties of TiC/TiO<sub>2</sub>/SrCO<sub>3</sub>-coated CB particles are essential for the enhancement in cell adhesion and proliferation.

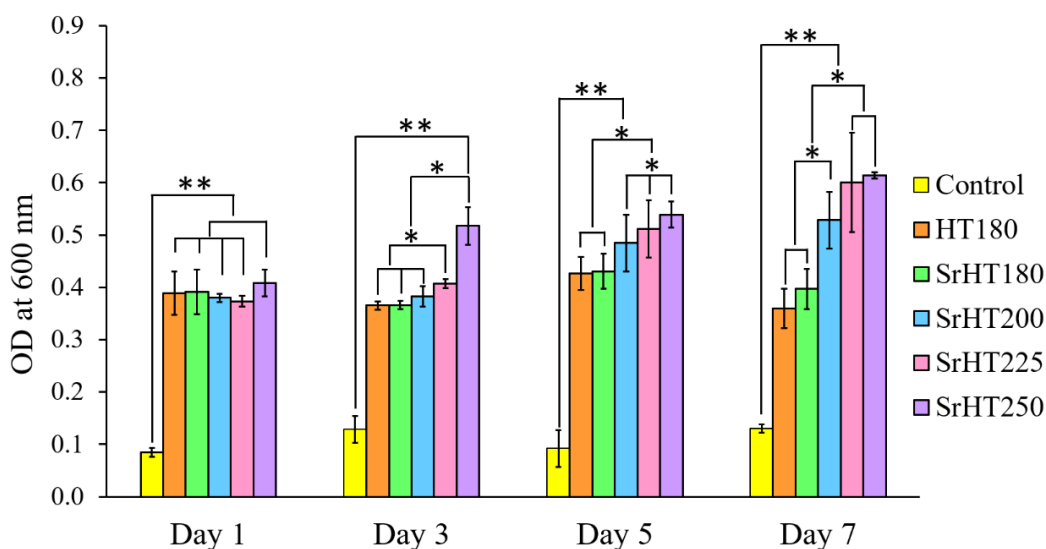


**Figure 4.** Cell proliferation of samples after measured with PrestoBlue<sup>®</sup> on day 1, 3, 5 and 7.

### 3.2.2 Cell viability

To determine viable cell numbers in the cell culture experiment, cell viability and migration were observed on the samples using FDA staining under a fluorescence microscope. Figure 5 illustrates the increase in osteoblast cells over time. It is evident that both on day 1 and day 5, the control and HT180 samples exhibited less cell adhesion compared to the Sr-groups, highlighting the role of SrCO<sub>3</sub> in enhancing cell adhesion and viability. Notably, the SrHT225 and SrHT250 samples demonstrated high

cell anchorage on both days. These results indicate that the nanocomposite particles possess a favorable surface for cell adhesion and viability. This finding aligns with a previous study [40] which reported that SrCO<sub>3</sub> promoted viable cell numbers and significant cell attachment, demonstrating its cytocompatibility and ability to improve bone tissue formation. In our research, it is suggested that factors such as phase composition, nanotopography, and wettability contribute to the enhanced cell adhesion and viability of the SrHT225 and SrHT250 nanocomposites. TiC, as suggested by Lopreiato et al. [41], can promote cell maturation and adhesion. Moreover, anatase TiO<sub>2</sub> has been recognized as a suitable material for bone cell adhesion due to its ability to absorb more hydroxyl groups on surfaces, which is favorable for bone tissue formation [42]. Our findings indicate that the SrHT225 and SrHT250 samples exhibited higher hydrophilic surfaces compared to the other groups (Figure 3), and a highly wettable surface was conducive to increased cell attachment. Additionally, Chen et al. [43] reported that the nanotopography of particles influences cell adhesion, with higher roughness and larger crystal size promoting cell adhesion and spreading. This correlation is consistent with the nanotopography presented in this study, where roughness and crystal size increased with temperature, resulting in enhanced osteoblast cell adhesion on the as-prepared core-shell particles, particularly in the case of SrHT225 and SrHT250 samples.

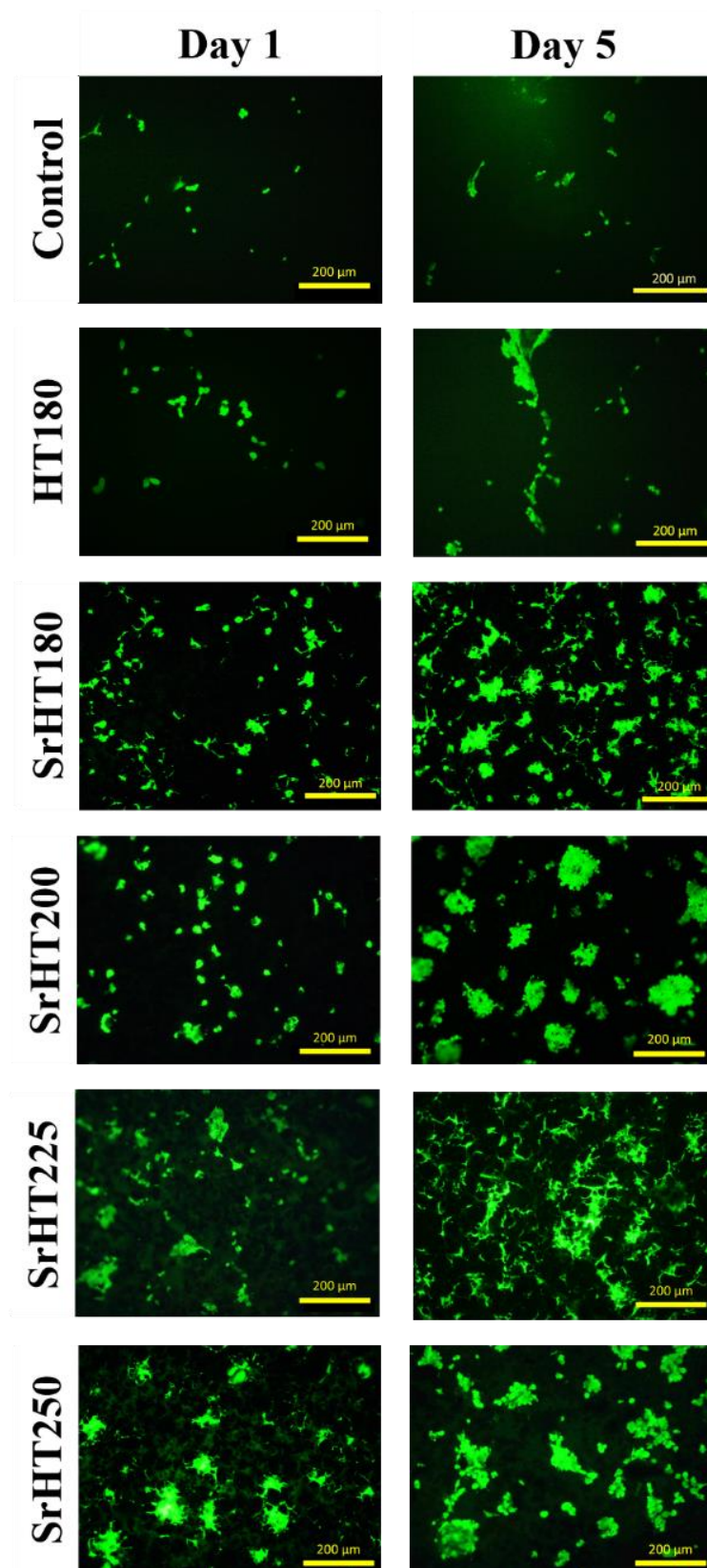


**Figure 5.** Cell viability on the samples after day 1 and 5.

### 3.2.3 Calcium deposition

To measure calcium deposition, cell-lysis solutions were employed in accordance with the manufacturer's guidelines (Calcium Colorimetric Assay Kit, MAK022, Sigma-Aldrich, USA). The measurement of calcium deposition on the samples was performed on day 7, day 14, and day 21, as indicated in Figure 6 by measuring the optical density (OD) at 575 nm. On day 7, the SrHT200 group exhibited higher calcium deposition compared to the other groups. On day 14, the calcium deposition of the SrHT200 group remained higher than the other groups, except for the SrHT250 group. On day 21, the SrHT250 group demonstrated the highest calcium deposition among all groups. Notably, there was a significant increase in calcium deposition over time for the Sr-containing groups, particularly in the case of SrHT250. These results highlight the crucial role of TiC/TiO<sub>2</sub>/SrCO<sub>3</sub>-coated carbon black particles in promoting calcium deposition. Previous research has reported that Sr-modified bioactive ceramic nanoparticles facilitate calcium deposition, mineralization, and bone differentiation [44]. The presence of SrCO<sub>3</sub> nanoparticles notably enhances cell adhesion, proliferation, growth rate, alkaline phosphatase (ALP) activity, and calcium deposition in osteoblast cells.

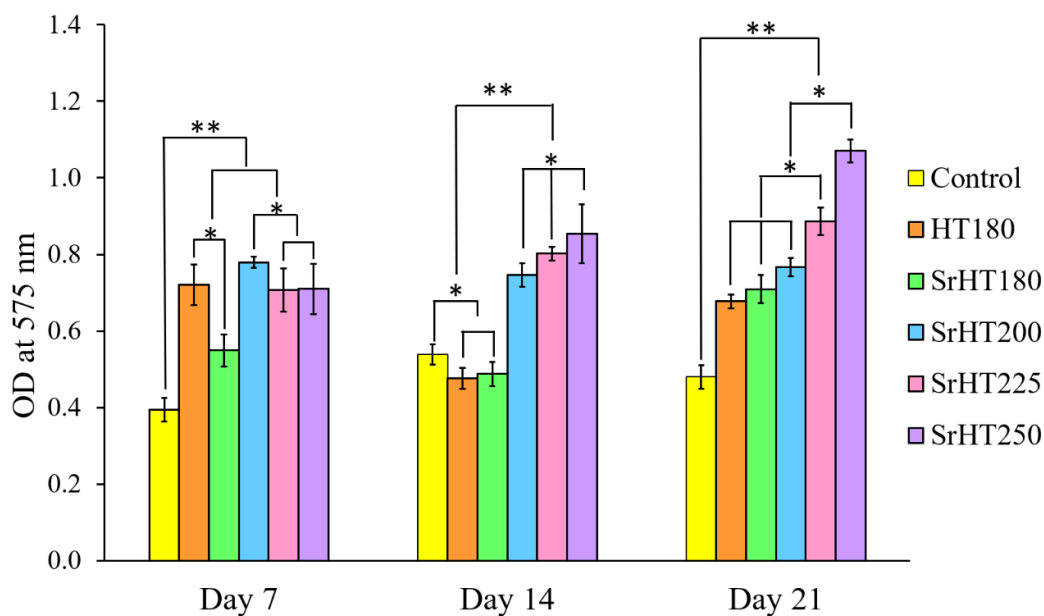


**Figure 6.** Calcium deposition of samples on day 7, 14 and 21.

Furthermore, the hydrophilicity and nanotopography of the nanocomposite particles have been identified as critical properties that enhance their bioactive functions, as supported by previous findings [45],[46]. Ceramic particles serve as templates for calcium attachment secreted by osteoblast cells during bone tissue formation, while hydrophilic particles with rough surfaces act as preferential substrates for calcium deposition. In our study, the results demonstrate that the nanocomposite particles, particularly the SrHT250 group, which exhibit high hydrophilicity and favorable nanotopography, exhibit greater calcium deposition compared to particles with lower hydrophilicity and roughness.

### 3.3 Core-shell porous mixed oxide phases with TiC coating on CBs

The study on this topic, including the experimental details and the discussion of the significant results, is presented in the form of an academic article that has been published in *Journal Materials Research*, Volume 38, Pages. 3504-3518 as attached in Appendix B. The important results are phase composition, morphology, wettability measurement, and biological functions of the core-shell porous particles as follows.

#### 3.3.1 Preparation of core-shell porous mixed oxide phases with TiC coating on CBs

TiC-coated carbon black particles were prepared via molten salt synthesis according to the above section and our previous procedure [47]. Titanium powders were mixed with CBs at a molar ratio of 1:8. The resulting mixture was then combined with KCl using an agate mortar. The mixture was transferred to an alumina crucible and covered with a lid. Subsequently, it was placed inside an alumina tube furnace and subjected to a firing process at 900°C for 4 h. The procedure was carried out in an atmosphere protected by argon gas, with both heating and cooling rates set at 3°C/min. After the furnace cooled down, the solidified mass was thoroughly rinsed with distilled water to eliminate any residual salt. The sample was dried in an oven overnight. The obtained samples were designated as TCBs. To obtain porous structure of mixed oxide phased with TiC on CBs, TCBs were made calcination for 20 min at 100, 150, 200, and 250°C. The obtained samples were labelled as shown in Table 3.

**Table 3** Sample ID and fabricating conditions.

Samples	Details
CBs	As-received carbon black particles
TCBs	TiC-coated carbon black particles via molten salt synthesis at 900°C for 4 h
TCBs100	Calcination at 100°C
TCBs150	Calcination at 150°C
TCBs200	Calcination at 200°C
TCBs250	Calcination at 250°C
Control	Agarose hydrogel solution without particles

### 3.3.2 Phase composition and crystallinity of core-shell porous particles

Figure 7 illustrates XRD pattern of the CBs and TCBs synthesized using MSS at 900°C for 4 h, with a Ti:CBs ratio of 1:8. The XRD pattern of these samples was compared with those obtained after calcination at temperatures of 100, 150, 200, and 250°C for 20 min. The XRD pattern in Figure 7a reveals the presence of a single phase, denoted as the C phase, at  $2\theta$  values of 25.18° and 43.5°. These peaks correspond to the amorphous nature of the initial CB particles (ICDD card 00-041-1487). Figure 7b, the diffraction peaks observed at  $2\theta$  values of 35.9°, 41.9°, 60.5°, 72.4°, and 76.1° correspond to the (111), (200), (220), (311), and (222) reflections of TiC, respectively. These peaks indicate the presence of TiC in the sample. Additionally, a broad peak associated with carbon is observed at  $2\theta = 25.18^\circ$ , indicating the amorphous nature of the carbon black used. No residual titanium or intermediate phases were detected, suggesting complete reaction of TiC via MSS. Figure 7c shows the XRD pattern after calcination at 100°C (TCBs100), where a small additional peak corresponding to rutile TiO<sub>2</sub> is observed at  $2\theta = 27.4^\circ$  (110), along with the TiC and C peaks. As the temperature is increased to 150-200°C (TCBs150, TCBs200), two more oxide phases, Ti<sub>2</sub>O<sub>3</sub> and Ti<sub>3</sub>O<sub>5</sub>, are observed alongside TiC, C, and rutile (Figure 7d, 7e). The appearance of titanium oxide phases indicates the oxidation of TiC during thermal treatment in the presence of air. Furthermore, at 250°C (TCBs250), the intensity of the TiC peaks decreases noticeably, while the intensity of the oxide peaks increases due to

the accelerated oxidation rate at this temperature (Figure 7f). Additionally, the samples subjected to higher temperatures exhibit increased crystallinity compared to the lower temperature samples. The determination of the crystalline size of the samples was examined using the Scherrer equation [48]. The crystallinities of samples were increased with an increase in calcination (Table 4). Clearly, calcination affected the crystalline size and the formation of the mixed-phases particles.

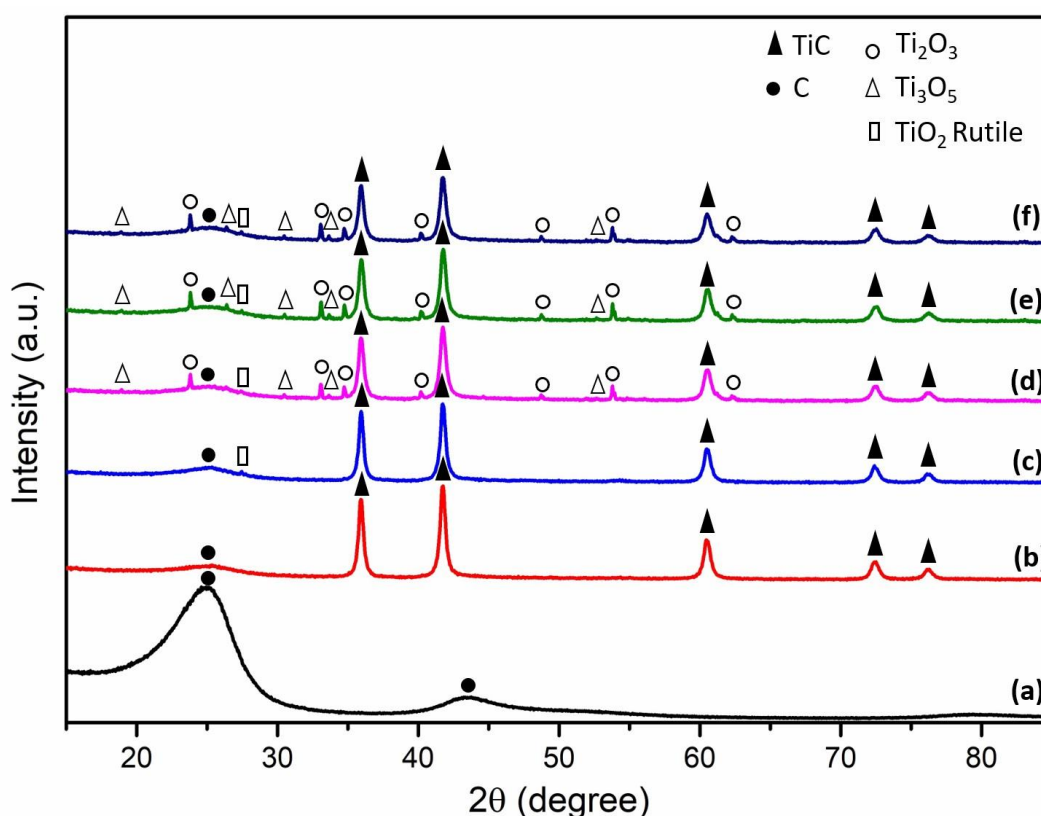
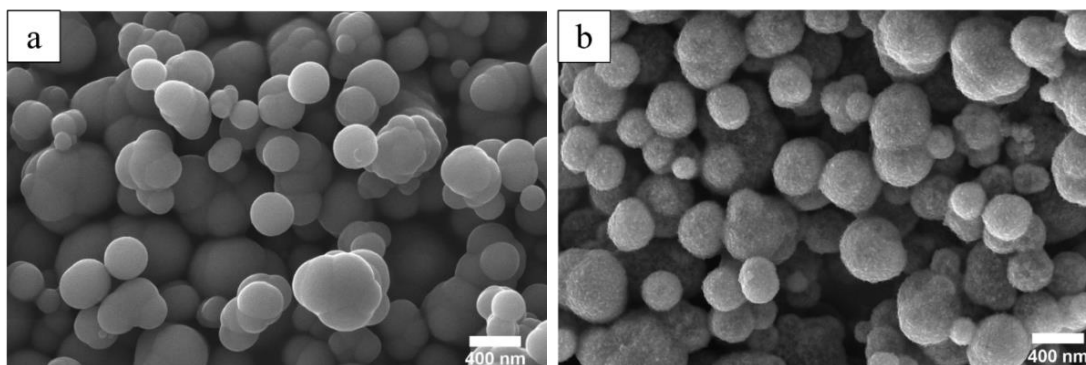


**Figure 7.** XRD results of the samples; (a) CBs, (b) TCBs, (c) TCBs100, (d) TCBs150, (e) TCBs200, and (f) TCBs250.

### 3.3.3 Structural study of core-shell porous particles

Figure 8 presents FE-SEM images of CBs and the samples prepared under different conditions. The FE-SEM images provide the morphologies and surface characteristics of the CBs (Figure 8a), TCBs prior to oxidation (Figure 8b), and compare them with the calcination samples (Figure 8c-f). The CBs exhibit spherical

shapes with smooth surfaces. The TCBs display spherical structures with an average particle size of 400 nm and rough surfaces, attributed to the presence of TiC nanocrystals on their surfaces. Calcination at temperatures ranging from 100°C to 250°C, all the particle samples retain their spherical shapes and 400 nm size, but their surface features were modified. The observation of porosity, indicated by circles and arrows, becomes evident starting from calcination temperature of 150°C (TCBs150) and becomes more pronounced at 200°C and 250°C for TCBs200 and TCBs250, respectively. Notably, TCBs250 exhibits more voids with diameters of approximately 80-130 nm, and some broken coatings are observed, as indicated by the arrows. These observations are likely a result of crystal growth and an increased oxidation rate of TiC at 250°C. The formation of such porous structures reveals the underlying carbon (C) core and confirms the core-shell structure of the particles. This phenomenon can be attributed to the diffusion rates of materials in the core (C) and shell (TiC) at the calcination temperature. The roughness of the samples is evaluated using the arithmetic average roughness (Ra) equation [49]. The findings revealed a noticeable increase in surface roughness values as the calcination temperatures were raised. The surface roughness of the particles was estimated and reported in Table 4. Core-shell structure of the TCBs250 was further confirmed by TEM (Figure 9). The shell thickness was around 15 nm. The SAED pattern revealed the diffraction rings of the (111), (200), (220), and (311) planes of the cubic TiC and the (002) plane of C.



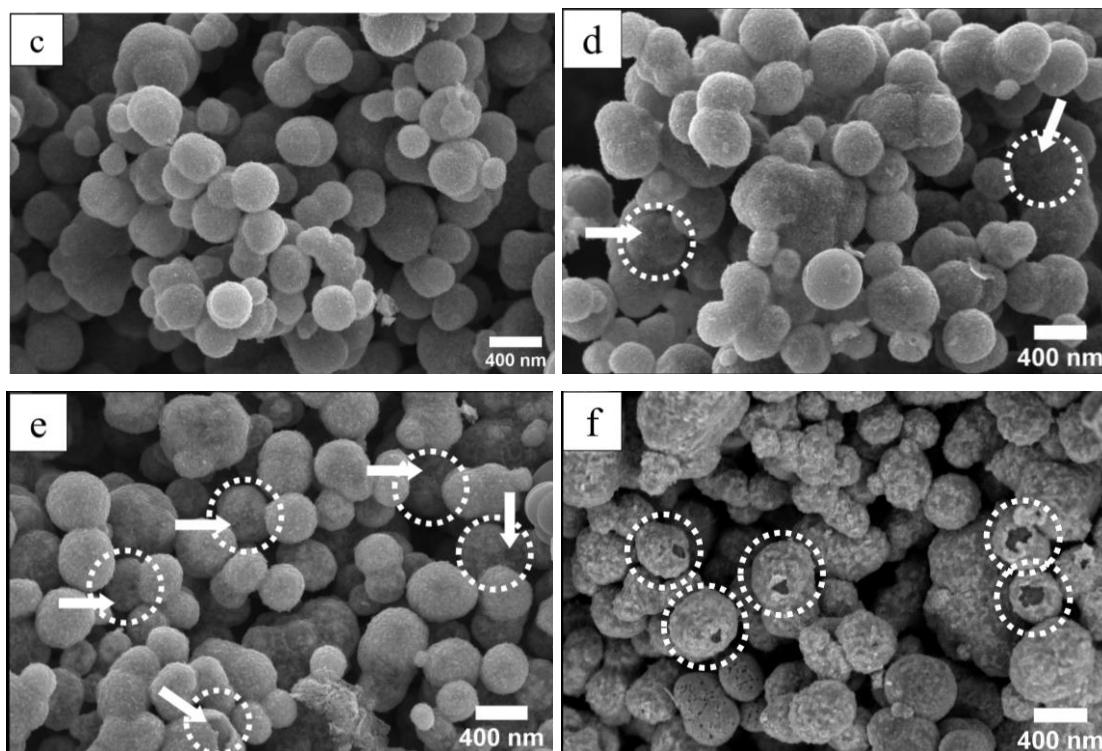


**Figure 8.** FE-SEM images of the samples; (a) CBs, (b) TCBs, (c) TCBS100, (d) TCBS150, (e) TCBS200, and (f) TCBS250.

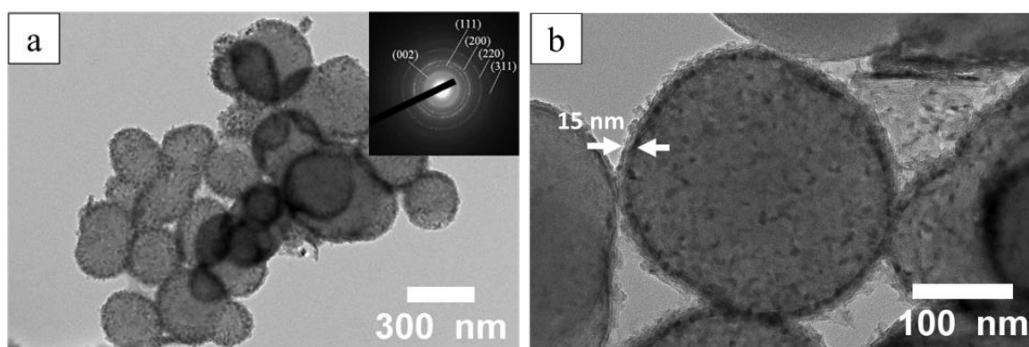


**Figure 9.** TEM images of TCBS250: at magnification of (a) 25 000x and (b) 100 000x. The insert in (a) is SAED pattern of particles.

### 3.3.4 Wettability measurement of core-shell porous particles

Surface wettability plays a significant role in the evaluation of the biological response of biomaterials and greatly influences cell behavior during the bone formation process. Contact angle measurements were performed to assess the wettability of the

uncoated CBs, TCBs, TCBs100, TCBs150, TCBs200, and TCBs250. The control group consisted of uncoated CBs, which exhibited a contact angle value of  $49.5\pm 0.45^\circ$ . A significant decrease in the contact angle was observed in TCBs  $35.8\pm 0.18^\circ$  compared to the uncoated particles. Subsequently, when the TCBs were thermally treated in air at temperatures ranging from  $100^\circ\text{C}$  to  $250^\circ\text{C}$ , their contact angles values further decreased. The contact angle values for TCBs100, TCBs150, TCBs200, and TCBs250 were measured as  $33.9\pm 0.15^\circ$ ,  $23.9\pm 0.12^\circ$ ,  $20.8\pm 0.12^\circ$ , and  $19.1\pm 0.10^\circ$ , respectively. It is worth noting that all the TCBs groups displayed a considerable reduction in contact angle value, from  $49.5\pm 0.45^\circ$  for CBs to  $19.1\pm 0.10^\circ$  for TCBs250. Moreover, the estimated surface roughness values of the CBs, TCBs, TCBs100, TCBs150, TCBs200, and TCBs250 were determined as  $7.03\pm 0.05$ ,  $15.07\pm 0.02$ ,  $15.09\pm 0.03$ ,  $15.42\pm 0.12$ ,  $16.78\pm 0.26$ , and  $19.60\pm 0.42$ , respectively. It is noteworthy that all TCBs groups exhibited higher surface roughness values compared to the CBs. This phenomenon can be attributed to the enhanced porosity observed in the particles, which is in accordance with the observation from FE-SEM image (Figure 8). Remarkably, TCBs250 exhibited a lower contact angle compared to the other samples, which can be ascribed to its increased porosity and surface roughness. These factors contribute to enhanced hydrophilicity.

**Table 4** The crystalline size, surface roughness and contact angle measurement of the samples.

Samples	Crystalline size (nm)	Surface roughness (nm)	Contact angle ( $^\circ$ )
CBs	-	$7.03\pm 0.05$	$49.5\pm 0.45$
TCBs	19.31	$15.07\pm 0.02$	$35.8\pm 0.18$
TCBs100	20.36	$15.09\pm 0.03$	$33.9\pm 0.15$
TCBs150	25.42	$15.42\pm 0.12$	$23.9\pm 0.12$
TCBs200	32.96	$16.78\pm 0.26$	$20.8\pm 0.12$
TCBs250	35.21	$19.60\pm 0.42$	$19.1\pm 0.10$

### 3.4 Biological functions of core-shell porous particles

#### 3.4.1 Cell proliferation

Cell proliferation was assessed at different time points (day 1, 3, 5, and 7) using PrestoBlue assay. Figure 10 illustrates the results, demonstrating that the control group, TCBs, TCBs100, and TCBs150 exhibited lower levels of cell proliferation compared to the other two samples. Specifically, TCBs200 displayed lower cell proliferation than the other groups on day 1 but demonstrated an increase in cell proliferation from day 3 to day 5, with further growth observed up to day 7. Overall, cell proliferation increased progressively from day 1 to day 7, and the TCBs250 group exhibited significantly higher proliferation compared to the other groups, except for TCBs200 on day 5 and 7. Notably, the cell proliferation results were comparable for TCBs200 and TCBs250 on days 5 and 7. A high cell proliferation rate indicates a high level of tissue formation, which is in good agreement with previous research [50]. Furthermore, cell proliferation plays an important role in biological processes that contribute to the improvement of the bioperformance of particulate biomaterials for bone tissue applications [51].

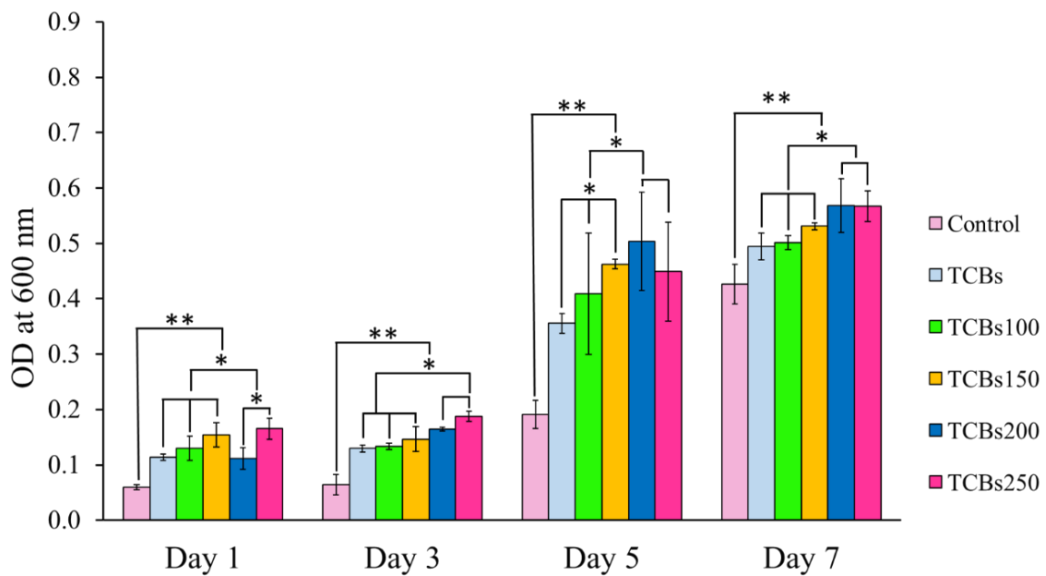


**Figure 10.** Cell proliferation of the samples measured with PrestoBlue<sup>®</sup> on day 1, 3, 5 and 7.

### 3.4.2 Protein synthesis

The protein synthesis of the samples was evaluated using the BCA kit, and the measurements were taken at OD 595 nm on day 7, 14, and 21, as depicted in Figure 11. The results indicate that the protein synthesis values for all groups did not exhibit significant differences from day 7 to day 21, except for the TCBs250 group. On day 7, both the control and TCBs demonstrated lower protein synthesis values compared to the other groups. Conversely, the TCBs250 group exhibited significantly higher protein synthesis values on day 14. Furthermore, the protein synthesis values of TCBs100, TCBs150, and TCBs200 were higher than those of the control and TCBs groups on day 14 and 21. Especially, the TCBs250 group displayed the highest protein synthesis levels on both days 14 and 21. Enhanced protein adhesion is related to the improved wettability of the sample and points out the importance of hydrophilicity in promoting bone formation. Wettability plays a vital role in cell adhesion, proliferation, and protein adsorption. Furthermore, Elisa et al. [52] highlighted that protein adhesion on the surface of bioactive materials is influenced by the surface properties.

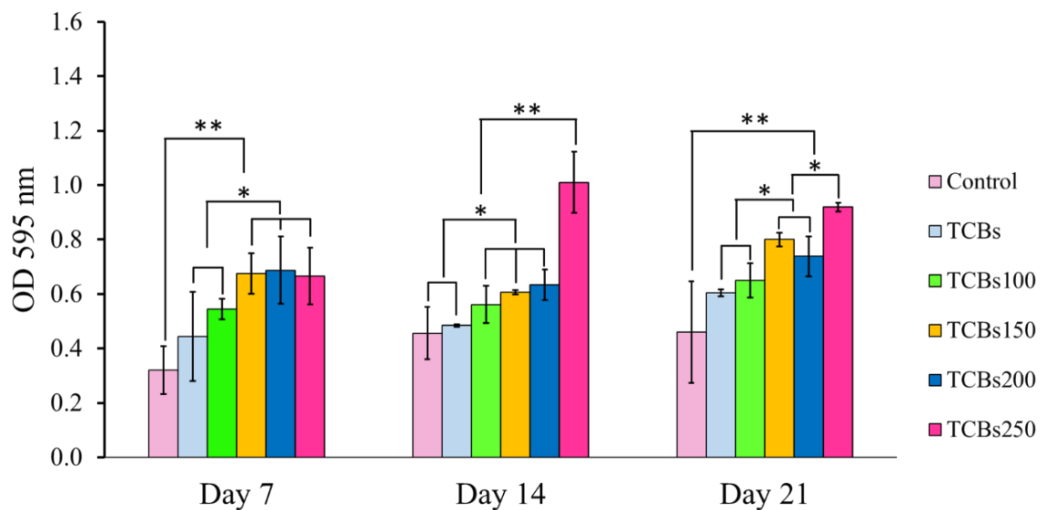


**Figure 11.** Protein synthesis of the samples on day 7, 14 and 21.

### 3.4.3 ALP activity

ALP activity of the samples was examined, and the results are displayed in Figure 12. On day 7, the ALP activity of TCBS100 was comparable to that of TCBS150, and both exhibited higher values compared to the control and TCBS groups. On day 14, the control group displayed lower ALP activity than the other groups. TCBS200 demonstrated similar ALP activity to the control on day 7 but exhibited significantly higher activity than the control on day 21. The modified samples exhibited enhanced ALP activity in comparison to the control group, which can be attributed to the increased proliferation of MG-63 cells on TCBS200. The highest ALP values were observed in TCBS250 on both day 7 and 21. The findings suggest that ALP activity increases over time. The bioactive surface area of oxide particles, particularly  $Ti_2O_3$ , plays a crucial role in influencing ALP activity induction. A higher surface area of  $Ti_2O_3$  particles has been found to promote greater ALP activity compared to particles with a lower surface area. Some studies have reported the bioactivity of titanium oxide surfaces in stimulating ALP activity [53],[54].

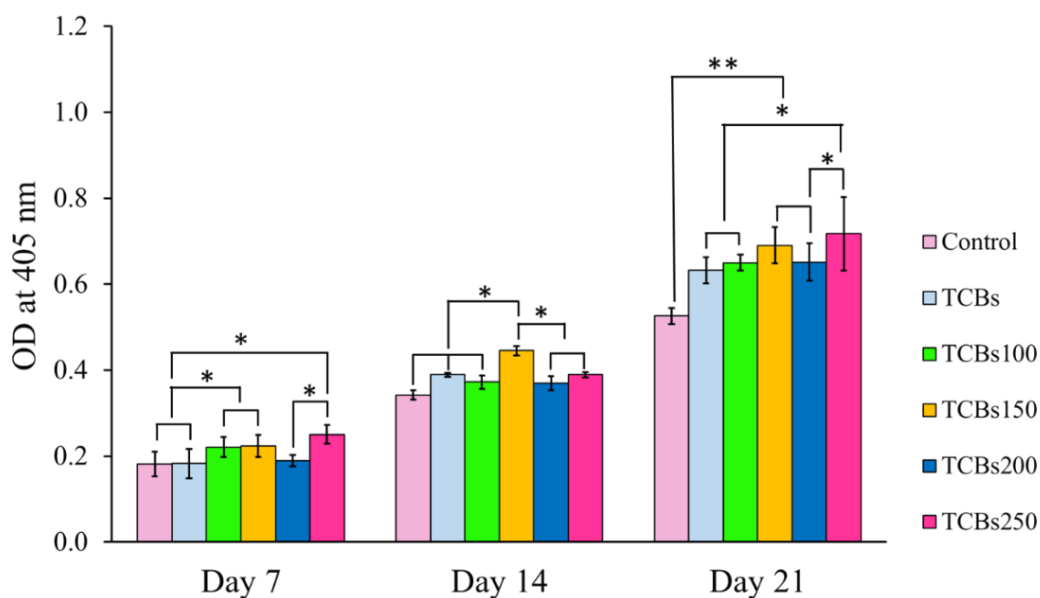


**Figure 12.** ALP activity of the samples on day 7, 14, and 21.

### 3.4.4 Calcium deposition

Calcium deposition on the samples was evaluated by measuring the optical density (OD) at 575 nm on days 7, 14, and 21, as shown in Figure 13. On day 7, the TCBs200 and TCBs250 samples exhibited higher calcium deposition compared to the other groups. Similar levels of calcium deposition were observed in the control, TCBs, and TCBs100 groups on day 14. Furthermore, the TCBs150, TCBs200, and TCBs250 samples demonstrated higher calcium deposition compared to the control, TCBs, and TCBs100 groups. On day 21, the control group displayed significantly lower calcium deposition compared to the other groups. The increased calcium deposition observed in the modified samples can be attributed to the presence of Ti-based bioactive compounds, including TiC, TiO<sub>2</sub>, Ti<sub>2</sub>O<sub>3</sub>, and Ti<sub>3</sub>O<sub>5</sub>, on the surface of the particles. In the present study, a notable increase in calcium deposition was observed on TCBs250, which is in good agreement with previous studies [55-57] that can be attributed to the presence of mixed phases on the surface of the particles.

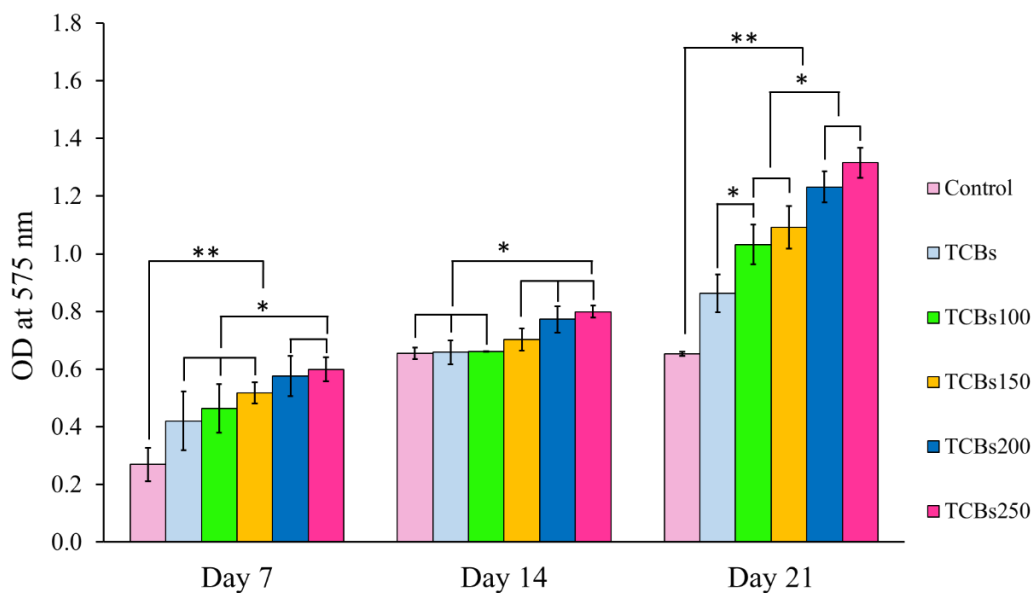


**Figure 13.** Calcium deposition of samples on day 7, 14 and 21.

## 4. CONCLUSIONS

### 4.1 Core-shell structure of TiC/TiO<sub>2</sub>/SrCO<sub>3</sub> coating on carbon black particles

The surface modification of carbon black particles was accomplished by coating of TiC/TiO<sub>2</sub>/SrCO<sub>3</sub> nanocrystals using molten salt synthesis and hydrothermal treatment to enhance wettability and bioactivity of the particles. Molten salt synthesis offered core-shell structure of TiC-coated carbon black particles leading to a significant improvement in particle wettability. Hydrothermal synthesis conducted at different temperatures facilitated the development of multi-oxide phases on the shell layers, thereby enhancing the bioactivity of the particles. It was found that the reaction temperature played a crucial role in influencing the microstructure, crystallite size, surface roughness, and biological functionalities of the particles. Crystallite size, surface roughness, and wettability of the coated particles increased with temperature giving rise to a favored-nanotopography for cell activities of the particles heated at 250°C. Such a unique core-shell structure with a well-reserved nanotopography and the synergistic effects facilitated by the multi-phase TiC/TiO<sub>2</sub>/SrCO<sub>3</sub> of the particles treated at 250°C led to an enhancement in various bioactivities such as cell adhesion, proliferation, osteogenic differentiation, and calcium deposition of osteoblast cells. These results illuminate the potential for the development of bioactive particles suitable for use as filling materials in films and/or scaffolds for guided bone regeneration (GBR).

(This work has been published in Journal of American Ceramic Society; Vol. 106, pp. 2689-2701, 2023)

#### 4.2 Core-shell porous bioactive compound of mixed oxide phases with TiC on carbon black particles

In this study, we successfully fabricated core-shell bioactive compounds comprising mixed oxide phases with TiC on CBs for bone augmentation in oral and maxillofacial surgery. These particles were synthesized using molten salt synthesis and calcination at various temperatures. The resulting particles exhibited a core-shell structure with a porous structure. This unique structure contributed to enhanced hydrophilicity, increased surface roughness, and improved bioactivity of the particles. Interestingly, as temperature increased during calcination, the samples exhibited greater surface roughness, porosity, and crystallite size compared to the other samples. These characteristics are known to influence the biological response and bioactivity of biomaterials, promoting favorable outcomes in bone tissue regeneration. Moreover, the porous structure of the particles facilitated the attachment of biological molecules, serving as signaling cues to promote the formation of new bone tissue. Notably, TCBs250 demonstrated superior biological performance compared to the other samples, exhibiting the highest cell response and bioactivity. In conclusion, TCBs250 emerged as a promising material for bone formation in oral and maxillofacial surgery. The core-shell structure, coupled with its enhanced bioactivity and favorable cellular response, TCBs250 is a potential candidate for application in bone tissue engineering and regenerative medicine in the field of oral and maxillofacial surgery. This research reveals valuable insights into the advancement of bioactive particles as a filling material within films and/or scaffolds, serving the purpose of guided bone regeneration (GBR). These findings contribute significantly to the ongoing development of biomaterials for enhanced bone regeneration, offering promising prospects for future clinical applications.

(This work has been published in *Journal of Materials Research*, Vol. 38, pp. 3504-3518, 2023)

### 4.3 Conclusion remarks

In conclusion, our research has culminated in the enhancement of wettability and bioactivity of submicron-sized carbon black particles via meticulous surface modification processes: molten salt synthesis through the hydrothermal method and calcination. Molten salt synthesis yielded a core-shell structure with TiC coating on CBs. Furthermore, subsequent hydrothermal and calcination at different temperatures led to the development of multi-phased structures in the shell layers. These structural enhancements significantly improved particle wettability, paving the way for a fundamental improvement in their bioactivity. Moreover, the reaction temperature during the synthesis processes was revealed to be a pivotal factor influencing several parameters. As the temperature increased, the crystalline size, surface roughness, wettability, and biological functionality of the particles were affected. Our findings contribute significantly to the ongoing evolution of biomaterials designed to enhance bone regeneration and serve as promising materials in films or scaffolds, particularly for guided bone regeneration applications.

## 5. BIBLIOGRAPHY AND REFERENCES

- [1] S. Petti, U. Glendor, and L. Andersson, “World traumatic dental injury prevalence and incidence, a meta-analysis-One billion living people have had traumatic dental injuries,” *Dent. Traumatol.*, vol. 34, no. 2, pp. 71–86, Apr. 2018, doi: 10.1111/edt.12389.
- [2] Z. Sheikh, C. Sima, and M. Glogauer, “Bone Replacement Materials and Techniques Used for Achieving Vertical Alveolar Bone Augmentation,” *Materials (Basel)*., vol. 8, no. 6, pp. 2953–2993, May 2015, doi: 10.3390/ma8062953.
- [3] M. Esposito, M. G. Grusovin, S. Kwan, H. V. Worthington, and P. Coulthard, “Interventions for replacing missing teeth: Bone augmentation techniques for dental implant treatment,” *Cochrane Database Syst. Rev.*, no. 3, pp. 70–71, 2008, doi: 10.1002/14651858.CD003607.pub3.
- [4] T. P. Chaturvedi, “Allergy related to dental implant and its clinical significance,” *Clin. Cosmet. Investig. Dent.*, vol. 5, pp. 57–61, 2013, doi: 10.2147/CCIDE.S35170.
- [5] A. R. Amini, J. S. Wallace, and S. P. Nukavarapu, “Short-term and long-term effects of orthopedic biodegradable implants,” *J. Long. Term. Eff. Med. Implants*, vol. 21, no. 2, pp. 93–122, 2011, doi: 10.1615.
- [6] J. Girón *et al.*, “Biomaterials for bone regeneration: an orthopedic and dentistry overview,” *Brazilian J. Med. Biol. Res.*, vol. 54, no. 9, pp. 1–15, 2021, doi: 10.1590/1414-431x2021e11055.
- [7] H. Siddiqui, K. Pickering, and M. Mucalo, “A Review on the Use of Hydroxyapatite-Carbonaceous Structure Composites in Bone Replacement Materials for Strengthening Purposes,” *Materials (Basel)*., vol. 11, no. 10, p. 1813, Sep. 2018, doi: 10.3390/ma11101813.
- [8] R. A. Horowitz, Z. I. V Mazor, C. Foitzik, H. Prasad, M. Rohrer, and A. D. Y. Palti, “ $\beta$  -Tricalcium phosphate as bone substitute material: Properties and clinical applications,” *J. Osseointegration*, vol. 1, no. 1, pp. 60–68, 2010.
- [9] R. AL Jasser and S. Andreana, “An overview of bone augmentation

- techniques,” *Clin. Case Reports Rev.*, vol. 2, no. 4, 2016, doi: 10.15761/CCRR.1000226.
- [10] T. Starch-Jensen, D. Deluiz, N. H. Bruun, and E. M. B. Tinoco, “Maxillary sinus floor augmentation with autogenous bone graft alone compared with alternate grafting materials: A systematic review and meta-analysis focusing on histomorphometric outcome,” *J. Oral Maxillofac. Res.*, vol. 11, no. 3, Sep. 2020, doi: 10.5037/jomr.2020.11302.
- [11] R. Fujita, A. Yokoyama, T. Kawasaki, and T. Kohgo, “Bone augmentation osteogenesis using hydroxyapatite and  $\beta$ -tricalcium phosphate blocks,” *J. Oral Maxillofac. Surg.*, vol. 61, no. 9, pp. 1045–1053, Sep. 2003, doi: 10.1016/S0278-2391(03)00317-3.
- [12] A. N. Rindone and W. L. Grayson, “Illuminating the regenerative microenvironment: Emerging quantitative imaging technologies for craniofacial bone tissue engineering,” *ACS Biomater. Sci. Eng.*, vol. 8, no. 11, pp. 4610–4612, Nov. 2022, doi: 10.1021/acsbiomaterials.1c01373.
- [13] H. O. Simila and A. R. Boccaccini, “Sol-gel synthesis of lithium doped mesoporous bioactive glass nanoparticles and tricalcium silicate for restorative dentistry: Comparative investigation of physico-chemical structure, antibacterial susceptibility and biocompatibility,” *Front. Bioeng. Biotechnol.*, vol. 11, no. April, pp. 1–19, Apr. 2023, doi: 10.3389/fbioe.2023.1065597.
- [14] W. H. Salem, “Preparation of bioactive composite and fibers for dental applications,” *Biomater. J.*, vol. 2, no. 2, pp. 56–71, 2023.
- [15] J. M. Gunn, J. Rekola, J. Hirvonen, and A. J. Aho, “Comparison of the osteoconductive properties of three particulate bone fillers in a rabbit model: Allograft, calcium carbonate (Biocoral®) and S53P4 bioactive glass,” *Acta Odontol. Scand.*, vol. 71, no. 5, pp. 1238–1242, Sep. 2013, doi: 10.3109/00016357.2012.757642.
- [16] R. Eivazzadeh-Keihan *et al.*, “Carbon based nanomaterials for tissue engineering of bone: Building new bone on small black scaffolds: A review,” *J. Adv. Res.*, vol. 18, no. March, pp. 185–201, 2019, doi: 10.1016/j.jare.2019.03.011.

- [17] R. H. Hurt, M. Monthieux, and A. Kane, "Toxicology of carbon nanomaterials: Status, trends, and perspectives on the special issue," *Carbon N. Y.*, vol. 44, no. 6, pp. 1028–1033, May 2006, doi: 10.1016/j.carbon.2005.12.023.
- [18] R. Niranjana and A. K. Thakur, "The Toxicological Mechanisms of Environmental Soot (Black Carbon) and Carbon Black: Focus on Oxidative Stress and Inflammatory Pathways," *Front. Immunol.*, vol. 8, no. JUN, pp. 1–20, Jun. 2017, doi: 10.3389/fimmu.2017.00763.
- [19] H. Kim *et al.*, "Ultrafine carbon black particles inhibit human lung fibroblast-mediated collagen gel contraction," *Am. J. Respir. Cell Mol. Biol.*, vol. 28, no. 1, pp. 111–121, Jan. 2003, doi: 10.1165/rcmb.4796.
- [20] B. Granum, "The effect of particles on allergic immune responses," *Toxicol. Sci.*, vol. 65, no. 1, pp. 7–17, Jan. 2002, doi: 10.1093/toxsci/65.1.7.
- [21] L. K. Vesterdal *et al.*, "Pulmonary exposure to carbon black nanoparticles and vascular effects," *Part. Fibre Toxicol.*, vol. 7, no. 1, p. 33, Dec. 2010, doi: 10.1186/1743-8977-7-33.
- [22] K. Ganguly *et al.*, "Early pulmonary response is critical for extra-pulmonary carbon nanoparticle mediated effects: Comparison of inhalation versus intra-arterial infusion exposures in mice," *Part. Fibre Toxicol.*, vol. 14, no. 1, pp. 1–17, 2017, doi: 10.1186/s12989-017-0200-x.
- [23] A. L. Lambert, "Ultrafine carbon black particles enhance respiratory syncytial virus-induced airway reactivity, pulmonary inflammation, and chemokine expression," *Toxicol. Sci.*, vol. 72, no. 2, pp. 339–346, Apr. 2003, doi: 10.1093/toxsci/kfg032.
- [24] R. You *et al.*, "Nanoparticulate carbon black in cigarette smoke induces DNA cleavage and Th17-mediated emphysema," *Elife*, vol. 4, no. Oct. 2015, pp. 1–20, Oct. 2015, doi: 10.7554/eLife.09623.
- [25] Y. Shen *et al.*, "Carbon black suppresses the osteogenesis of mesenchymal stem cells: the role of mitochondria," *Part. Fibre Toxicol.*, vol. 15, no. 1, p. 16, Dec. 2018, doi: 10.1186/s12989-018-0253-5.
- [26] H. Kim, K. Park, and M.-Y. Lee, "Biocompatible dispersion methods for carbon black," *Toxicol. Res.*, vol. 28, no. 4, pp. 209–216, Dec. 2012, doi:

10.5487/TR.2012.28.4.209.

- [27] D. Sahu, G. M. Kannan, and R. Vijayaraghavan, "Carbon black particle exhibits size dependent toxicity in human monocytes," *Int. J. Inflamm.*, vol. 2014, pp. 1–10, 2014, doi: 10.1155/2014/827019.
- [28] S. Xie, W. Li, Z. Pan, B. Chang, and L. Sun, "Mechanical and physical properties on carbon nanotube," *J. Phys. Chem. Solids*, vol. 61, no. 7, pp. 1153–1158, Jul. 2000, doi: 10.1016/S0022-3697(99)00376-5.
- [29] R. Scandurra, A. Scotto d'Abusco, and G. Longo, "A Review of the Effect of a Nanostructured Thin Film Formed by Titanium Carbide and Titanium Oxides Clustered around Carbon in Graphitic Form on Osseointegration," *Nanomaterials*, vol. 10, no. 6, p. 1233, Jun. 2020, doi: 10.3390/nano10061233.
- [30] F. Veronesi *et al.*, "Osseointegration is improved by coating titanium implants with a nanostructured thin film with titanium carbide and titanium oxides clustered around graphitic carbon," *Mater. Sci. Eng. C*, vol. 70, pp. 264–271, 2017, doi: 10.1016/j.msec.2016.08.076.
- [31] V. Kumaravel *et al.*, "Antimicrobial TiO<sub>2</sub> nanocomposite coatings for surfaces, dental and orthopaedic implants," *Chem. Eng. J.*, vol. 416, no. February, p. 129071, 2021, doi: 10.1016/j.cej.2021.129071.
- [32] K. M. Sajesh, K. Kiran, S. V. Nair, and R. Jayakumar, "Sequential layer-by-layer electrospinning of nano SrCO<sub>3</sub>/PRP loaded PHBV fibrous scaffold for bone tissue engineering," *Compos. Part B Eng.*, vol. 99, pp. 445–452, 2016, doi: 10.1016/j.compositesb.2016.06.026.
- [33] C. Luo *et al.*, "Biomimetic open porous structured core-shell microtissue with enhanced mechanical properties for bottom-up bone tissue engineering," *Theranostics*, vol. 9, no. 16, pp. 4663–4677, 2019, doi: 10.7150/thno.34464.
- [34] G. A. E. Prince *et al.*, "Yolk-porous shell biphasic bioceramic granules enhancing bone regeneration and repair beyond homogenous hybrid," *Mater. Sci. Eng. C*, vol. 100, no. February, pp. 433–444, 2019, doi: 10.1016/j.msec.2019.03.026.
- [35] Z. Asgari-Fard, M. Sabet, and M. Salavati-Niasari, "Synthesis and characterization of strontium carbonate nanostructures via simple hydrothermal

- method,” *High Temp. Mater. Process.*, vol. 35, no. 2, pp. 215–220, Feb. 2016, doi: 10.1515/htmp-2014-0232.
- [36] J. Kim and S. Kang, “Stable phase domains of the  $\text{TiO}_2$ – $\text{Ti}_3\text{O}_5$ – $\text{Ti}_2\text{O}_3$ – $\text{TiO}$ – $\text{Ti}(\text{C}_x\text{O}_y)$ – $\text{TiC}$  system examined experimentally and via first principles calculations,” *J. Mater. Chem. A*, vol. 2, no. 8, pp. 2641–2647, 2014, doi: 10.1039/C3TA14633B.
- [37] J. He *et al.*, “The anatase phase of nanotopography titania plays an important role on osteoblast cell morphology and proliferation,” *J. Mater. Sci. Mater. Med.*, vol. 19, no. 11, pp. 3465–3472, Nov. 2008, doi: 10.1007/s10856-008-3505-3.
- [38] Z. Xu, H. Lu, J. Lu, C. Lv, X. Zhao, and G. Wang, “Enhanced osteogenic activity of Ti alloy implants by modulating strontium configuration in their surface oxide layers,” *RSC Adv.*, vol. 8, no. 6, pp. 3051–3060, 2018, doi: 10.1039/C7RA10807A.
- [39] Y. Wang, D. Zhang, C. Wen, and Y. Li, “Processing and characterization of  $\text{SrTiO}_3$ – $\text{TiO}_2$  nanoparticle–nanotube heterostructures on titanium for biomedical applications,” *ACS Appl. Mater. Interfaces*, vol. 7, no. 29, pp. 16018–16026, Jul. 2015, doi: 10.1021/acsami.5b04304.
- [40] M. Demirel, A. İ. Kaya, and B. Aksakal, “Synthesizing the strontium carbonate and silver doped bioceramic bone graft: Structure-properties and cell viability,” *Int. J. Appl. Ceram. Technol.*, vol. 17, no. 1, pp. 333–341, Jan. 2020, doi: 10.1111/ijac.13316.
- [41] M. Lopreiato *et al.*, “Nanostructured TiC layer is highly suitable surface for adhesion, proliferation and spreading of cells,” *Condens. Matter*, vol. 5, no. 2, p. 29, Apr. 2020, doi: 10.3390/condmat5020029.
- [42] L. Lv, K. Li, Y. Xie, Y. Cao, and X. Zheng, “Enhanced osteogenic activity of anatase  $\text{TiO}_2$  film: Surface hydroxyl groups induce conformational changes in fibronectin,” *Mater. Sci. Eng. C*, vol. 78, pp. 96–104, Sep. 2017, doi: 10.1016/j.msec.2017.04.056.
- [43] W. Chen *et al.*, “Nanotopography influences adhesion, spreading, and self-renewal of human embryonic stem cells,” *ACS Nano*, vol. 6, no. 5, pp. 4094–

- 4103, May 2012, doi: 10.1021/nn3004923.
- [44] W. Querido, M. Farina, and K. Anselme, “Strontium ranelate improves the interaction of osteoblastic cells with titanium substrates: Increase in cell proliferation, differentiation and matrix mineralization,” *Biomatter*, vol. 5, no. 1, p. e1027847, Jan. 2015, doi: 10.1080/21592535.2015.1027847.
- [45] B. C. Ward and T. J. Webster, “The effect of nanotopography on calcium and phosphorus deposition on metallic materials in vitro,” *Biomaterials*, vol. 27, no. 16, pp. 3064–3074, Jun. 2006, doi: 10.1016/j.biomaterials.2005.12.027.
- [46] Q. Zhang, L. Xiao, and Y. Xiao, “Porous nanomaterials targeting autophagy in bone regeneration,” *Pharmaceutics*, vol. 13, no. 10, p. 1572, Sep. 2021, doi: 10.3390/pharmaceutics13101572.
- [47] H. N. Soe, M. Khangkhamano, S. Sangkert, J. Meesane, and R. Kokoo, “TiC-coated carbon particles as bioactive substrates for inducing of mineralization in bone healing,” *Mater. Lett.*, vol. 229, pp. 118–121, Oct. 2018, doi: 10.1016/j.matlet.2018.06.125.
- [48] F. M. Lima, F. M. Martins, P. H. F. Maia Júnior, A. F. L. Almeida, and F. N. A. Freire, “Nanostructured titanium dioxide average size from alternative analysis of Scherrer’s Equation,” *Matéria (Rio Janeiro)*, vol. 23, no. 1, Mar. 2018, doi: 10.1590/s1517-707620170001.0301.
- [49] M. K. Gupta and P. K. Sood, “Surface roughness measurements in NFMQL assisted turning of titanium alloys: An optimization approach,” *Friction*, vol. 5, no. 2, pp. 155–170, Jun. 2017, doi: 10.1007/s40544-017-0141-2.
- [50] R. Florencio-Silva, G. R. D. S. Sasso, E. Sasso-Cerri, M. J. Simões, and P. S. Cerri, “Biology of bone tissue: Structure, function, and factors that influence bone cells,” *Biomed Res. Int.*, vol. 2015, pp. 1–17, 2015, doi: 10.1155/2015/421746.
- [51] M. Ansari, “Bone tissue regeneration: biology, strategies and interface studies,” *Prog. Biomater.*, vol. 8, no. 4, pp. 223–237, Dec. 2019, doi: 10.1007/s40204-019-00125-z.
- [52] C. N. Elias, J. H. C. Lima, R. Valiev, and M. A. Meyers, “Biomedical applications of titanium and its alloys,” *JOM*, vol. 60, no. 3, pp. 46–49, Mar.

- 2008, doi: 10.1007/s11837-008-0031-1.
- [53] L. Zhang and L. Chen, “A Review on biomedical titanium alloys: Recent progress and prospect,” *Adv. Eng. Mater.*, vol. 21, no. 4, p. 1801215, Apr. 2019, doi: 10.1002/adem.201801215.
- [54] B. Feng, J. Weng, B. C. Yang, S. X. Qu, and X. D. Zhang, “Characterization of surface oxide films on titanium and adhesion of osteoblast,” *Biomaterials*, vol. 24, no. 25, pp. 4663–4670, Nov. 2003, doi: 10.1016/S0142-9612(03)00366-1.
- [55] L. Mullen, R. C. Stamp, W. K. Brooks, E. Jones, and C. J. Sutcliffe, “Selective laser melting: A regular unit cell approach for the manufacture of porous, titanium, bone in-growth constructs, suitable for orthopedic applications,” *J. Biomed. Mater. Res. Part B Appl. Biomater.*, vol. 89B, no. 2, pp. 325–334, May 2009, doi: 10.1002/jbm.b.31219.
- [56] L. Zhao, L. Liu, Z. Wu, Y. Zhang, and P. K. Chu, “Effects of micropitted/nanotubular titania topographies on bone mesenchymal stem cell osteogenic differentiation,” *Biomaterials*, vol. 33, no. 9, pp. 2629–2641, Mar. 2012, doi: 10.1016/j.biomaterials.2011.12.024.
- [57] S. Cavalu *et al.*, “Nanoparticles and nanostructured surface fabrication for innovative cranial and maxillofacial surgery,” *Materials (Basel)*, vol. 13, no. 23, p. 5391, Nov. 2020, doi: 10.3390/ma13235391.

APPENDIX I

## RESEARCH ARTICLE

# Bioactive core–shell structure of TiC/TiO<sub>2</sub>/SrCO<sub>3</sub> coating on carbon black particles for bone tissue formation: Fabrication, characterization, and biological functions

Hnin Nandar Soe<sup>1</sup> | Jirut Meesane<sup>2</sup> | Rungrote Kokoo<sup>3</sup> |  
Matthana Khangkhamano<sup>1</sup> 

<sup>1</sup>Department of Mining and Materials Engineering, Faculty of Engineering, Prince of Songkla University, Hat Yai, Songkhla, Thailand

<sup>2</sup>Institute of Biomedical Engineering, Faculty of Medicine, Prince of Songkla University, Hat Yai, Songkhla, Thailand

<sup>3</sup>Department of Chemical Engineering, Faculty of Engineering, King Mongkut's University of Technology North Bangkok, Bangkok, Thailand

## Correspondence

Matthana Khangkhamano, Department of Mining and Materials Engineering, Faculty of Engineering, Prince of Songkla University, Hat Yai 90110, Songkhla, Thailand.

Email: kmatthana@eng.psu.ac.th

## Funding information

National Science, Research and Innovation Fund (NSRF) and Prince of Songkla University, Grant/Award Number: ENG6505057S

## Abstract

Although carbon-based nanomaterials, such as carbon nanotubes, graphene, and carbon dots, have attracted much attention for bone tissue regeneration and engineering due to the advantages of being lightweight, mechanical stability, and remarkable ability for bone repair, their toxicity and dispersity are the most concern and greatly limiting their clinical uses. In this article, the surface modification of carbon black particles based on core–shell structure design as a promising candidate material for bone tissue engineering applications is presented. TiC/TiO<sub>2</sub>/SrCO<sub>3</sub>-coated carbon black particles were prepared via molten salt synthesis and hydrothermal process at various temperatures to study the effects of temperature on crystal structure, morphologies, surface wettability, and biological functions. Phase composition, morphologies, and elemental distributions were studied by X-ray diffraction, field-emission scanning electron microscope, and energy-dispersive X-ray spectroscopy, respectively. Cell proliferation, cell viability, alkaline phosphatase (ALP) activity, and calcium deposition were also investigated. The investigation showed that the reaction temperature played an important role in the crystallinity, phase formation, nanotopography, and biological functions of the particles. The particles treated at 250°C offered favored surface properties of roughness, composition, crystallite size, and wettability for cell adhesion, proliferation, ALP activity, and calcium deposition. As a result, these bioactive core–shell particles would be a promising filler material for bone tissue engineering applications.

## KEYWORDS

bioactive core–shell particle, bone tissue formation, carbon-based nanomaterial, surface modification

## 1 | INTRODUCTION

Worldwide, a number of patients suffer from bone defects, either trauma or diseases.<sup>1</sup> In severe cases, patients need to be treated with bioactive substrates or implants to enhance bone healing. Traditional biomaterials, including metals, polymers, and ceramics, have been widely used as bone tissue engineering scaffolds to treat bone defects. Their clinical applications, however, have been limited to some extent. For instance, metals/alloys cause ion release for long-term uses and are likely to initiate allergic responses and adverse reactions due to corrosion problem.<sup>2</sup> In particular, for titanium and its alloys, their nature of being biologically inert restricts long-term application in a human body because the implants are encapsulated by fibrous tissue resulting in a lack of osteointegration.<sup>3</sup> Biopolymers show an appropriate fixation, yet they are likely to release monomers when implanted due to the degradation of the implants.<sup>4</sup> Bioceramics, such as calcium phosphate, hydroxyapatite, and bioglasses, possess the good biocompatibility and promotion of wound healing. However, their low fracture toughness inhibits the uses in stress-bearing areas.<sup>5</sup> Besides, some of the bioceramics such as alumina and zirconia are bioinert materials that lack the character of osteoconduction and the capability of chemical bonding with human tissue. Therefore, biomaterials with bioactive functions having the potential to allow new bone formation and growth as well as mechanical properties matching the natural bone are in high demand.

Recently, a variety of carbon-based materials, such as carbon nanotubes, graphene, and carbon dots, attract significant interests for bone tissue engineering applications, either as a matrix or a reinforcing material, because of their unique structure and properties, including good mechanical strength, tunable surface functionalities, high biocompatibility, and commercial availability. They offer remarkable abilities for bone tissue regeneration, cell proliferation, and osteogenic differentiation, whereas carbon black particles (CBs) were found to have a size-dependent effect on *in vitro* cultures<sup>6</sup> and have been used as a representative carbonaceous toxicant in air pollution studies.<sup>7</sup> Several studies show that ultrafine CBs (less than 100 nm) are toxic causing disorders on many biological systems and, hence, adverse effects on health, such as respiratory and lung diseases,<sup>8</sup> allergic immune response,<sup>9</sup> vascular effects,<sup>10</sup> early pulmonary response,<sup>11</sup> inflammatory response,<sup>12</sup> and genotoxicity.<sup>13</sup> The toxicity of nanoscale CBs is attributed to their high surface area and surface reactivity<sup>14</sup> as well as the ability to adsorb toxic substances.<sup>15</sup> The effects of nanosized CBs on bone health and osteogenesis, however, remain unclear. In this matter, a limited number of studies were reported. Shen

et al.<sup>16</sup> reported the effect of nanosized CBs on the osteogenesis of mesenchymal stem cells (MSCs) that the CBs inhibited the osteogenic differentiation of MSCs, reduced the activity of alkaline phosphatase (ALP), and damaged the mitochondrial fusion and fission during osteogenesis. Furthermore, the dispersion of the CBs in liquid media seemed to be a difficulty for their research due to the high aggregation and poor wettability of the particles. Likely, Kim et al.<sup>17</sup> investigated the dispersity of CBs in various liquid media, including distilled water, Krebs-Ringer solution (KR), physiological salt solution (PSS), and biological buffer solutions (cell culture media and blood plasma). The results indicated that nanosized CBs had a higher degree of agglomeration and incomplete dispersion in KR, PSS, and biological buffer solutions than the coarse CBs. Furthermore, Sahu et al.<sup>18</sup> presented that nanosized CBs (~50 nm) had greater toxicity and inflammatory response than micron-sized ones (~500 nm) in human monocytes.

Based on literatures, nanosized CBs cause a greater inflammatory response than coarse ones. Those carbon black particles, however, were used in the forms of both nanoscale and bare surfaces that were found to be highly aggregated and have poor dispersion, high surface reactivity, and toxicity. In this study, submicron CBs with surface modification were used to minimize those adverse effects on wettability and biological systems as well as to create a lightweight bioactive material as a reinforcing agent for bone tissue engineering applications. In this paper, surface coating of CBs was performed via molten salt synthesis (MSS) and hydrothermal process. The coating layer was designed to be composed of TiC/TiO<sub>2</sub>/SrCO<sub>3</sub> nanocomposite that was chemically coated on CB surfaces. TiC could improve surface wettability, hardness, wear resistance, compressive strength, biocompatibility, and osseointegration,<sup>19</sup> whereas TiO<sub>2</sub> offers biocompatibility, low cytotoxicity, stability in body fluids, and corrosion resistance,<sup>20</sup> favorable molecular response, and osseointegration.<sup>21</sup> SrCO<sub>3</sub> enhances bioactivity, biocompatibility, bone repair, and new bone formation.<sup>22</sup> To our knowledge, the designed core-shell particles having multi-bioceramic phases of TiC/TiO<sub>2</sub>/SrCO<sub>3</sub> coating on non-wettable carbon black surfaces as a lightweight bioactive material applied in bone tissue engineering applications have never been studied elsewhere.

## 2 | EXPERIMENTAL PROCEDURES

### 2.1 | Raw materials

Carbon blacks (CBs, N990, 99% pure, Sigma-Aldrich) with an averaged particle size of 400 nm and metallic titanium powder (Ti, 100 mesh, 99.7% pure, Sigma-Aldrich)

TABLE 1 Lists of samples and synthesis conditions

Samples	Details
CBs	As-received carbon black particles
TCBs	TiC-coated carbon black particles via molten salt synthesis at 900°C for 4 h
HT180	Hydrothermal synthesis of the TCBs in distilled water at 180°C
SrHT180	Hydrothermal synthesis of the TCBs in a 0.1 M (SrNO <sub>3</sub> ) <sub>2</sub> solution at 180°C
SrHT200	Hydrothermal synthesis of the TCBs in a 0.1 M (SrNO <sub>3</sub> ) <sub>2</sub> solution at 200°C
SrHT225	Hydrothermal synthesis of the TCBs in a 0.1 M (SrNO <sub>3</sub> ) <sub>2</sub> solution at 225°C
SrHT250	Hydrothermal synthesis of the TCBs in a 0.1 M (SrNO <sub>3</sub> ) <sub>2</sub> solution at 250°C
Control	Agarose hydrogel solution without particles

Abbreviation: CBs, carbon black particles.

were used as raw materials for fabricating the core-shell structure of TiC-coated carbon black particles. Potassium chloride (KCl) (99.9% pure, Ajax Finechem) was used as a reaction media for MSS. Strontium nitrate (SrNO<sub>3</sub>)<sub>2</sub> (ACS reagent, 99% pure, Sigma-Aldrich) was used as a precursor for SrCO<sub>3</sub> formation via hydrothermal process.

## 2.2 | Preparation of TiC-coated carbon black particles via molten salt synthesis

TiC-coated carbon black particles were prepared via MSS.<sup>23–25</sup> Ti and carbon black reactants were mixed in a molar ratio of 1:8 using an agate mortar and then combined with KCl. The mixture was placed in an alumina crucible covered with its lid and loaded into an alumina-tube furnace. The furnace was heated to 900°C for 4 h under argon gas protection. After heating, the reacted mass was repeatedly washed with distilled water to remove residual salt and gain the final product. The samples obtained from this process were designated as TCBs. The TCBs were then used as a raw material for preparing TiC/TiO<sub>2</sub>/SrCO<sub>3</sub>-coated carbon black particles via hydrothermal method as presented in the next section.

## 2.3 | Preparation of TiC/TiO<sub>2</sub>/SrCO<sub>3</sub>-coated carbon black particles via hydrothermal process

Hydrothermal synthesis<sup>26,27</sup> of the TCBs was conducted at various temperatures to seek an optimum condition for producing a favored surface for cell activities. As-synthesized TCBs of 0.5 g were loaded into a 0.1 M (SrNO<sub>3</sub>)<sub>2</sub> solution and sonicated for 15 min to obtain a homogeneous suspension. The suspension was loaded into a Teflon container (10 ml volume), placed in an autoclave reactor, sealed tightly, and heated to 180, 200, 225, and 250°C for 2 h. After that, the reactor was cooled naturally in an ambient condition. The obtained sample was filtrated

and thoroughly washed with distilled water prior to dry in an oven and powder characterization. All hydrothermal samples were labeled according to reaction temperature as presented in Table 1.

## 2.4 | Sample characterization

Phases and crystallinity of the product powders were identified by X-ray diffraction (XRD) (model—X'Pert MPD, PHILIPS, the Netherlands). Spectra were recorded at 30 mA and 40 kV using Ni-filtered CuK<sub>α</sub> radiation. The scan rate (2θ) was 3°/min with a step size of 0.05. ICDD cards used for phase identification are TiC (01-076-7070), TiO<sub>2</sub>-anatase (01-075-2547), SrCO<sub>3</sub> (00-005-0418), Ti<sub>2</sub>O<sub>3</sub> (00-043-1033), TiO<sub>2</sub>-rutile (01-079-6031), and Ti<sub>3</sub>O<sub>5</sub> (01-083-7068). The crystallite size was evaluated using the following Scherrer equation<sup>28</sup>:

$$D = \frac{K\lambda}{(\beta\cos\theta)} \quad (1)$$

where  $D$ ,  $K$ ,  $\lambda$ ,  $\beta$ , and  $\theta$  represent average crystallite size (nm), the Scherrer constant, X-ray wavelength, and full width at half maximum of the diffraction angle and Bragg angle, respectively.

Morphology and microstructure were observed using a field-emission scanning electron microscope (FE-SEM) (model—Apreo, FEI, Czech Republic) with an accelerating voltage of 5 kV. Elemental composition was also evaluated using energy-dispersive X-ray spectroscopy (EDX) equipped with a FE-SEM. The product powders were dispersed in isopropyl alcohol to avert agglomeration. The samples were put into sticky carbon films and characterized after gold coating. The roughness of the samples was evaluated using arithmetic average roughness ( $R_a$ )<sup>29</sup>:

$$R_a = \frac{1}{n_x n_y} \sum_{i=1}^{n_x} \sum_{j=1}^{n_y} [Z(i, j) - Z_{ave}] \quad (2)$$

where  $R_a$ ,  $i$  and  $j$ ,  $n_x$  and  $n_y$ , and  $Z(i,j)$  and  $Z_{ave}$  represent the arithmetic average roughness, pixels in  $x$  and  $y$  directions, the maximum number of pixels in two directions, the topography data for the surface, and the height of the average surface, respectively.

## 2.5 | Wettability measurement

Wettability of the samples was measured using an OCA-15EC contact angle (CA) meter. Contact angle is used to determine the hydrophobicity and hydrophilicity of a sample surface. To prepare a sample surface for the test, 0.1 g of the product particles was dispersed in ethanol by ultrasonication for 5 min and dropped on a glass substrate. The substrate was then stored air-dry before being used for experiments. To measure the contact angle,<sup>30,31</sup> the prepared substrate was placed on a stage of the CA meter at ambient temperature. A water droplet of 2  $\mu$ l was then released from a dosing needle onto the surface and allowed to equilibrate for 10 s. Using sessile drop method, the static contact angle between the droplet and surface was measured, whereas the droplet was sitting on the surface using a built-in drop shape analyzer. An average value was measured at three different locations of the surface.

## 2.6 | Biological testing

### 2.6.1 | Materials and method

The samples were divided into six groups according to experimental conditions, including the control, HT180, SrHT180, SrHT200, SrHT225, and SrHT250. Agarose hydrogel solution without particles was used as the control. The rest groups were prepared by mixing with 500 mg of sample particles and 1% agarose hydrogel solution. Then, the mixed solution was poured into a plastic mold and dried in ambient condition for 24 h. The dried specimens were cut with a razor blade into 10 mm  $\times$  10 mm for cell culture. The samples were washed twice with 75% ethanol for sterilization and rinsed in phosphate-buffered saline (PBS) three times to remove residual ethanol. Each sample was transferred to a 24-well culture plate for biological tests.

### 2.6.2 | Cell culture

The MG-63 osteoblast cell was used to study the biocompatibility and differentiation of the sample particles. The MG-63 at a density of  $2 \times 10^5$  cells were seeded

into agarose hydrogel containing the sample particles and cultured in alpha-MEM media ( $\alpha$ -MEM, Gibco™, Invitrogen, Carlsbad, CA, USA) with the addition of 1% penicillin/streptomycin, 0.1% fungizone, and 10% fetal bovine serum at 37°C in an incubator. The media was changed every 3–4 days during culturing. In the differentiation stage, the osteoblast cells were cultured in an osteogenic supplemented (OS) medium containing 20 mM  $\beta$ -glycerophosphate, 50  $\mu$ M ascorbic acid, and 100 nM dexamethasone, Sigma-Aldrich.

### 2.6.3 | Cell viability

The viability of MG-63 osteoblast cells on the particle samples at days 1 and 5 was assessed with fluorescein diacetate (FDA). Acetone was used to dissolve the FDA at a concentration of 5 mg/ml. Before staining, the cells were washed with PBS. Next, 1 ml of fresh media and 5  $\mu$ l of FDA solution were added on the sample surface and incubated for 5 min. The samples were washed with PBS for three times before being examined under a fluorescence microscope.

### 2.6.4 | Cell proliferation

The cell proliferation and biocompatibility were assessed by PrestoBlue assay (PrestoBlue Cell Viability Reagent, Invitrogen, USA) at days 1, 3, 5, and 7. The PrestoBlue was mixed with the fresh media at a ratio of 1–9 before being added to the particle samples and then incubated for 1 h at 37°C. The optical density (OD) measurement at a wavelength of 600 nm was selected for resazurin reaction between the cells and the PrestoBlue. After testing, the samples were washed with PBS and cultured for cell-proliferation measurements from day 1 to day 7.

### 2.6.5 | Alkaline phosphatase (ALP) activity

The osteoblast cells were cultured in OS media on days 7, 14, and 21 for ALP measurements. The samples were rinsed with PBS after removing the media. The 800  $\mu$ l of lysis solution, including 1% Triton X in PBS, was added onto the samples, frozen at  $-80^\circ\text{C}$  for 1 h, and then left at room temperature for 1 h for three cycles. The samples were crushed and loaded into Eppendorf tubes. A centrifuge machine (12000 rpm) was used to separate the supernatant from the pellet. The supernatant was used then for ALP detection. ALP activity was investigated using a colorimetric assay kit (Abcam, Cambridge, UK). The ALP was observed at an OD of 405 nm.

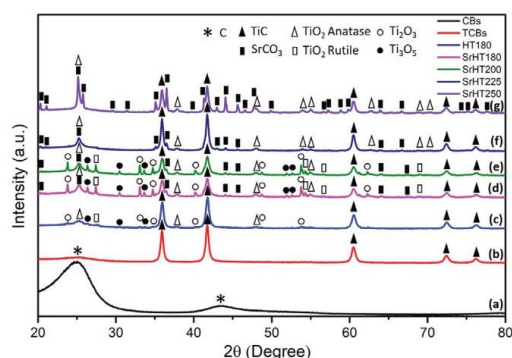


FIGURE 1 X-ray diffraction (XRD) curves of (A) as-received carbon black particles (CBs), (B) TiC-coated carbon black particles (TCBs) via molten salt synthesis and the TCBs treated for 2 h: (C) in distilled water at 180°C (HT180) and in a 0.1 M  $(\text{SrNO}_3)_2$  solution at (D) 180°C (SrHT180), (E) 200°C (SrHT200), (F) 225°C (SrHT225), and (G) 250°C (SrHT250) via hydrothermal method

### 2.6.6 | Calcium deposition

The cell-lysis solutions were used for calcium deposition measurement (Calcium Colorimetric Assay Kit, MAK022, Sigma-Aldrich, USA) at days 7, 14, and 21 following the manufacturer's instructions. The 30  $\mu\text{l}$  of supernatant was added to 96-well plates before adjusting the volume to 50  $\mu\text{l}$  with deionized water. After that, 60  $\mu\text{l}$  of calcium assay buffer and 90  $\mu\text{l}$  of chromogenic reagent were mixed in each well. The well plates were then incubated for 10 min at 37°C and then measured at a wavelength of 575 nm.

### 2.7 | Statistical analysis

All data were shown as mean  $\pm$  standard deviation. The results were statistically compared by one-way analysis of variance and Tukey's honestly significant difference test (SPSS 16.0 software package). Statistical significance was set at  $p < .05$  and  $p < .005$ .

## 3 | RESULTS AND DISCUSSION

### 3.1 | Phase composition and structural study

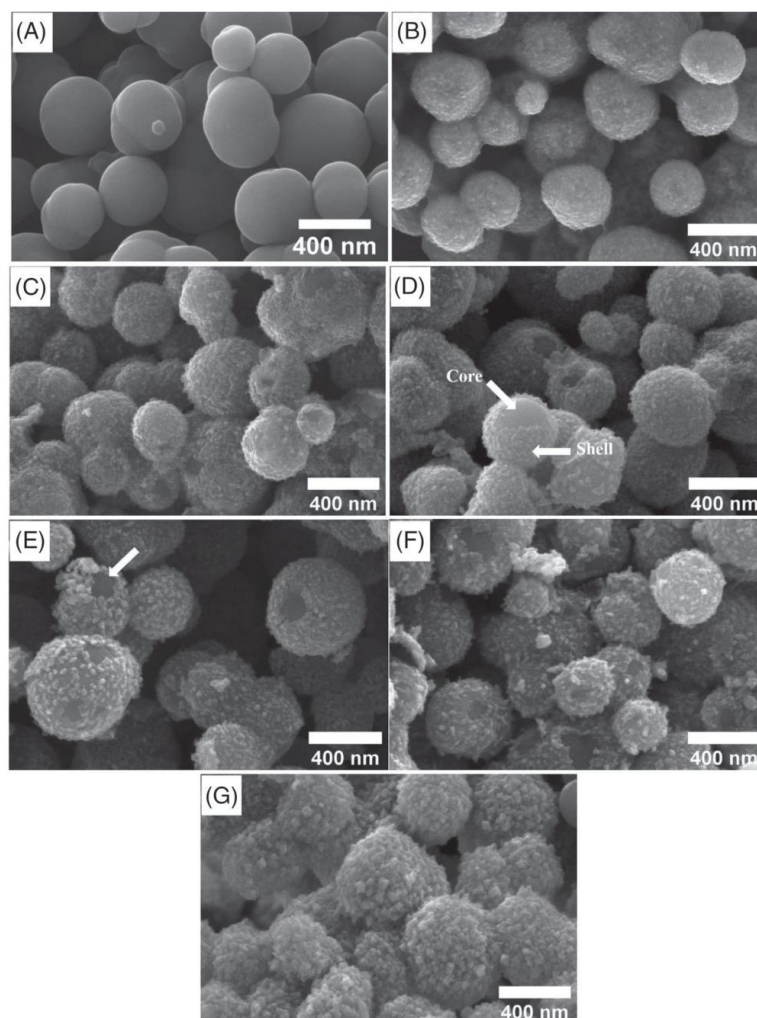
Figure 1 shows XRD curves of as-received CBs and as-prepared samples of TCBs, HT180, SrHT180, SrHT200, SrHT225, and SrHT250. Two broad peaks of C phase (ICDD card 00-041-1487) were observed, without any

TABLE 2 Phase composition, crystallite size, and surface roughness of the samples

Samples	Crystallite size (nm)			Surface roughness (nm)
	TiC	TiO <sub>2</sub> Anatase	SrCO <sub>3</sub>	
CBs	–	–	–	8
TCBs	39.54	–	–	17
HT180	19.35	28.38	–	21
SrHT180	27.48	32.91	57.53	23
SrHT200	28.97	35.13	71.02	25
SrHT225	33.61	36.33	71.39	30
SrHT250	42.44	38.08	76.85	43

Abbreviation: CBs, carbon black particles.

other impurity phases, on the uncoated CBs at  $2\theta = 25.18^\circ$  and  $43.5^\circ$  attributing to an amorphous nature of as-received CB particles (Figure 1A). After MSS (TCBs), TiC (ICDD card 01-076-7070) and C phases were found (Figure 1B). Unreacted Ti and other intermediate phases were undetected suggesting the complete formation of TiC via MSS. Once the TCBs were hydrothermally treated with and without  $\text{Sr}(\text{NO}_3)_2$ , a number of additional phases were formed according to the synthesis temperature. At 180°C, TiC was observed as a major phase, whereas anatase TiO<sub>2</sub> (ICDD card 01-075-2547), rutile TiO<sub>2</sub> (ICDD card 01-079-6029), Ti<sub>2</sub>O<sub>3</sub> (ICDD card 01-074-0324), and Ti<sub>3</sub>O<sub>5</sub> (ICDD card 01-083-7068) were found as minor phases (Figure 1C). For the samples treated with  $\text{Sr}(\text{NO}_3)_2$ , orthorhombic SrCO<sub>3</sub> (ICDD card 01-078-4340) was additionally found at 180°C, and its crystallinity increased obviously with temperature (Figure 1D). The observation of titanium oxide phases was attributed to the oxidation of TiC during hydrothermal treatment. The presence of SrCO<sub>3</sub> was due to the reaction of  $\text{Sr}^{2+}$  with CO<sub>2</sub> in the reaction solution.<sup>32</sup> Furthermore, in comparison with the HT180, the SrHT180 offered remarkably higher and sharper Ti<sub>2</sub>O<sub>3</sub> and Ti<sub>3</sub>O<sub>5</sub> peaks with a decrease in TiC peak intensity, pointing out an accelerating oxidation of TiC under the presence of  $\text{Sr}(\text{NO}_3)_2$ , a strong oxidizing agent. At 200°C (the SrHT200), the phases presented were unchanged (Figure 1E). At 225°C, interestingly, rutile TiO<sub>2</sub>, Ti<sub>2</sub>O<sub>3</sub>, and Ti<sub>3</sub>O<sub>5</sub> disappeared, whereas TiC became more pronounced (Figure 1F). The disappearance of those intermediate compounds could be due to their instability under the hydrothermal conditions at a temperature above or equal to 225°C resulting in the production of TiC, which might be achieved by carbothermal reduction through the pathway:  $\text{TiO}_2 \rightarrow \text{Ti}_3\text{O}_5 \rightarrow \text{Ti}_2\text{O}_3 \rightarrow \text{Ti}(\text{C}_x\text{O}_y) \rightarrow \text{TiC}$ .<sup>33</sup> On further increasing temperature to 250°C (Figure 1G), SrCO<sub>3</sub> and anatase TiO<sub>2</sub> peak intensity increased due to crystal growth, whereas TiC decreased because of high oxidation rate gained. In addition, average



**FIGURE 2** Field-emission scanning electron microscopy (FE-SEM) images of (A) as-received carbon black particles (CBs), (B) TiC-coated carbon black particles (TCBs) via molten salt synthesis and the TCBs treated for 2 h in (C) distilled water at 180°C (HT180) and a 0.1 M  $(\text{SrNO}_3)_2$  solution at (D) 180°C (SrHT180), (E) 200°C (SrHT200), (F) 225°C (SrHT225), and (G) 250°C (SrHT250) via hydrothermal method. Scale bar = 400 nm

crystallite sizes are estimated from Equation (1) and are demonstrated in Table 2. It was found that crystallite size increased with reaction temperature. The synthesis temperature, therefore, played an important role on phase composition and crystallite size of the nanocomposites.

Figure 2 shows FE-SEM images of the as-received CBs and as-synthesized TCBs, HT180, SrHT180, SrHT200, SrHT225, and SrHT250. Before MSS, as-received CB particles were in spherical shapes with a diameter of approx-

imately 400 nm and smooth surfaces (Figure 2A). After MSS, clearly, the TCBs (Figure 2B) remained spherical shapes and sizes of 400 nm, but the surfaces were rough due to the formation of dense TiC nanocrystals (shell) coating on carbon surfaces (core). This indicated that core-shell structure was generated after MSS. After hydrothermal process at 180–250°C (Figure 2C–G), shapes and sizes of the materials remain unchanged, pointing out that hydrothermal temperature has no effect on shapes and sizes of the carbon black particles. Unlike previous

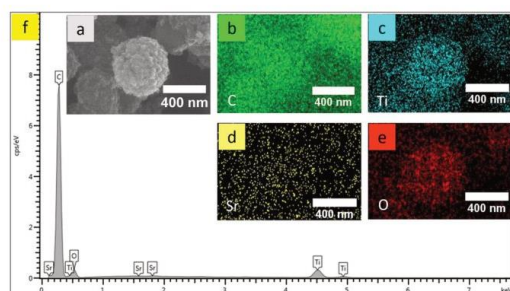


**FIGURE 3** Energy-dispersive X-ray elemental mapping analysis of the SrHT250 after hydrothermal synthesis at 250°C for 2 h in a 0.1 M (SrNO<sub>3</sub>)<sub>2</sub> solution at a magnification of 300 000×: (A) SEM image undertaken for energy-dispersive X-ray spectroscopy (EDX) technique; (B–E) the corresponding elemental mapping of C, Ti, Sr, and O, respectively; (F) EDX spectrum of the SrHT250. Scale bar = 400 nm

study,<sup>34</sup> hydrothermal temperature governed the morphology that particles gradually changed from granular to nanotube with an increased temperature. However, surface feature, crystallite size, and roughness were found to be modified depending on hydrothermal temperature. As shown in Table 2, the crystallite size of the coating components: TiC, TiO<sub>2</sub>, and SrCO<sub>3</sub> seemed to be increased with temperature. Not only that but also coating of CBs with TiC significantly increased the surface roughness from 8 nm (the uncoated CBs) to 17 nm (the TCBs). After oxidation, the roughness increased considerably with temperature from 23 nm (the SrHT180) to 43 nm (the SrHT250). The observations indicated the effect of temperature on the crystallite size and roughness of the products. Moreover, the formation of nanosized holes was noticed on the hydrothermal product particles because the temperature was 180°C. This revealed clearly the fresh C (core) underneath the crystalline coating (shell) as depicted by the arrows in Figure 2D. The core was attributed to only unreacted C and the shell was composed of TiC along with its oxidation products and SrCO<sub>3</sub>. Elemental distributions on the SrHT250 particles were performed and are demonstrated in Figure 3. Figure 3A represents the FE-SEM image undertaken for the EDX analysis. Figure 3B–E shows the corresponding elemental mapping of C, Ti, Sr, and O, respectively. Obviously, the particles were composed of Ti, C, O, and Sr and were distributed uniformly on the surfaces. Figure 3F illustrates SEM-EDX spectra of the particles where C was the main component attributed to the fresh C core, the TiC, and SrCO<sub>3</sub> on the coatings. Ti and O were minor components that corresponded to TiC, TiO<sub>2</sub>,

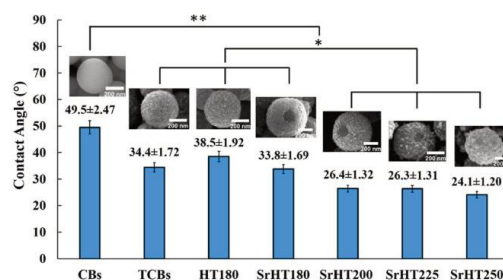


**FIGURE 4** Contact angle measurements of as-received carbon black particles (CBs), TiC-coated carbon black particles (TCBs), and the hydrothermal samples synthesized at various temperatures. The inset field-emission scanning electron microscopy (FE-SEM) images demonstrate surface features of the samples. Statistical significance was set at “\*”  $p < .05$  and “\*\*\*”  $p < .005$ . “\*\*\*” is significant difference from other groups. “\*\*” is significant difference between two groups of low temperature (TCBs, HT180, and SrHT180) and high temperature (SrHT200, SrHT225, and SrHT250). Scale bar = 200 nm

and SrCO<sub>3</sub> phases on the coatings. Sr was a trace element detected on the mapping attributing to SrCO<sub>3</sub> phase on the coatings.

### 3.2 | Wettability measurement

Figure 4 shows the contact angle measurement on as-received CBs, TCBs, HT180, SrHT180, SrHT200, SrHT225, and SrHT250. The CBs were used as a control. The contact angles for the CBs and TCBs were  $49.5^\circ \pm 2.47^\circ$  and  $34.4^\circ \pm 1.72^\circ$ , respectively, pointing out an enhancement in the wettability of the CB particles when coated with TiC. After hydrothermal treatment, as compared to the control, wettabilities of the samples were greatly improved with the increased hydrothermal temperature: from  $33.8^\circ \pm 1.69^\circ$  at 180°C (SrHT180) to  $24.1^\circ \pm 1.20^\circ$  at 250°C (SrHT250). Furthermore, although reaction temperature is identical, the particles (SrHT180) having SrCO<sub>3</sub> demonstrated a better wettability than those (HT180) without SrCO<sub>3</sub>. The existence of anatase TiO<sub>2</sub> nanocrystals on the particle surfaces was also claimed to increase wettability as reported by He et al.<sup>35</sup> that anatase TiO<sub>2</sub> exhibited good surface wettability than the rutile phase. Therefore, the marked change in contact angle value was attributed to crystallite size, surface roughness, and phase composition that are governed by reaction temperature. Note that the wettability behavior of materials can be adjusted by reaction temperature, and such surface property plays an important role for cell adhesion.

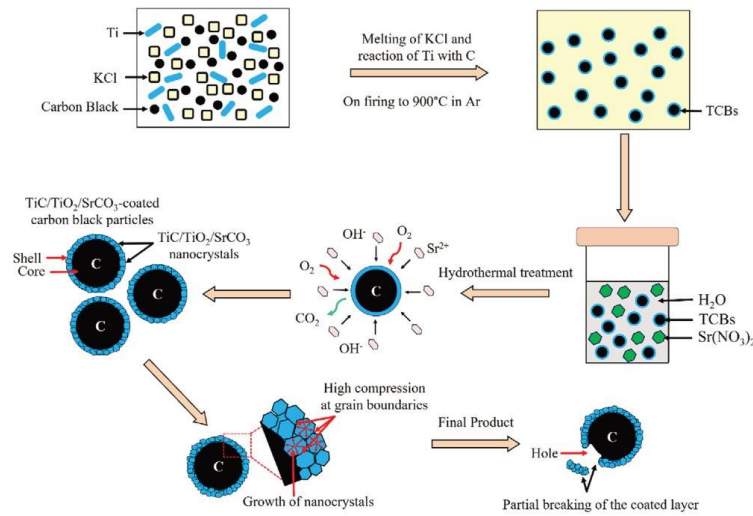
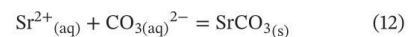
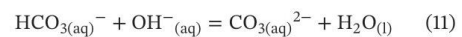
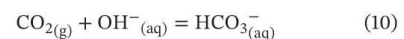
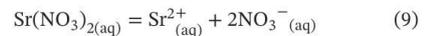
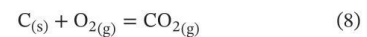
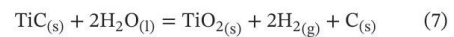
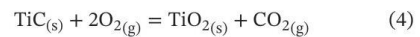
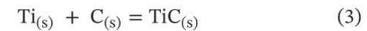


FIGURE 5 Schematic diagram of suggesting formation mechanism of as-synthesized TiC/TiO<sub>2</sub>/SrCO<sub>3</sub>-coated carbon black particles via molten salt synthesis and hydrothermal treatment

### 3.3 | Formation mechanism of the bioactive core-shell particles

The overall fabrication process of TiC/TiO<sub>2</sub>/SrCO<sub>3</sub>-coated CB particles using CBs as both a reactant and template is schematically shown in Figure 5. Reaction mechanisms are suggested based on literatures.<sup>36–39</sup> To fabricate core-shell structure, the MSS of TiC coatings on CBs is a crucial step involved. The formation of dense TiC nanocrystal coatings on CB surfaces concurrently with the undetected Ti phase on the XRD curve (Figure 1B). This pointed out that Ti reacted completely with CB (reaction 1) via a template-growth mechanism,<sup>38</sup> giving rise to a core-shell structure as shown in Figure 2. Once the MSS product (TCBs) was hydrothermally treated at 180–250°C, phase composition and surface characteristics of were modified (Figure 2C–G) due to oxidation and grain growth. However, particle shapes and sizes were unchanged. The TiC shells were oxidized by oxygen and water resulting in the formation of titanium oxides, carbon, and gases (reactions 2–5). Note that the oxidation of TiC is significantly accelerated in the presence of water.<sup>39</sup> Simultaneously, crystals grew with temperature and holding time. Yet, within the limited particle size, the ceramic crystals formed on the carbon surfaces were unable to grow freely. This gave rise to a high compression at the coatings, particularly at the grain boundaries (Figure 5) and, hence, finally the explosion of

the shells, revealing unreacted C cores (Figure 2D). The fresh C core was then further oxidized (reaction 6). SrCO<sub>3</sub> was formed by reaction (10) that resulted from reactions (7)–(9):



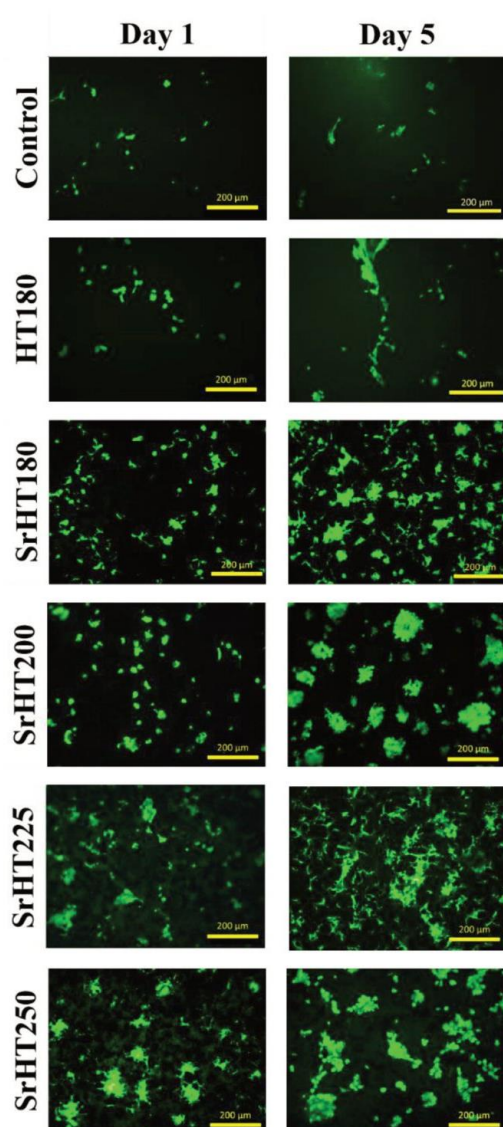


FIGURE 6 Cell viability after days 1 and 5 on the control compared with the TCBs treated at various hydrothermal temperatures. Scale bar = 200  $\mu\text{m}$

### 3.4 | Osteoblast cell viability on the core-shell nanocomposite particles

The cell viability and migration on the samples were observed for the determination of viable cell numbers in cell culture experiment using a fluorescence microscope by FDA staining. Figure 6 shows that osteoblast cell increased

with accumulated time. Clearly, on both days 1 and 5, less cell adhesion was found on the control and the HT180 than the Sr-groups, indicating the role of  $\text{SrCO}_3$  on enhancing cell adhesion and viability. Especially for the SrHT225 and SrHT250, high cell anchorage was observed on both days. The results pointed out that the nanocomposite particles have a favorable surface for cell adhesion and viability. This is in good agreement with previous report<sup>40</sup> that  $\text{SrCO}_3$  had a good number of viable cells and a significant cell attachment that indicated its cytocompatibility and ability to improve bone tissue formation. Here, however, not only  $\text{SrCO}_3$  but also other factors, such as phase composition, nanotopography, and wettability, were suggested to offer an enhancement in the cell adhesion and viability of the SrHT225 and SrHT250 nanocomposites. Lopreiato et al.<sup>41</sup> suggested the role of TiC that it could promote cell maturation and adhesion. Besides, anatase  $\text{TiO}_2$  was claimed as a suitable material for bone cell adhesion because it can absorb more hydroxyl groups on surfaces, which is favorable for bone tissue formation.<sup>42</sup> Our research exhibited that the SrHT225 and SrHT250 had higher hydrophilic surfaces than other groups (Figure 4) which high wettability surface exhibited more cell attachment on it. Chen et al.<sup>43</sup> reported that the nanotopography of particles has an effect on cell adhesion; nanotopography with high roughness and large crystal size promotes cell adhesion and spreading. This correlated to the nanotopography presented in this paper that the roughness and crystal size increased with temperature leading to an enhancement in osteoblast cell adhesion on as-prepared core-shell particles, particularly for the SrHT225 and SrHT250.

### 3.5 | Osteoblast cell proliferation on the core-shell nanocomposite particles

Cell proliferation is a process of a cell to multiply and grow in order to generate a population of cells. Cell proliferation plays a vital role in biological factor that influences the enhancement of osseointegration for bone implant materials.<sup>44</sup> The bioactivity of the samples in each group was tested with PrestoBlue reagent from days 1 to 7, and the results are demonstrated in Figure 7. On day 1, the control, HT180, SrHT180, SrHT200, and SrHT225 groups had less cell proliferation than the SrHT250. On day 3, the SrHT250 had significantly higher cell proliferation than other groups, that is, the control, HT180, SrHT180, SrHT200, and SrHT225. On day 5, the results for the HT180 and SrHT180 groups were similar but significantly lower than the SrHT200, SrHT225, and SrHT250. On day 7, the proliferation of the HT180 group was less than the other groups, except the control. Cell proliferation significantly increased from days 1 to 7 in each group. Interestingly, the

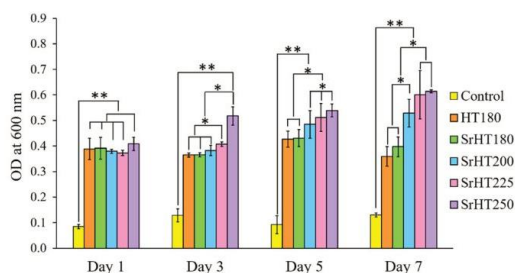


FIGURE 7 Cell proliferation of samples on days 1, 3, 5, and 7 measured with PrestoBlue. Statistical significance was set at “\*”  $p < .05$  and “\*\*\*”  $p < .005$ .

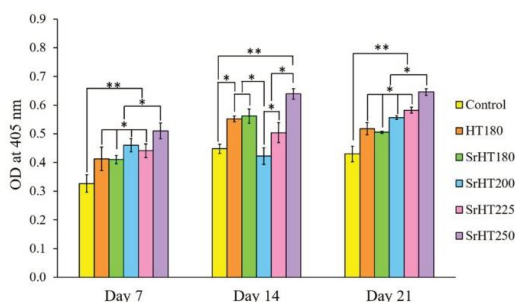


FIGURE 8 Alkaline phosphatase activity of samples on days 7, 14, and 21 (“\*”  $p < .05$ , “\*\*\*”  $p < .005$ )

highest cell proliferation was found on the SrHT250 for all tested days in which the SrHT250 had high roughness, wettability, and high crystallinity of anatase  $\text{TiO}_2$  and  $\text{SrCO}_3$ . Wang et al.<sup>45</sup> indicated that anatase  $\text{TiO}_2$  offered superior cell behaviors, such as cell adhesion, proliferation, and differentiation. Here, our results confirmed that the combined properties of  $\text{TiC}/\text{TiO}_2/\text{SrCO}_3$ -coated CB particles are essential for the improvement of cell adhesion and proliferation.

### 3.6 | Alkaline phosphatase (ALP) activity of osteoblast cell on the core-shell nanocomposites

ALP activity is a well-established marker to measure the early stage of osteogenic differentiation. Figure 8 shows the ALP activity on the control, HT180, SrHT180, SrHT200, SrHT225, and SrHT250. The ALP values for all groups were not much different on day 7. The control and the SrHT200 showed lower ALP values than the other groups on day 14. The trends were clearly increased on day 14, and SrHT250 had the highest ALP value. On day 21, the

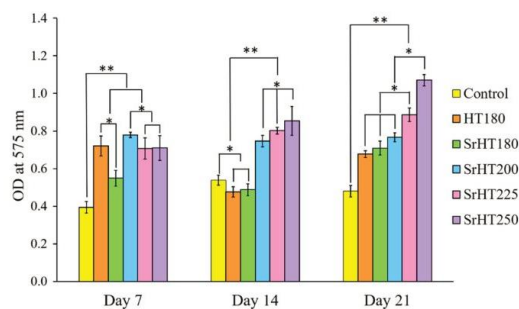


FIGURE 9 Calcium deposition on samples on days 7, 14, and 21 (“\*”  $p < .05$ , “\*\*\*”  $p < .005$ )

SrHT200 and SrHT250 showed insignificant differences in ALP activity. However, for all tested days, the highest ALP activity was obviously found on the SrHT250. Good ALP activity leads to an exceptional osseointegration.<sup>46</sup> This demonstrated that  $\text{TiC}/\text{TiO}_2/\text{SrCO}_3$ -coated carbon black particles, especially for the SrHT250, showed a unique bioactive function to enhance ALP activity. Furthermore, Jiang et al.<sup>47</sup> reported that a substrate with good osteoblast cell adhesion and high proliferation leads to an enhancement in ALP activity that is in accordance with the results shown by the SrHT250.

### 3.7 | Calcium deposition on the core-shell nanocomposite particles

Figure 9 shows calcium deposition on the samples after the measurement at OD of 575 on days 7, 14, and 21. On day 7, the SrHT200 showed higher calcium deposition than other groups. On day 14, the calcium deposition of the SrHT200 was still higher than the other groups, except for the SrHT250. On day 21, among them, the SrHT250 produced the highest calcium deposition and was even higher than day 14. Interestingly, calcium deposition for the Sr-sample groups increased markedly with time, especially for the SrHT250. The results indicated that  $\text{TiC}/\text{TiO}_2/\text{SrCO}_3$ -coated carbon black particles had an important role for promoting calcium deposition. It was reported that Sr-modified bioactive ceramic nanoparticles promoted calcium deposition for the mineralization and differentiation of bone.<sup>48</sup> Note that the presence of  $\text{SrCO}_3$  nanoparticles could remarkably enhance not only cell adhesion, proliferation, and growth rate but also the ALP activity and calcium deposition of osteoblasts cells.

Importantly, the hydrophilicity and nanotopography of the nanocomposite particles are also crucial properties

enhancing their bioactive functions as reported by previous studies.<sup>49,50</sup> Ceramic particles acted as a template for the attachment of calcium secreted from osteoblast cells during bone tissue formation, whereas the hydrophilic particles with rough surfaces acted as preferential substrates for calcium deposition. In the current research, the results demonstrated that the nanocomposite particles, especially the SrHT250, with high hydrophilicity and favored nanotopography, had a greater calcium deposition than those having poorer hydrophilicity and roughness.

#### 4 | CONCLUSION

Surface modification of carbon black particles was achieved by coating with TiC/TiO<sub>2</sub>/SrCO<sub>3</sub> nanocrystals via MSS and hydrothermal process to enhance the wettability and bioactivity of the particles. MSS offered the core-shell structure of TiC-coated carbon black particles providing a great enhancement in the wettability of particles. Hydrothermal synthesis at various temperatures promoted the formation of multi-oxide phases on the shell layers for bioactivity enhancement. It was found that reaction temperature played an important role in the microstructure, crystallite size, surface roughness, and biological functions of the particles. Crystallite size, surface roughness, and wettability of the coated particles increased with temperature giving rise to a favored nanotopography for cell activities of the particles heated at 250°C. Such a unique core-shell structure with a well-reserved nanotopography and the cooperation effect offered by multiphase TiC/TiO<sub>2</sub>/SrCO<sub>3</sub> of the particles treated at 250°C resulted in greatly accelerated bioactivities; cell adhesion, proliferation, osteogenic differentiation, and calcium deposition of osteoblasts cells. These results shed light on developing bioactive particles as a filling material in films and/or scaffolds for guided bone regeneration.

#### ACKNOWLEDGMENTS

This research was supported by the National Science, Research and Innovation Fund (NSRF) and Prince of Songkla University (Grant no. ENG6505057S). Soe HN would like to thank the Graduate School, Prince of Songkla University for the scholarship award. Thanks also to the Center of Excellence in Metal and Materials Engineering (CEMME), the Faculty of Engineering, and the Institute of Biomedical Engineering, Faculty of Medicine, Prince of Songkla University for facilities and equipment support.

#### ORCID

Matthana Khangkhamano  <https://orcid.org/0000-0002-0869-9843>

#### REFERENCES

- Comesaña R, Lusquinos F, Del Val J, Quintero F, Riveiro A, Boutinguiza M, et al. Toward smart implant synthesis: bonding bioceramics of different resorbability to match bone growth rates. *Sci Rep*. 2015;5:1–13. <https://doi.org/10.1038/srep10677>
- Chaturvedi TP. Allergy related to dental implant and its clinical significance. *Clin Cosmet Investig Dent*. 2013;5:57–61. <https://doi.org/10.2147/CCIDE.S35170>
- Hu X, Shen H, Shuai K, Zhang E, Bai Y, Cheng Y, et al. Surface bioactivity modification of titanium by CO<sub>2</sub> plasma treatment and induction of hydroxyapatite: in vitro and in vivo studies. *Appl Surf Sci*. 2011;257(6):1813–23. <https://doi.org/10.1016/j.apsusc.2010.08.082>
- Amini AR, Wallace JS, Nukavarapu SP. Short-term and long-term effects of orthopedic biodegradable implants. *J Long Term Eff Med Implants*. 2011;21(2):93–122. <https://doi.org/10.1615/JLongTermEffMedImplants.v21.i2.10>
- Pei B, Wang W, Dunne N, Li X. Applications of carbon nanotubes in bone tissue regeneration and engineering: Superiority, concerns, current advancements, and prospects. 2019. <https://doi.org/10.3390/nano9101501>
- Hurt RH, Monthieux M, Kane A. Toxicology of carbon nanomaterials: status, trends, and perspectives on the special issue. *Carbon (NY)*. 2006;44(6):1028–33. <https://doi.org/10.1016/j.carbon.2005.12.023>
- Niranjan R, Thakur AK. The toxicological mechanisms of environmental soot (black carbon) and carbon black: focus on oxidative stress and inflammatory pathways. *Front Immunol*. 2017;8:1–20. <https://doi.org/10.3389/fimmu.2017.00763>
- Kim H, Liu X, Kobayashi T, Kohyama T, Wen FQ, Romberger DJ, et al. Ultrafine carbon black particles inhibit human lung fibroblast-mediated collagen gel contraction. *Am J Respir Cell Mol Biol*. 2003;28(1):111–21. <https://doi.org/10.1165/rcmb.4796>
- Granum B, Løvik M. The effect of particles on allergic immune responses. *Toxicol Sci*. 2002;65(1):7–17. <https://doi.org/10.1093/toxsci/65.1.7>
- Vesterdal LK, Folkmann JK, Jacobsen NR, Sheykhzade M, Wallin H, Loft S, et al. Pulmonary exposure to carbon black nanoparticles and vascular effects. *Part Fibre Toxicol*. 2010;7:1–15. <https://doi.org/10.1186/1743-8977-7-33>
- Ganguly K, Etehadieh D, Upadhyay S, Takenaka S, Adler T, Karg E, et al. Early pulmonary response is critical for extra-pulmonary carbon nanoparticle mediated effects: comparison of inhalation versus intra-arterial infusion exposures in mice. *Part Fibre Toxicol*. 2017;14(1):1–17. <https://doi.org/10.1186/s12989-017-0200-x>
- Lambert AL, Mangum JB, DeLorme MP, Everitt JI. Ultrafine carbon black particles enhance respiratory syncytial virus-induced airway reactivity, pulmonary inflammation, and chemokine expression. *Toxicol Sci*. 2003;72(2):339–46. <https://doi.org/10.1093/toxsci/kg032>
- You R, Lu W, Shan M, Berlin JM, Samuel EL, Marcano DC, et al. Nanoparticulate carbon black in cigarette smoke induces DNA cleavage and Th17-mediated emphysema. *Elife*. 2015;4:1–20. <https://doi.org/10.7554/eLife.09623>
- Borm PJA, Robbins D, Haubold S, Kuhlbusch T, Fissan H, Donaldson K, et al. The potential risks of nanomaterials: A review carried out for ECETOC. 2006. <https://doi.org/10.1186/1743-8977-3-11>

15. Lindner K, Ströbele M, Schlick S, Webering S, Jenckel A, Kopf J, et al. Biological effects of carbon black nanoparticles are changed by surface coating with polycyclic aromatic hydrocarbons. *Part Fibre Toxicol.* 2017;14(1):1–17. <https://doi.org/10.1186/s12989-017-0189-1>
16. Shen Y, Wu L, Qin D, Xia Y, Zhou Z, Zhang X, et al. Carbon black suppresses the osteogenesis of mesenchymal stem cells: the role of mitochondria. *Part Fibre Toxicol.* 2018;15(1):1–17. <https://doi.org/10.1186/s12989-018-0253-5>
17. Kim H, Park K, Lee MY. Biocompatible dispersion methods for carbon black. *Toxicol Res.* 2012;28(4):209–216. <https://doi.org/10.5487/TR.2012.28.4.209>
18. Sahu D, Kannan GM, Vijayaraghavan R. Carbon black particle exhibits size dependent toxicity in human monocytes. *Int J Inflam.* 2014;2014:827019. <https://doi.org/10.1155/2014/827019>
19. Scandurra R, D'abusco AS, Longo G. A review of the effect of a nanostructured thin film formed by titanium carbide and titanium oxides clustered around carbon in graphitic form on osseointegration. *Nanomaterials.* 2020;10(6):1–18. <https://doi.org/10.3390/nano10061233>
20. Kumaravel V, Nair KM, Mathew S, Bartlett J, Kennedy JE, Manning BJ, et al. Antimicrobial TiO<sub>2</sub> nanocomposite coatings for surfaces, dental and orthopaedic implants. *Chem Eng J.* 2021;416(February):129071. <https://doi.org/10.1016/j.cej.2021.129071>
21. Chuang YC, Chang CC, Yang F, Simon M, Rafailovich M. TiO<sub>2</sub> nanoparticles synergize with substrate mechanics to improve dental pulp stem cells proliferation and differentiation. *Mater Sci Eng C.* 2021;118:111366. <https://doi.org/10.1016/j.msec.2020.111366>
22. Sajesh KM, Kiran K, Nair SV, Jayakumar R. Sequential layer-by-layer electrospinning of nano SrCO<sub>3</sub>/PRP loaded PHBV fibrous scaffold for bone tissue engineering. *Compos Part B Eng.* 2016;99:445–452. <https://doi.org/10.1016/j.compositesb.2016.06.026>
23. Ye J, Thackray RP, Lee WE, Zhang S. Microstructure and rheological properties of titanium carbide-coated carbon black particles synthesised from molten salt. *J Mater Sci.* 2013;48(18):6269–75. <https://doi.org/10.1007/s10853-013-7424-4>
24. Li X, Dong Z, Westwood A, Brown A, Zhang S, Brydson R, et al. Preparation of a titanium carbide coating on carbon fibre using a molten salt method. *Carbon.* 2008;46(2):305–9. <https://doi.org/10.1016/j.carbon.2007.11.020>
25. Xie W, Mirza Z, Möbus G, Zhang S. Novel synthesis and characterization of high quality silicon carbide coatings on carbon fibers. *J Am Ceram Soc.* 2012;95(6):1878–82. <https://doi.org/10.1111/j.1551-2916.2012.05153.x>
26. Mehnane HF, Wang C, Kondamareddy KK, Yu W, Sun W, Liu H, et al. Hydrothermal synthesis of TiO<sub>2</sub> nanoparticles doped with trace amounts of strontium, and their application as working electrodes for dye sensitized solar cells: tunable electrical properties & enhanced photo-conversion performance. *RSC Adv.* 2017;7(4):2358–64. <https://doi.org/10.1039/c6ra26012h>
27. Ni S, Yang X, Li T. Hydrothermal synthesis and photoluminescence properties of SrCO<sub>3</sub>. *Mater Lett.* 2011;65(4):766–8. <https://doi.org/10.1016/j.matlet.2010.11.056>
28. Lima FM, Martins FM, Junior PHF, Almeida AFL, Freire FNA. Nanostructured titanium dioxide average size from alternative analysis of Scherrer's Equation Tamanho médio das nanopartículas de dióxido de titânio a partir de uma nova abordagem na Equação de Scherrer. *Rev Mater.* 2018;23(1).
29. Gupta MK, Sood PK. Surface roughness measurements in NFMQL assisted turning of titanium alloys: an optimization approach. *Friction.* 2017;5(2):155–70. <https://doi.org/10.1007/s40544-017-0141-2>
30. Gao N, Yan Y. Characterisation of surface wettability based on nanoparticles. *Nanoscale.* 2012;4(7):2202–18. <https://doi.org/10.1039/c2nr11736c>
31. Munshi AM, Singh VN, Kumar M, Singh JP. Effect of nanoparticle size on sessile droplet contact angle. *J Appl Phys.* 2008;103(8):10–5. <https://doi.org/10.1063/1.2912464>
32. Asgari-Fard Z, Sabet M, Salavati-Niasari M. Synthesis and characterization of strontium carbonate nanostructures via simple hydrothermal method. *High Temp Mater Process.* 2016;35(2):215–220. <https://doi.org/10.1515/htmp-2014-0232>
33. Kim J, Kang S. Stable phase domains of the TiO<sub>2</sub>-Ti<sub>3</sub>O<sub>5</sub>-Ti<sub>2</sub>O<sub>3</sub>-TiO-Ti(C<sub>x</sub>O<sub>y</sub>)-TiC system examined experimentally and via first principles calculations. *J Mater Chem A.* 2014;2(8):2641–7. <https://doi.org/10.1039/c3ta14633b>
34. Lee DS, Lee SY, Rhee KY, Park SJ. Effect of hydrothermal temperature on photocatalytic properties of TiO<sub>2</sub> nanotubes. *Curr Appl Phys.* 2014;14(3):415–20. <https://doi.org/10.1016/j.cap.2013.12.018>
35. He J, Zhou W, Zhou X, Zhong X, Zhang X, Wan P, et al. The anatase phase of nanotopography titania plays an important role on osteoblast cell morphology and proliferation. *J Mater Sci Mater Med.* 2008;19(11):3465–72. <https://doi.org/10.1007/s10856-008-3505-3>
36. Zhang S, Khangkhamano M, Zhang H, Yeprem HA. Novel synthesis of ZrB<sub>2</sub> powder via molten-salt-mediated magnesiothermic reduction. *J Am Ceram Soc.* 2014;97(6):1686–8. <https://doi.org/10.1111/jace.12945>
37. Soe HN, Khangkhamano M, Sangkert S, Meesane J, Kokoo R. TiC-coated carbon particles as bioactive substrates for inducing of mineralization in bone healing. *Mater Lett.* 2018;229:118–21. <https://doi.org/10.1016/j.matlet.2018.06.125>
38. Khangkhamano M. Novel molten salt synthesis of ZrB<sub>2</sub> and ZrC powders and molten salt synthesis of novel TiC. University of Exeter. 2014.
39. Yang G, Park SJ. Conventional and microwave hydrothermal synthesis and application of functional materials: a review. *Materials (Basel).* 2019;12(7):1177. <https://doi.org/10.3390/ma12071177>
40. Demirel M, Kaya A, Aksakal B. Synthesizing the strontium carbonate and silver doped bioceramic bone graft: structure-properties and cell viability. *Int J Appl Ceram Technol.* 2020;17(1):333–41. <https://doi.org/10.1111/ijac.13316>
41. Lopreiato M, Mariano A, Cocchiola R, Longo G, Dalla Vedova P, Scandurra R, et al. Nanostructured tic layer is highly suitable surface for adhesion, proliferation and spreading of cells. *Condens Matter.* 2020;5(2):1–12. <https://doi.org/10.3390/condmat5020029>
42. Lv L, Li K, Xie Y, Cao Y, Zheng X. Enhanced osteogenic activity of anatase TiO<sub>2</sub> film: surface hydroxyl groups induce conformational changes in fibronectin. *Mater Sci Eng C.* 2017;78:96–104. <https://doi.org/10.1016/j.msec.2017.04.056>
43. Chen W, Villa-diaz LG, Sun Y, Weng S, Kim JK, Lam RH, et al. Nanotopography in fluences adhesion, spreading, and

- self-renewal of human embryonic stem cells. *ACS Nano*. 2012;6(5):4094–103.
44. Xu Z, Lu H, Lu J, Lv C, Zhao X, Wang G. Enhanced osteogenic activity of Ti alloy implants by modulating strontium configuration in their surface oxide layers. *RSC Adv*. 2018;8(6):3051–60. <https://doi.org/10.1039/c7ra10807a>
  45. Wang Y, Zhang D, Wen C, Li Y. Processing and characterization of SrTiO<sub>3</sub>-TiO<sub>2</sub> nanoparticle-nanotube heterostructures on titanium for biomedical applications. *ACS Appl Mater Interfaces*. 2015;7(29):16018–26. <https://doi.org/10.1021/acsami.5b04304>
  46. Albesri S, Alblaiheh A, Niazy AA, Ramalingam S, Sundar C, Alghamdi HS. Biomarkers as independent predictors of bone regeneration around biomaterials: a systematic review of literature. *J Contemp Dent Pract*. 2018;19(5):605–18. <https://doi.org/10.5005/jp-journals-10024-2306>
  47. Jiang H, Zhou W, Wang B, Tang L. The effect of strontium modified rough titanium surface on biologic response of MC3T3-E1 cells. *Dent Mater J*. 2020;39(5):808–14. <https://doi.org/10.4012/dmj.2019-188>
  48. Querido W, Farina M, Anselme K. Strontium ranelate improves the interaction of osteoblastic cells with titanium substrates: increase in cell proliferation, differentiation and matrix mineralization. *Biomater*. 2015;5:e1027847. <https://doi.org/10.1080/21592535.2015.1027847>
  49. Ward BC, Webster TJ. The effect of nanotopography on calcium and phosphorus deposition on metallic materials in vitro. *Biomaterials*. 2006;27(16):3064–74. <https://doi.org/10.1016/j.biomaterials.2005.12.027>
  50. Zhang Q, Xiao L, Xiao Y. Porous nanomaterials targeting autophagy in bone regeneration. *Pharmaceutics*. 2021;13(10):1–22. <https://doi.org/10.3390/pharmaceutics13101572>

**How to cite this article:** Soe HN, Meesane J, Kokoo R, Khangkhamano M. Bioactive core-shell structure of TiC/TiO<sub>2</sub>/SrCO<sub>3</sub> coating on carbon black particles for bone tissue formation: Fabrication, characterization, and biological functions. *J Am Ceram Soc*. 2023;106:2689–2701. <https://doi.org/10.1111/jace.18942>

APPENDIX II



# A material-based core–shell bioactive compound of mixed oxide phases with TiC on carbon black particles for bone augmentation in oral and maxillofacial surgery

Hnin Nandar Soe<sup>1</sup>, Matthana Khangkhamano<sup>2</sup>, Jirut Meesane<sup>3,a)</sup>, Rungrote Kokoo<sup>4</sup>

<sup>1</sup>Department of Mining and Materials Engineering, Faculty of Engineering, Prince of Songkla University, Hat Yai, Songkhla 90110, Thailand

<sup>2</sup>Center of Excellence in Metal and Materials Engineering (CEMME), Prince of Songkla University, Hat Yai, Songkhla 90110, Thailand

<sup>3</sup>Institute of Biomedical Engineering, Faculty of Medicine, Prince of Songkla University, Hat Yai, Songkhla 90110, Thailand

<sup>4</sup>Department of Chemical Engineering, Faculty of Engineering, King Mongkut's University of Technology North Bangkok, Bangkok 10800, Thailand

<sup>a)</sup>Address all correspondence to this author. e-mail: jirutmeesane999@yahoo.co.uk

Received: 9 February 2023; accepted: 1 June 2023; published online: 20 June 2023

Augmentation of a bone defect with bone graft materials for oral and maxillofacial surgery is a challenge for researchers. Bone substitutes (autograft, allograft, xenograft) have several drawbacks such as risk of infection, limitation of harvest sites and amount of graft material, risk of donor site morbidity, and pain. Over the last decade, various kinds of synthetic materials have been used in order to improve bone augmentation without any risk of disease transmission and overcome an additional operation. However, the bioactivity of these synthetic materials is still challenging due to inadequate bone cell response for augmentation. Here, we synthesized core–shell with a porous structure of mixed oxide phases with titanium carbide on carbon black particles to treat bone loss for oral and maxillofacial surgery. Core–shell bioactive compounds were fabricated via molten salt synthesis followed by thermal treatment in air at different temperatures. The phase composition and morphology of the product powders were characterized by XRD, FE-SEM, and TEM. The particles were cultured with osteoblast cells to evaluate the biological functions. The results demonstrated that TCBS250 with a high proportion of titanium oxides had the highest surface roughness, porosity, hydrophilicity, and biological response. Finally, TCBS250 is a promising bioactive material for augmentation or regeneration of bone in oral and maxillofacial surgery.

## Introduction

The maxillofacial problem has been a major issue in these days. Millions of people globally are suffering from insufficient bone volume due to extended time after tooth loss before implant replacement, injuries from accidents, trauma, cysts, caries, tumor resection, and various diseases at the oral and maxillofacial areas [1, 2]. In critical cases, any patients who suffered from maxillofacial problems usually have to take surgery in order to regain their original maxillofacial shape. Thus, the different types of bone augmentation materials used for bone injuries include autografts, allografts, xenografts, and synthetic materials [3]. Autografts (taking bone from another area of the same patient) are considered to be the most effective for bone defect treatment. Autografts can establish direct bone bonding and exhibit osteoinductive and osteoconductive properties. However, an autotransplantation has drawbacks such as nerve injury,

long operative time, infection, blood loss, risk of bacterial infection, donor site morbidity, and postoperative pain [4]. Although allografts (bones obtained from a bone bank or another person) can reduce surgical time compared with autografts, allografts have disadvantages such as disease transmission, infection, and graft rejection [5]. On the other hand, xenografts (harvested from different species) are considered to be biocompatible with the bone of recipients and have osteoinductive potential; however, the drawbacks include immune response, high cost, and the risk of disease transmission [6].

Currently, synthetic biomaterials have been used to restore the maxillofacial injuries including metals, polymers, and ceramics [7]. In particular, bioactive ceramic materials, such as hydroxyapatite (HA), beta-tricalcium phosphate ( $\beta$ -TCP), and bioactive glasses, are used to fill bone defects for augmentation [8, 9].  $\beta$ -TCP has been accepted as a bone filler material for bone

formation and replacement [10], but other studies reported  $\beta$ -TCP could not stimulate adequate bone growth [11, 12]. HA is more biocompatible and stable in bone tissue than  $\beta$ -TCP [13]; but it has limitations in remodeling capacity, and therefore, inappropriate as a bone-grafting material for bone augmentation [14]. Some studies [15, 16] reported that bioactive glasses have superior osteoconductive properties for bone regeneration, but little or no resorption of a bioglass was observed, which is a limitation in bone augmentation as a defect filler [17]. Therefore, the reconstruction and augmentation of a bone defect at the oral and maxillofacial area are a major challenge for biomaterials researchers, and orthopedic and maxillofacial surgeons.

In recent decades, carbon black particles (CBs) have been popular due to their lightweight and large specific surface area. Furthermore, CBs are biocompatible and inexpensive [18]. However, its poor surface wettability and dispersion in water lead to insufficient functionality for chemical bonding with human tissues. In order to overcome these problems, surface modification of CBs has been purposed in this study. The CBs were used as a reactant and template. TiC coatings not only promoted wettability but also facilitated strong bonding with human bone [19, 20]. Furthermore, titanium oxides provide corrosion resistance, biocompatibility, and non-toxic [21–23]. The presence of TiC and titanium oxides on CBs could improve physical and biological properties. Therefore, our research focused on fabrication of mixed oxide phases with TiC on CBs via molten salt synthesis followed by thermal treatment in air. To the best of our knowledge, no research has reported on the fabrication of core-shell with a porous structure of mixed oxide phases with TiC on CBs as a bioactive compound for oral and maxillofacial surgery. In this work, the phase composition, structure, and morphology of the fabricated particles were characterized and observed. Moreover, the formation mechanism of the designated particles was explored. Then, the physical properties and biological functionality were also investigated. Finally, core-shell with a porous structure of bioactive compound were evaluated on bone augmentation for oral maxillofacial surgery.

## Results

### Phase composition and structural study

Figure 1 shows the XRD pattern of the starting CBs, TiC-coated CBs (TCBs) prepared by molten salt synthesis (MSS) at 900 °C for 4 h, 1:8 ratio of Ti:CBs, and compared with the samples obtained after thermal treatment in air at 100 °C, 150 °C, 200 °C, 250 °C for 20 min. Only C phase was observed [Fig. 1(a)] at  $2\theta = 25.18^\circ$  and  $43.5^\circ$  attributed to amorphous nature of the starting CB particles (ICDD card 00-041-1487). In Fig. 1(b), all the peaks with the diffraction intensity were located at  $2\theta = 35.9^\circ$ ,  $41.9^\circ$ ,  $60.5^\circ$ ,  $72.4^\circ$ , and  $76.1^\circ$  which corresponded to

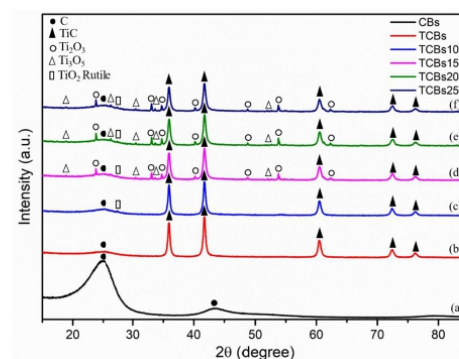


**Figure 1:** XRD results of the samples; (a) CBs, (b) TCBs, (c) TCBs100, (d) TCBs150, (e) TCBs200, (f) TCBs250.

(111), (200), (220), (311), and (222) reflection of TiC, respectively. One broad peak of carbon was observed at  $2\theta = 25.18^\circ$ , which indicated the amorphous nature of the carbon black used. No residual Ti or other intermediate phases were found, which pointed out the complete reaction of TiC via MSS and the composition of the TCBs made of only TiC and C. In Fig. 1(c), after oxidation at 100 °C (TCBs100), an extra tiny peak of rutile  $\text{TiO}_2$  was observed at  $2\theta = 27.4^\circ$  (110) along with the TiC and C peaks. When the temperature was increased to 150–200 °C (TCBs150, TCBs200), two more oxide phases,  $\text{Ti}_2\text{O}_3$  and  $\text{Ti}_3\text{O}_5$ , were noticed in addition to the TiC, C, and rutile [Fig. 1(d, e)]. The observation of titanium oxide phases was attributed to the oxidation of TiC during thermal treatment in air. Upon increasing the temperature to 250 °C (TCBs250), obviously, the peak intensities of TiC became lower, whereas those of the oxide peaks increased due to an increased oxidation rate at 250 °C [Fig. 1(f)]. Besides, the crystallinities of the samples increased with an increase in thermal treatment. The crystalline size of the samples was evaluated using the Scherrer Eq. (1) [24],

$$D = \frac{k\lambda}{(\beta\cos\theta)}, \quad (1)$$

where  $D$ ,  $k$ ,  $\lambda$ ,  $\beta$ , and  $\theta$  represent average crystallite size (nm), Scherrer constant, X-ray wavelength, full width at half maximum of diffraction angle, and Bragg angle, respectively. The calculated crystalline sizes of TCBs, TCBs100, TCBs150, TCBs200, and TCBs250 were 19.31, 20.36, 25.42, 32.96, and 35.21 nm, respectively. Clearly, thermal treatment affected the crystalline size and the formation of the mixed phase particles.

Figure 2 demonstrates FE-SEM images of the starting CBs and as-prepared samples. The FE-SEM images show the morphologies and surface appearances of the CBs [Fig. 2(a)], TCBs before oxidation [Fig. 2(b)] and compares those results with the

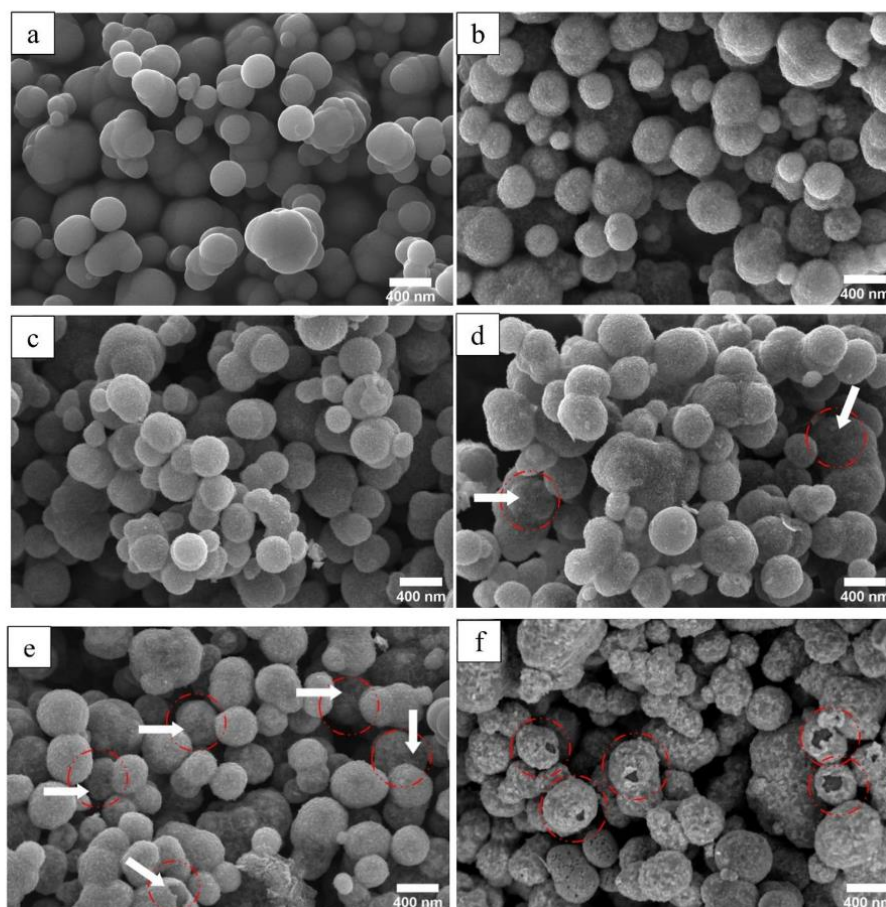


**Figure 2:** FE-SEM images of the samples; (a) CBs, (b) TCBs, (c) TCBs100, (d) TCBs150, (e) TCBs200, (f) TCBs250.

oxidized samples in Fig. 2(c–f). CBs demonstrates the spherical shapes with the smooth surface. The TCBs show spherical structures with an average particle size of 400 nm and rough surfaces. This occurred because the surface consisted of TiC nanocrystals. After oxidation at 100–250 °C, although all the particle samples retained their spherical shapes and 400 nm in size, surface features were modified. The formation of porosity (denoted by circles and arrows) can be observed beginning with the oxidation temperature of 150 °C (TCBs150) and became obvious at 200 °C and 250 °C on the TCBs200 and TCBs250, respectively. In particular, the TCBs250 showed more voids of approximately 80–130 nm in diameter, and some broken coatings were found as pointed out by the arrows. This was possibly due to the crystal growth and increased oxidation rate of TiC

at 250 °C. The formation of such porous structures revealed the fresh C core that confirmed the core–shell structure of the particles, which can be attributed to different diffusion rates of materials at the core (C) and shell (TiC) at the oxidation temperature. The roughness of the samples was evaluated by the arithmetic average roughness ( $R_a$ ) Eq. (2) [25],

$$R_a = \frac{1}{n_x n_y} \sum_{i=1}^{n_x} \sum_{j=1}^{n_y} [Z(i,j) - Z_{ave}], \quad (2)$$

where  $R_a$  is the arithmetic average roughness,  $i$  and  $j$  are pixels in the  $x$  and  $y$  directions, respectively,  $n_x$  and  $n_y$  represent the maximum number of pixels in two directions,  $Z(i,j)$  is the topography data for the surface, and  $Z_{ave}$  denotes the height of

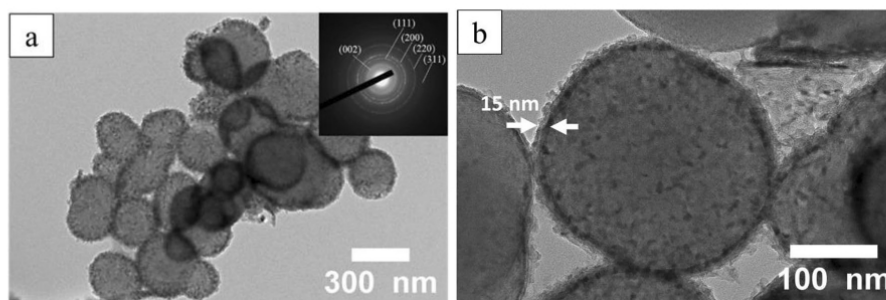


**Figure 3:** TEM images of TCBs250: (a) is an SAED pattern of particles; (b) illustrates the shell thickness of 15 nm.

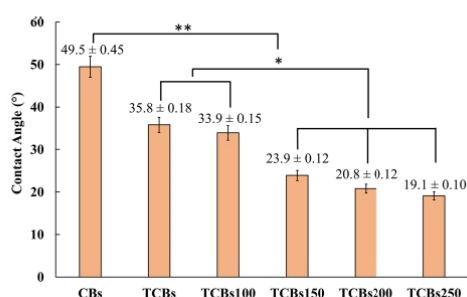


**Figure 4:** Contact angle measurements of samples after testing with water droplets.

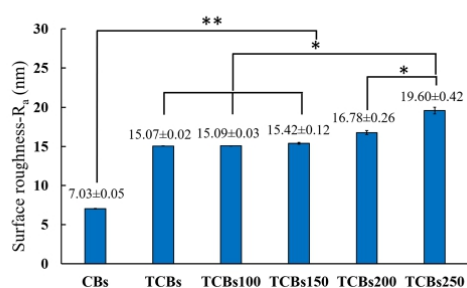


**Figure 5:** Surface roughness of the samples.  $R_a$  is the arithmetical mean of roughness.

the average surface. The estimated surface roughness of the particles is reported in Fig. 5. Obviously, compared to the uncoated CBs, a significant increase in surface roughness was gained from the coatings. Core-shell structure of the TCBs250 was further studied by TEM (Fig. 3). The shell thickness was around 15 nm. The SAED pattern revealed the diffraction rings of the (111),

(200), (220), and (311) planes of the cubic TiC and the (002) plane of C.

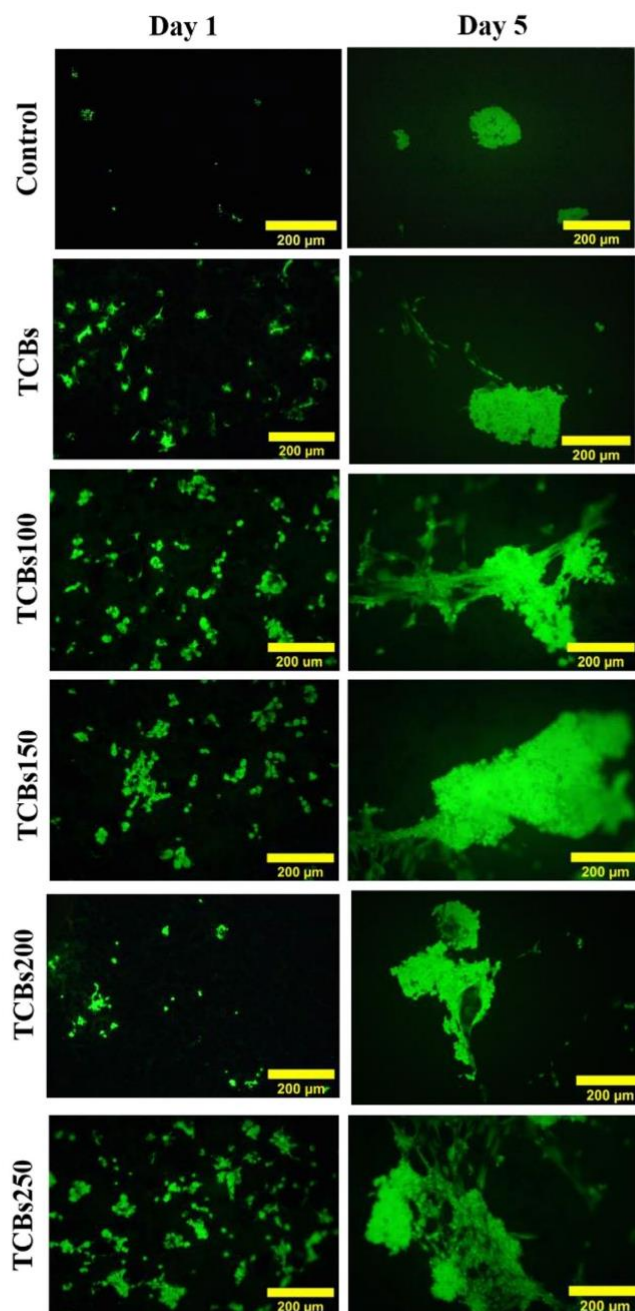
### Wettability measurement

Surface wettability plays an important role for determining the biological response of biomaterials and has a great influence on the behavior of the cells during the bone formation process. Figure 4 shows the contact angle measurements for the uncoated CBs, TCBs, TCBs100, TCBs150, TCBs200, and TCBs250. CBs were used as the control. As expected, a significant decrease in the contact angle was observed in the coated CBs compared with the uncoated particles. The CBs exhibited a value of  $49.5 \pm 0.45^\circ$  while the TCBs gave a value of  $35.8 \pm 0.18^\circ$ . When the TCBs were treated in air from  $100^\circ\text{C}$  to  $250^\circ\text{C}$ , their contact angles were  $33.9 \pm 0.15^\circ$ ,  $23.9 \pm 0.12^\circ$ ,  $20.8 \pm 0.12^\circ$ , and  $19.1 \pm 0.10^\circ$  for the TCBs100, TCBs150, TCBs200, and TCBs250, respectively. All the TCBs groups compared with the CBs showed a dramatic decrease in the contact angle value from  $49.5 \pm 0.45^\circ$  to  $19.1 \pm 0.10^\circ$ . Meanwhile, the estimated surface roughness values of the CBs, TCBs, TCBs100, TCBs150, TCBs200, and TCBs250 were  $7.03 \pm 0.05$ ,  $15.07 \pm 0.02$ ,  $15.09 \pm 0.03$ ,  $15.42 \pm 0.12$ ,  $16.78 \pm 0.26$ , and  $19.60 \pm 0.42$ , respectively. All TCBs groups resulted in higher surface roughness values compared with the CBs. The results indicated that the surface roughness values increased as the thermal treatment temperatures increased (Fig. 5). This might be due to the increased porosity of the particles, which is in good agreement with the FE-SEM observations (Fig. 2). Notably, the TCBs250 had a lower contact angle than the others that can be attributed to the increased porosity and roughness of the sample, which can promote hydrophilicity.

### Cell viability

Cell viability and migration on the samples were observed to determine viable cell numbers in the cell culture experiment using FDA staining and fluorescence microscopy [26]. Figure 6

**Figure 6:** Cell viability after FDA staining on days 1 and 5. Green indicates live cell attachment.



shows cell viability of the samples after 1 and 5 days. The prepared samples had greater cell attachment than the control. In the control group, the cells were more circular in shape than the cells in the other groups. On day 1, the osteoblast cells in all groups were observed to have a combination of circular and elongation shapes except the control. It can be seen that the amount of cell attachment increased on day 5. A small number of cells could loosely adhere to the control on each day. Larger numbers of cells were attached to the TCBS200, and TCBS250 on day 5. The best cell adhesion was found on TCBS250.

### Cell proliferation

Cell proliferation was evaluated on days 1, 3, 5, and 7 with PrestoBlue. Figure 7(a) shows that the control, TCBS, TCBS100, and TCBS150 had less cell proliferation than the other two samples. The TCBS200 showed lower cell proliferation than the other groups but higher than the control on day 1. After day 1, cell proliferation on the TCBS200 increased from day 3 to day 5 and increased up to day 7. Overall, cell proliferation increased from day 1 to 7, and proliferation for the TCBS250 was significantly higher than the other groups except for TCBS200 on days 5 and 7. The cell proliferation results were the same for the TCBS200 and TCBS250 on days 5 and 7.

### ALP activity

Figure 7(b) shows the ALP activity of the samples. The ALP activity of the TCBS100 had a similar value as the TCBS150 and a higher value than the control and TCBS on day 7. On day 14, the control group was lower than the other groups. The ALP activity of TCBS200 was similar to control on day 7 but significantly higher than control on day 21. The ALP activity of cells has enhanced in the modified samples compared with the control. This is due to the increased adhesion and proliferation of the MG-63 cells on the TCBS200. The highest ALP values were found on the TCBS250 on days 7 and 21. The results showed that ALP activity increased as time increased.

### Protein synthesis

Figure 7(c) shows the protein synthesis of the samples after measurements at OD 559 nm on days 7, 14, and 21 using the BCA kit. The results suggested that the values for all groups were not much different from day 7 to day 21 except for the TCBS250 group. The control and TCBS showed lower protein synthesis values than the other groups on day 7. The TCBS250 exhibited a significantly higher protein synthesis value on day 14. The protein synthesis values of the TCBS100, TCBS150, and TCBS200 were higher than the control and TCBS on days 14 and

21. The highest amounts of protein synthesis were found on the TCBS250 on days 14 and 21.

### Calcium deposition

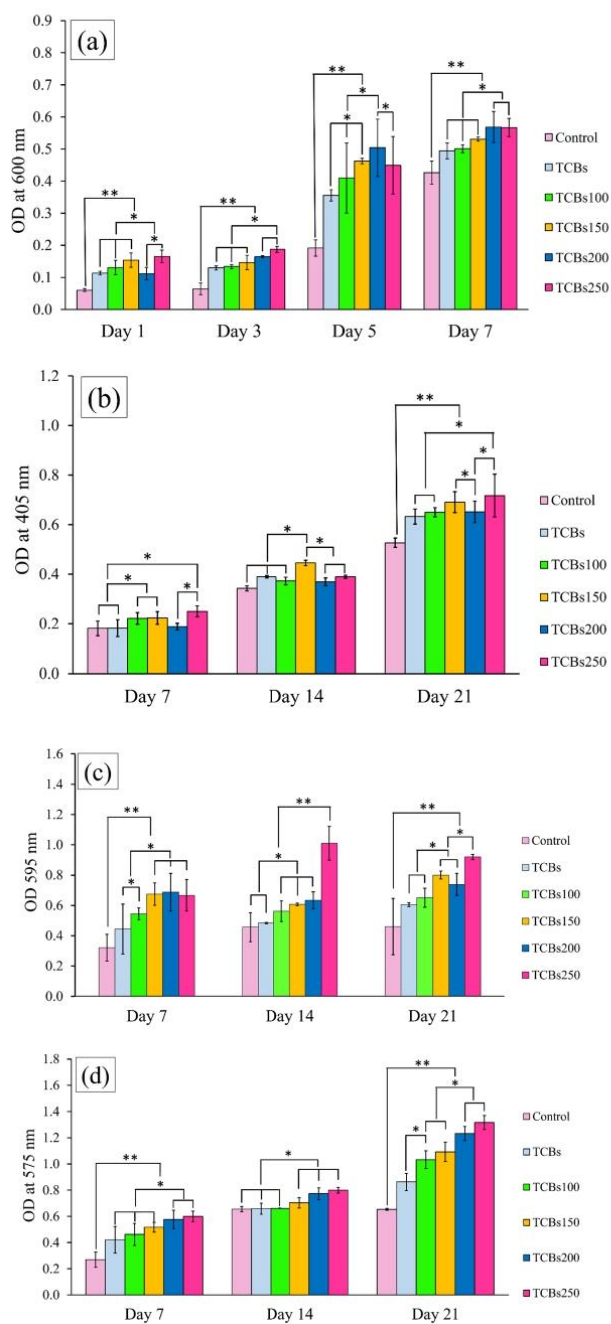
Figure 7(d) shows the calcium deposition on the samples after the OD measurements at 575 nm on days 7, 14, and 21. It was observed that the TCBS200 and TCBS250 samples had higher calcium deposition compared to the other groups on day 7. Similar calcium deposition was found on the control, TCBS, and TCBS100 on day 14. It was also revealed that calcium deposition on the TCBS150, TCBS200, and TCBS250 had higher values than the control, TCBS, and TCBS100. On day 21, calcium deposition on the control was significantly lower than the other groups. Increased calcium deposition was found on the modified samples due to the presence of Ti-based bioactive compounds TiC, TiO<sub>2</sub>, Ti<sub>2</sub>O<sub>3</sub>, and Ti<sub>3</sub>O<sub>5</sub> on the particle surface. Based on published results, the prepared samples have bio-acceptable properties [27][28].

## Discussion

### Formation mechanism of mixed oxide phases with TiC on CBs

The overall formation mechanism of mixed oxide phases with TiC on CBs is illustrated in Fig. 8. The formation mechanism was proposed in previous publications [29, 30]. The core-shell structure was formed via MSS. On heating, the KCl melts at 770 °C, which provides a liquid reaction medium that increases the surface contact areas of the solid particles and increases the diffusion rates of the dissolved species in the molten salt. In this melt, the Ti dissolves [29] and diffuses onto the surface of the CBs through the molten salt and subsequently reacts to form in situ TiC coatings on the surfaces of the CBs [30]. The coating process is dominated via a template growth mechanism. When the TCBS are heated in air, the phase compositions and surface features change. The core-shell with a porous structure were observed clearly after thermal treatment in air at 250 °C. Formation of the porous mixed oxide phases with TiC on the CBs can be suggested as follows. At first, the TiC shells oxidize to form oxides of titanium and CO<sub>2</sub>. The CO<sub>2</sub> diffuses faster than O<sub>2</sub> due to its higher diffusion coefficient in air [31]. This causes a strong surface diffusion along the core-shell interface. Next, small voids form at the interface due to diffusivity differences of the matter [32]. At the high temperature of 250 °C, the internal pressure increases that leads to partial breaking of the shell, which forms holes or gaps along the shell layer [Fig. 2(f)]. Finally, the core-shell with porous particles form via thermal treatment in air.

**Figure 7:** (a) Cell proliferation of the samples measured with Presto-Blue® on days 1, 3, 5, and 7, (b) ALP activity, (c) protein synthesis, and (d) calcium deposition of samples on days 7, 14, and 21.



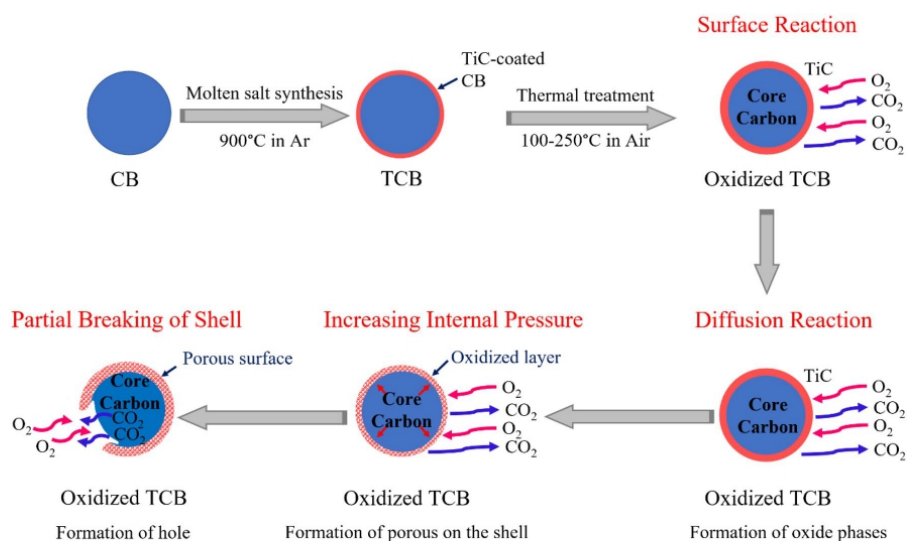


Figure 8: Illustration of a possible formation mechanism of the synthesized mixed oxide phases with TiC on CBs.

#### Chemical components of mixed oxide phases with TiC on CBs and bone formation

The chemical components of biomaterial particles are clues related to the potential promotion of bone formation in living organisms [33]. The compositions which have charges and hydrophilicity normally show the ability to promote attachment from biological signals from body fluids [34]. These biological signals act as bridges that connect the cells and the biomaterial particles, which lead to enhanced cell behaviors and the promotion of bone formation. Furthermore, cells in direct contact with biomaterial particles with a charge and hydrophilicity will promote bone formation [35]. Our results demonstrated that the presence of a high amount of titanium oxides on the particles exhibited greater hydrophilicity and cell response than lower amounts, which provides an environment to enhance bone formation.

#### Morphology and topography of mixed oxide phases with TiC on CBs and bone formation

The morphology of particulate biomaterials has often been used to describe the performance of bone formation [36]. First, many morphologies are possible; for instance, sphere, triangle, needle, and plate show different potentials to promote bone formation [37], which is the result of different surface areas that can affect cell response [38]. Porous spherical

particles exhibit more surface area than other morphologies and the cause of cell adhesion. Furthermore, a porous structure supports the flow of the nutrients and bioactive molecules during cell growth for bone formation [39].

Second, the topography of particulate biomaterials is also a clue for the enhancement potential of bone formation [40]. Previous studies demonstrated that a rough surface has more potential to promote bone growth than a smooth surface [41]. A rough surface has many nodes which support cell attachment, creeping, spreading, and migration [42], which also leads to enhanced bone formation. Some previous research exhibited crystal grains on the surface of materials that affected surface roughness leading to the promotion of bone formation [43]. Large crystal grains can lead to a rougher surface that can affect bone formation more than small crystal grains.

Interestingly, few reports discuss the morphology of particulate biomaterials with core-shell forms that may affect bone formation. In our research, we focused on the morphology of core-shell porous spherical particles of particulate biomaterials for bone formation. Principally, the core-shell spherical particles with a rough surface have a unique surface energy of the substrate for improvement in bioactivity [44]. The surface energy correlates with the process of biological performance; therefore, core-shell particles with a rough surface can support attachment of biological molecules acting as signals to promote new tissue formation.

### Physical properties of mixed oxide phases with TiC on CBs and bone formation

The physical properties of particulate biomaterials are another clue which affects bone formation [45]. Siqueira et al. [46] mentioned the importance of hydrophilicity, which causes the promotion of bone formation. Hydrophilic particles demonstrated good performance to enhance bone formation [47] because a hydrophilic surface supports adhesion of cells that have mainly negative charges on their surface [48]. This leads to enhanced cell spreading, migration, and proliferation that promote bone formation.

In general, the water contact angle measurement is used to test for hydrophilicity. Materials that have a water contact angle less than  $90^\circ$  are known as hydrophilic [49]. Hydrophilicity of a material is mainly associated with surface roughness, which can affect initial cell adhesion on a material's surface [50]. All samples exhibited hydrophilic behavior except for the CBs, which suggested that the changes in the contact angle value were due to the hydrophilicity properties of the particles and the increased surface roughness caused by surface modification of the particles. Furthermore, particles with different proportions of phases have different surface wettabilities and physicochemical properties that can profoundly affect cell adhesion and attachment [51]. Some studies reported that cells tend to spread on hydrophilic surfaces rather than hydrophobic surfaces [52, 53] which are consistent with our experiment.

### Osteoblast response of mixed oxide phases with TiC on CBs and bone formation

Osteoblast response is an important clue to explain the performance of particulate biomaterials for bone formation [54]. Osteoblast response is often described in both qualitative and quantitative terms [55]. Cell viability is used to explain cell organization on particulate biomaterials. Cell viability is the initial cell behavior related to other responses including creeping, spreading, migration, and proliferation [56]. Structure, size, and form are the main factors of particulate biomaterials related to their ability to support bone formation [57]. Previous studies reported that a suitable size of particulate biomaterials is in the range of 100 to 300 microns for optimized bone formation [58]. Porous particles have a suitable surface area that contributes to cell adhesion [59]. Finally, hydrophilicity is the important clue to enhance cell adhesion and biological or signal molecules on particulate biomaterials [60].

We have presented a correlation of those factors to cell response. First, cell viability was demonstrated by the osteoblast cells that self-organized into a dense structure as time increased. This indicated an interaction between the osteoblasts and ceramic compound that could improve biocompatibility. This

is in good agreement with other studies that showed that good cell viability depended on the surface structure and surface composition of the biomaterials [61]. A high cell proliferation rate indicates a high level of tissue formation, which is in accordance with previous research [62]. In addition, cell proliferation plays a critical role in biological factors that influence the enhancement of bioperformance of particulate biomaterials for bone tissue applications [63].

Besides cell response, the other bioactivities that include ALP activity, protein absorption, and calcium deposition are important clues to explain the performance of particulate biomaterials to promote bone formation. Similar to the explanation regarding cell response, the structures and characteristics of particulate biomaterials affect bioactivity. A suitable bioactive surface area of the oxide particles, particularly in  $Ti_2O_3$ , affects the potential to induce ALP activity. The high surface area of the  $Ti_2O_3$  particles acts as the clue to activate more ALP activity than a low surface area [64]. Some studies reported that the surface of titanium oxides exhibits bioactivity to induce ALP activity [65–67]. Increased protein adhesion is related to the increased wettability of the sample and shows the importance of hydrophilicity for bone formation. Wettability affects cell adhesion, proliferation, and protein adsorption. Moreover, according to Elisa et al. [68], protein adhesion on a bioactive material surface depends on the surface properties. In this current research, increased calcium deposition was found on TCBS250 due to the presence of mixed phases on the particle surface. Based on previously published reports [69, 70], we note the bio-acceptability of spherical particles with a porous structure.

### Performance of mixed oxide phases with TiC on CBs and clinical application

According to the literature, core-shell particles with large surface areas are able to promote cell responses leading to enhanced bone formation [71]. Particulate biomaterials in the size range of microns with hydrophilicity and surface roughness are the main clues to promote cell responses [72]. Mixed oxide phases with TiC on CBs, which have good cell response for bone formation, have been selected as bone-grafting materials for filling a defect area. These particles play the important roles of maintaining the space of the defect and promoting bone formation. They are often used for bone augmentation in oral and maxillofacial surgery [73]. Some research focused on the development of the components and surface roughness of those particles to enhance biological performance to promote bone formation [74, 75].

The expected procedure of filling bone defects with bone-grafting materials is shown in Fig. 9. In some cases, a failing tooth in a patient needs to be extracted. The bone surrounding the extracted socket of the tooth is no longer stimulated by the tooth root and begins to collapse or shrink. Dental surgeons

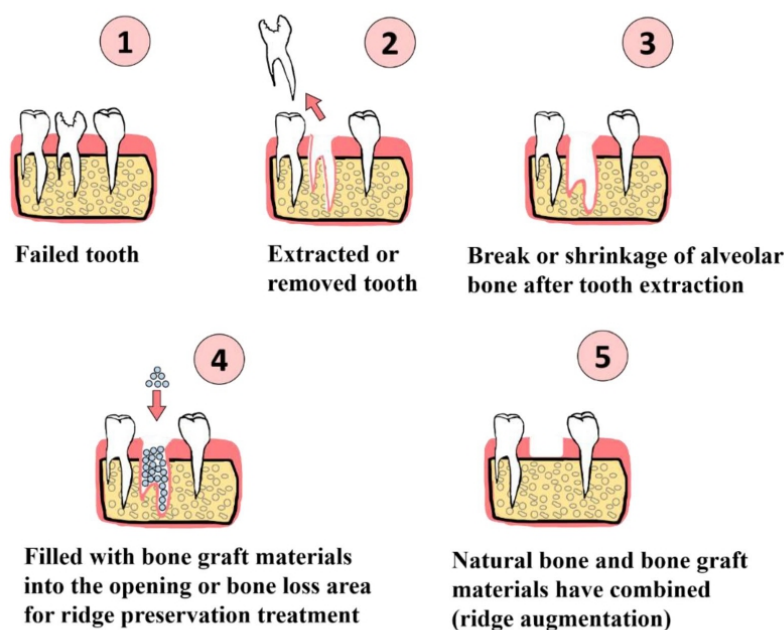


Figure 9: Reconstruction of bone loss using grafting materials.

need to insert bone-grafting materials into the open area for bone augmentation. This aims to heal or reconstruct the bone loss area. Once the bone-grafting materials and natural bone have completely matured, a suitable membrane may be used for ridge preservation treatment. Further dental implantation or tooth replacement can then be considered.

Notably, very few studies have reported on core-shell with porosity and the potential to fill a bone loss defect. Our research demonstrated that modified particles with high surface roughness have the potential to support cell response leading to enhanced bone augmentation. These modified particles can be applied in bone defects or loss preservation at the oral and maxillofacial area. Furthermore, the formed core-shell with porous particles have a suitable structure to support biological functions for cell responses in bone formation. Therefore, our product has promising properties for bone augmentation in oral and maxillofacial surgery.

### Conclusions

Core-shell bioactive compounds consisting of mixed oxide phases with TiC on CBs were fabricated for the purpose of bone augmentation in oral and maxillofacial surgery. The particles were synthesized via MSS followed by thermal treatment at different temperatures. The prepared particles possessed a

core-shell with porous structure and a well-reserved morphology led to enhance the hydrophilicity, surface roughness, and bioactivity of the particles. The sample treated at higher oxidation temperature showed greater surface roughness, porosity, and crystallite size than the other samples. Furthermore, the porous particles support attachment of biological molecules acting as signals to promote new bone tissue formation. Especially, TCBS250 showed better biological performance than others. In summary, TCBS250 showed the highest cell response and bioactivity as a promising material for bone formation at oral and maxillofacial surgery.

### Methodology

#### Raw materials

Titanium powder (Ti) ( $\geq 150 \mu\text{m}$ , purity 99.7%, Sigma-Aldrich) and CBs N990 (99% pure, Sigma-Aldrich) with an average particle size of 400 nm were used as the starting raw materials while the salt used to form the reaction media was potassium chloride (KCl) (99.9% pure, Ajax Finechem).

#### Sample preparation

Ti powders were mixed with CBs, in a molar ratio of 1:8, and further combined with KCl in an agate mortar. The mixture was

then put in an alumina crucible covered with a lid and loaded in an alumina tube furnace and fired at 900 °C for 4 h in an argon-protected atmosphere with heating and cooling rates of 3 °C/min. Once the furnace cooled down, the solidified mass was repeatedly washed with distilled water, to remove residual salt, and then oven-dried overnight. The samples gained from this process were designated as TCBs. The TCBs were thermally treated in air for 20 min at 100, 150, 200, and 250 °C to obtain the porous particles of mixed phases. The samples heated at 100, 150, 200, and 250 °C were labeled as TCBs100, TCBs150, TCBs200, and TCBs250, respectively.

### Sample characterization

Phase identification and purity of the reacted powder were examined by X-ray diffraction (XRD) (X'Pert MPD, Philips, the Netherlands). The spectra were recorded at 30 mA and 40 kV, using Ni-filtered CuK $\alpha$  radiation. The scan rate ( $2\theta$ ) was 3°/min with a step size of 0.05. ICDD cards used for identification were TiC (03-065-8804), C (00-041-1487), Ti<sub>2</sub>O<sub>3</sub> (01-071-6412), TiO<sub>2</sub>-Rutile (01-079-6031), and Ti<sub>3</sub>O<sub>5</sub> (01-083-7068).

Morphologies, topography, and core-shell structure were observed by a field-emission scanning electron microscope (FE-SEM) (Apreo, FEI, Czech Republic) and a transmission electron microscope (TEM) (JEOL JEM-2010). Selected area electron diffraction (SAED) was used to assist in identifying the local phases.

The wettability of the samples was measured using an optical contact angle meter (OCA-15EC CA meter). Optical contact angle is an analysis system used to measure the interfacial parameters and phenomena of a sample. In this contact angle measurement, drops that hang from a dosing needle of the optical analysis were placed on a solid surface for the analytical process. A drop of 2  $\mu$ l of distilled water was deposited on the sample surface where its contact angle was then measured under ambient conditions. The angle values of at least 3 drops were recorded and averaged for each sample.

### Biological testing

#### Materials and methods

The samples were divided into six groups according to the experimental conditions that included the control, TCBs, TCBs100, TCBs150, TCBs200, and TCBs250. An agarose hydrogel solution without particles was used as the control. The other groups were prepared by mixing 500 mg of particles and 1% agarose hydrogel solution. The prepared solutions were then transferred into a plastic mold and dried for 24 h. The dried specimens were measured and cut with a razor blade into approximately 10  $\times$  10 mm pieces for cell culture. The samples were washed twice with 75%

ethanol for sterilization of the samples and rinsed in phosphate-buffered saline (PBS) three times for removal of residual ethanol. Each sample was put in 24-well culture plate for the biological property tests.

#### Cell culture

The MG-63 osteoblast cell which is isolated from human osteosarcoma cell line was cultured in complete alpha-MEM medium ( $\alpha$ -MEM, Gibco™, Invitrogen, Carlsbad, CA, USA) that included 10% fetal bovine serum, 1% penicillin/streptomycin, and 0.1% fungizone and seeded on the prepared particle construct in agarose gel in different ratios. The MG-63 osteoblast cells were maintained in a 5% CO<sub>2</sub>/95% air-humidified incubator at 37 °C. At the differentiation stage, the MG-63 osteoblast cells were cultured in an osteogenic supplement (OS) medium (OS; 20 mM  $\beta$ -glycerophosphate, 50  $\mu$ M ascorbic acid, and 100 nM dexamethasone; Sigma-Aldrich).

#### Cell viability

The cells in each group were stained with fluorescein diacetate (FDA) on days 1 and 5 to observe cell viability. The media were removed from the sample constructs in agarose and washed with PBS two times. Fresh media were added to the samples and 5  $\mu$ g/ml of acetone was added in fresh media and kept at room temperature for 5 min. The samples were rinsed with PBS and observed under fluorescence microscopy.

#### Cell proliferation

The MG-63 cell line was also used to observe cell proliferation. Cells were seeded on the substrate. Cell proliferation was detected at days 1, 3, 5, and 7 with 10% PrestoBlue® cell viability reagent. The cell viability reagent in fresh media was added onto the substrates and incubated for 1 h before measurement at 600 nm.

#### Alkaline phosphatase activity (ALP)

The osteoblast cells on the samples were cultured in the OS media condition on days 7, 14, and 21, in accordance with the cell lysis method for ALP detection. The cells on the substrate were frozen at -80 °C for 1 h and then placed in 1% Triton X-100 in PBS at room temperature for 1 h for 3 cycles upon which the samples were then crushed and inserted into an Eppendorf tube. The supernatant was separated from the pellet at 12,000 RPM centrifugation. The supernatant was used for ALP detection following the manufacturer's instructions (Abcam®, Cambridge, UK).

#### Protein synthesis

The cells were cultured in OS media on days 7, 14, and 21 to measure the protein. The prepared specimens constructed in

agarose were rinsed with PBS after removal from the media. An amount of 800  $\mu$ L of 1% Triton X-100 was then added in each group and frozen at  $-80^{\circ}\text{C}$  for 1 h and at room temperature for 1 h for 3 cycles. The samples were crushed and put into Eppendorf tubes. A centrifuge was used to separate the supernatant from the pellet. A cell lysis solution was used for the protein measurement following the manufacturer's instructions (Pierce™ BCA Protein Assay Kit, Thermo Scientific, USA).

#### Calcium deposition

The MG-63 osteoblast cells were cultured in an osteogenic supplement (OS) medium at days 7, 14, and 21. A lysis solution was used for the calcium assay (Calcium Colorimetric Assay Kit, MAK022, Sigma-Aldrich, USA) following the manufacturer's instructions.

#### Statistical analysis

Five samples were used for each test that included contact angle, surface roughness, cell viability, cell proliferation, ALP activity, protein synthesis, and calcium deposition. All the experiments were repeated three times. All data were shown as mean  $\pm$  standard deviation. The results were statistically compared by one-way analysis of variance (ANOVA) and Tukey's honestly significant difference test (SPSS 16.0 software package). Statistical significance was set at  $p < 0.05$  and  $p < 0.005$ .

#### Acknowledgments

This work was under a partial research project (REC.61-066-25-2). This research was also supported by the National Science, Research and Innovation Fund (NSRF) and Prince of Songkla University (Grant No. ENG6505057S). The authors would like to thank the Faculty of Engineering, Faculty of Medicine and the Graduate School, and the Center of Excellence in Metal and Materials Engineering (CEMME) at Prince of Songkla University for the support of this research.

#### Funding

This work was under a partial research project (REC.61-066-25-2). This research was also supported by the National Science, Research and Innovation Fund (NSRF) and Prince of Songkla University (Grant No. ENG6505057S).

#### Data availability

The data that support the findings of this study are available on request from the corresponding author.

#### Code availability

Not Applicable.

#### Declarations

**Conflict of interest** The authors declare that they have no conflict of interest.

#### Ethical approval

Not Applicable.

#### Consent to participate

Not Applicable.

#### Consent for publication

Not Applicable.

#### References

1. S. Petti, U. Glendor, L. Andersson, World traumatic dental injury prevalence and incidence, a meta-analysis-one billion living people have had traumatic dental injuries. *Dent. Traumatol.* **34**(2), 71–86 (2018). <https://doi.org/10.1111/edt.12389>
2. Z. Sheikh, C. Sima, M. Glogauer, Bone replacement materials and techniques used for achieving vertical alveolar bone augmentation. *Materials (Basel)* **8**(6), 2953–2993 (2015). <https://doi.org/10.3390/ma8062953>
3. M. Esposito, M.G. Grusovin, S. Kwan, H.V. Worthington, P. Coulthard, Interventions for replacing missing teeth: bone augmentation techniques for dental implant treatment, in *Cochrane database of systematic reviews*. ed. by M. Esposito (John Wiley, Chichester, 2008)
4. V.V. Dam, H.A. Trinh, D. Rokaya, D.H. Trinh, Bone augmentation for implant placement: recent advances. *Int. J. Dent.* **2022**, 1–7 (2022). <https://doi.org/10.1155/2022/8900940>
5. R. Zhao, R. Yang, P.R. Cooper, Z. Khurshid, A. Shavandi, J. Ratnayake, Bone grafts and substitutes in dentistry: a review of current trends and developments. *Molecules* **26**(10), 3007 (2021). <https://doi.org/10.3390/molecules26103007>
6. P.H. de Azambuja Carvalho, N. de Oliveira Ciaramicolo, O. Ferreira Júnior, V.A. Pereira-Filho, Clinical and laboratorial outcomes of xenogeneic biomaterials: literature review. *Front. Oral Maxillofac. Med.* **5**, 8–8 (2023). <https://doi.org/10.21037/fomm-21-43>
7. B. Liu, D. Lun, Current application of  $\beta$ -tricalcium phosphate composites in orthopaedics. *Orthop. Surg.* **4**(3), 139–144 (2012). <https://doi.org/10.1111/j.1757-7861.2012.00189.x>
8. J. Girón et al., Biomaterials for bone regeneration: an orthopedic and dentistry overview. *Brazilian J. Med. Biol. Res.* **54**(9), 1–15 (2021). <https://doi.org/10.1590/1414-431x2021e11055>
9. H. Siddiqui, K. Pickering, M. Mucalo, A review on the use of hydroxyapatite-carbonaceous structure composites in bone

- replacement materials for strengthening purposes. *Materials (Basel)* **11**(10), 1813 (2018). <https://doi.org/10.3390/ma11101813>
10. R.A. Horowitz, Z.I.V. Mazor, C. Foitzik, H. Prasad, M. Rohrer, A.D.Y. Palti,  $\beta$ -tricalcium phosphate as bone substitute material: properties and clinical applications. *J. Osseointegration* **1**(1), 60–68 (2010)
  11. R. AL Jasser, S. Andreana, An overview of bone augmentation techniques. *Clin. Case Rep. Rev.* **2**(4), 393–398 (2016). <https://doi.org/10.15761/CCRR.1000226>
  12. T. Starch-Jensen, D. Deluiz, N.H. Bruun, E.M.B. Tinoco, Maxillary sinus floor augmentation with autogenous bone graft alone compared with alternate grafting materials: a systematic review and meta-analysis focusing on histomorphometric outcome. *J. Oral Maxillofac. Res.* (2020). <https://doi.org/10.5037/jomr.2020.11302>
  13. R. Fujita, A. Yokoyama, T. Kawasaki, T. Kohgo, Bone augmentation osteogenesis using hydroxyapatite and  $\beta$ -tricalcium phosphate blocks. *J. Oral Maxillofac. Surg.* **61**(9), 1045–1053 (2003). [https://doi.org/10.1016/S0278-2391\(03\)00317-3](https://doi.org/10.1016/S0278-2391(03)00317-3)
  14. V. Petrovic, P. Zivkovic, D. Petrovic, V. Stefanovic, Craniofacial bone tissue engineering. *Oral Surg. Oral Med. Oral Pathol. Oral Radiol.* **114**(3), e1–e9 (2012). <https://doi.org/10.1016/j.oooo.2012.02.030>
  15. M. Cannio, D. Bellucci, J.A. Roether, D.N. Boccaccini, V. Cannillo, Bioactive glass applications: a literature review of human clinical trials. *Materials (Basel)* **14**(18), 5440 (2021). <https://doi.org/10.3390/ma14185440>
  16. J.R. Jones, Reprint of: Review of bioactive glass: from Hench to hybrids. *Acta Biomater.* **23**, S53–S82 (2015). <https://doi.org/10.1016/j.actbio.2015.07.019>
  17. J.M. Gunn, J. Rekola, J. Hirvonen, A.J. Aho, Comparison of the osteoconductive properties of three particulate bone fillers in a rabbit model: allograft, calcium carbonate (Biocoral®) and S53P4 bioactive glass. *Acta Odontol. Scand.* **71**(5), 1238–1242 (2013). <https://doi.org/10.3109/00016357.2012.757642>
  18. T.A. Silva, F.C. Moraes, B.C. Janegitz, O. Fatibello-Filho, Electrochemical biosensors based on nanostructured carbon black: a review. *J. Nanomater.* **2017**, 1–14 (2017). <https://doi.org/10.1155/2017/4571614>
  19. R. Scandurra, A. Scotto d'Abusco, G. Longo, A review of the effect of a nanostructured thin film formed by titanium carbide and titanium oxides clustered around carbon in graphitic form on osseointegration. *Nanomaterials* **10**(6), 1233 (2020). <https://doi.org/10.3390/nano10061233>
  20. G. Longo et al., Effect of titanium carbide coating by ion plating plasma-assisted deposition on osteoblast response: a chemical, morphological and gene expression investigation. *Surf. Coatings Technol.* **204**(16–17), 2605–2612 (2010). <https://doi.org/10.1016/j.surfcoat.2010.02.007>
  21. V. Kumaravel et al., Antimicrobial TiO<sub>2</sub> nanocomposite coatings for surfaces, dental and orthopaedic implants. *Chem. Eng. J.* **416**, 129071 (2021). <https://doi.org/10.1016/j.cej.2021.129071>
  22. Y.-C. Chuang, C.-C. Chang, F. Yang, M. Simon, M. Rafailovich, TiO<sub>2</sub> nanoparticles synergize with substrate mechanics to improve dental pulp stem cells proliferation and differentiation. *Mater. Sci. Eng. C* **118**, 111366 (2021). <https://doi.org/10.1016/j.msec.2020.111366>
  23. J.C.M. Souza et al., Nano-scale modification of titanium implant surfaces to enhance osseointegration. *Acta Biomater.* **94**, 112–131 (2019). <https://doi.org/10.1016/j.actbio.2019.05.045>
  24. F.M. Lima, F.M. Martins, P.H.F. Maia Júnior, A.F.L. Almeida, F.N.A. Freire, Nanostructured titanium dioxide average size from alternative analysis of Scherrer's equation. *Matéria (Rio Janeiro)* (2018). <https://doi.org/10.1590/s1517-707620170001.0301>
  25. M.K. Gupta, P.K. Sood, Surface roughness measurements in NFMQL assisted turning of titanium alloys: an optimization approach. *Friction* **5**(2), 155–170 (2017). <https://doi.org/10.1007/s40544-017-0141-2>
  26. F. Piccinini, A. Tesei, C. Arienti, A. Bevilacqua, Cell counting and viability assessment of 2D and 3D cell cultures: expected reliability of the trypan blue assay. *Biol. Proced. Online* **19**(1), 8 (2017). <https://doi.org/10.1186/s12575-017-0056-3>
  27. H.N. Soe, M. Khangkhamano, S. Sangkert, J. Meesane, R. Kokoo, TiC-coated carbon particles as bioactive substrates for inducing of mineralization in bone healing. *Mater. Lett.* **229**, 118–121 (2018). <https://doi.org/10.1016/j.matlet.2018.06.125>
  28. S. Zhang, M. Khangkhamano, H. Zhang, H.A. Yeprem, Novel synthesis of ZrB<sub>2</sub> powder via molten-salt-mediated magnesium-thermic reduction. *J. Am. Ceram. Soc.* **97**(6), 1686–1688 (2014). <https://doi.org/10.1111/jace.12945>
  29. X. Li et al., Preparation of a titanium carbide coating on carbon fibre using a molten salt method. *Carbon N. Y.* **46**(2), 305–309 (2008). <https://doi.org/10.1016/j.carbon.2007.11.020>
  30. J. Ye, R.P. Thackray, W.E. Lee, S. Zhang, Microstructure and rheological properties of titanium carbide-coated carbon black particles synthesised from molten salt. *J. Mater. Sci.* **48**(18), 6269–6275 (2013). <https://doi.org/10.1007/s10853-013-7424-4>
  31. Y. Yin, R.M. Rioux, C.K. Erdonmez, S. Hughes, G.A. Somorjai, A.P. Alivisatos, Formation of hollow nanocrystals through the nanoscale Kirkendall effect. *Science* **304**(5671), 711–714 (2004). <https://doi.org/10.1126/science.1096566>
  32. S. Chen, H. Wang, L. Zhu, J. Li, J. Sun, Solvothermal synthesis of TiO<sub>2</sub> hollow nanospheres utilizing the Kirkendall effect and their photocatalytic activities. *Appl. Surf. Sci.* **321**, 86–93 (2014). <https://doi.org/10.1016/j.apsusc.2014.09.197>
  33. X. Yu, X. Tang, S.V. Gohil, C.T. Laurencin, Biomaterials for bone regenerative engineering. *Adv. Healthc. Mater.* **4**(9), 1268–1285 (2015). <https://doi.org/10.1002/adhm.201400760>

34. K.L. Menzies, L. Jones, The impact of contact angle on the biocompatibility of biomaterials. *Optom. Vis. Sci.* **87**(6), 387–399 (2010). <https://doi.org/10.1097/OPX.0b013e3181da863e>
35. K. Anselme, Osteoblast adhesion on biomaterials. *Biomaterials* **21**(7), 667–681 (2000). [https://doi.org/10.1016/s0142-9612\(99\)00242-2](https://doi.org/10.1016/s0142-9612(99)00242-2)
36. J.G. Lyons, M.A. Plantz, W.K. Hsu, E.L. Hsu, S. Minardi, Nano-structured biomaterials for bone regeneration. *Front. Bioeng. Biotechnol.* **8**(August), 1–28 (2020). <https://doi.org/10.3389/fbioe.2020.00922>
37. C. Wu, J. Chang, Y. Xiao, *Advanced bioactive inorganic materials for bone regeneration and drug delivery*. CRC Press (2013). <https://doi.org/10.1201/b13926>
38. U. Meyer, A. Büchter, H. Wiesmann, U. Joos, D. Jones, Basic reactions of osteoblasts on structured material surfaces. *Eur. Cells Mater.* **8**, 39–49 (2005). <https://doi.org/10.22203/eCM.v009a06>
39. Q. Zhang, L. Xiao, Y. Xiao, Porous nanomaterials targeting autophagy in bone regeneration. *Pharmaceutics* **13**(10), 1572 (2021). <https://doi.org/10.3390/pharmaceutics13101572>
40. A. Barfeie, J. Wilson, J. Rees, Implant surface characteristics and their effect on osseointegration. *Br. Dent. J.* **218**(5), E9–E9 (2015). <https://doi.org/10.1038/sj.bdj.2015.171>
41. Y. Zhang, S.E. Chen, J. Shao, J.J.P. van den Beucken, Combinatorial surface roughness effects on osteoclastogenesis and osteogenesis. *ACS Appl. Mater. Interfaces* **10**(43), 36652–36663 (2018). <https://doi.org/10.1021/acsami.8b10992>
42. S. Migita, K. Araki, Effect of nanometer scale surface roughness of titanium for osteoblast function. *AIMS Bioeng.* **4**(1), 162–170 (2017). <https://doi.org/10.3934/bioeng.2017.1.162>
43. M. Bencina, A. Igljč, M. Mozetič, I. Junkar, Crystallized TiO<sub>2</sub> nanosurfaces in biomedical applications. *Nanomaterials* **10**(6), 1121 (2020). <https://doi.org/10.3390/nano10061121>
44. L. Fialho, L. Grenho, M.H. Fernandes, S. Carvalho, Porous tantalum oxide with osteoconductive elements and antibacterial core-shell nanoparticles: a new generation of materials for dental implants. *Mater. Sci. Eng. C* **120**, 111761 (2021). <https://doi.org/10.1016/j.msec.2020.111761>
45. C.I. Codrea et al., Advances in osteoporotic bone tissue engineering. *J. Clin. Med.* **10**(2), 253 (2021). <https://doi.org/10.3390/jcm10020253>
46. R. Siqueira et al., Hydrophilic titanium surface modulates early stages of osseointegration in osteoporosis. *J. Periodontol. Res.* **56**(2), 351–362 (2021). <https://doi.org/10.1111/jre.12827>
47. B.D. Boyan, E.M. Lotz, Z. Schwartz, Roughness and hydrophilicity as osteogenic biomimetic surface properties. *Tissue Eng. Part A* **23**(23–24), 1479–1489 (2017). <https://doi.org/10.1089/ten.tea.2017.0048>
48. S. Cai, C. Wu, W. Yang, W. Liang, H. Yu, L. Liu, Recent advance in surface modification for regulating cell adhesion and behaviors. *Nanotechnol. Rev.* **9**(1), 971–989 (2020). <https://doi.org/10.1515/ntrev-2020-0076>
49. G. Lamour et al., Contact angle measurements using a simplified experimental setup. *J. Chem. Educ.* **87**(12), 1403–1407 (2010). <https://doi.org/10.1021/ed100468u>
50. G. Strnad, N. Chirila, C. Petrovan, O. Russu, Contact angle measurement on medical implant titanium based biomaterials. *Procedia Technol.* **22**, 946–953 (2016). <https://doi.org/10.1016/j.procty.2016.01.094>
51. K. Cai, A. Rechtenbach, J. Hao, J. Bossert, K.D. Jandt, Polysaccharide-protein surface modification of titanium via a layer-by-layer technique: characterization and cell behaviour aspects. *Biomaterials* **26**(30), 5960–5971 (2005). <https://doi.org/10.1016/j.biomaterials.2005.03.020>
52. A. Sengottuvelan, P. Balasubramanian, J. Will, A.R. Boccaccini, Bioactivation of titanium dioxide scaffolds by ALP-functionalization. *Bioact. Mater.* **2**(2), 108–115 (2017). <https://doi.org/10.1016/j.bioactmat.2017.02.004>
53. J. Wei et al., Adhesion of mouse fibroblasts on hexamethyldisiloxane surfaces with wide range of wettability. *J. Biomed. Mater. Res. Part B Appl. Biomater.* **81**(1), 66–75 (2007). <https://doi.org/10.1002/jbm.b.30638>
54. G. Borciani, G. Montalbano, N. Baldini, G. Cerqueni, C. Vitale-Brovarone, G. Ciapetti, Co-culture systems of osteoblasts and osteoclasts: simulating in vitro bone remodeling in regenerative approaches. *Acta Biomater.* **108**, 22–45 (2020). <https://doi.org/10.1016/j.actbio.2020.03.043>
55. K. Anselme et al., Qualitative and quantitative study of human osteoblast adhesion on materials with various surface roughnesses. *J. Biomed. Mater. Res.* **49**(2), 155–166 (2000). [https://doi.org/10.1002/\(SICI\)1097-4636\(200002\)49:2%3c155::AID-JBM2%3e3.0.CO;2-J](https://doi.org/10.1002/(SICI)1097-4636(200002)49:2%3c155::AID-JBM2%3e3.0.CO;2-J)
56. A.E. Miller, P. Hu, T.H. Barker, Feeling things out: Bidirectional signaling of the Cell–ECM interface, Implications in the mechanobiology of cell spreading, migration, proliferation, and differentiation. *Adv. Healthc. Mater.* **9**(8), 1901445 (2020). <https://doi.org/10.1002/adhm.201901445>
57. P. Kazimierzak, A. Przekora, Osteoconductive and osteoinductive surface modifications of biomaterials for bone regeneration: a concise review. *Coatings* **10**(10), 971 (2020). <https://doi.org/10.3390/coatings10100971>
58. C.A. Shapoff, G.M. Bowers, B. Levy, J.T. Mellonig, R.A. Yukna, The effect of particle size on the osteogenic activity of composite grafts of allogeneic freeze-dried bone and autogenous marrow. *J. Periodontol.* **51**(11), 625–630 (1980). <https://doi.org/10.1902/jop.1980.51.11.625>
59. K.M. Hotchkiss, G.B. Reddy, S.L. Hyzy, Z. Schwartz, B.D. Boyan, R. Olivares-Navarrete, Titanium surface characteristics, including topography and wettability, alter macrophage activation. *Acta Biomater.* **31**, 425–434 (2016). <https://doi.org/10.1016/j.actbio.2015.12.003>

60. H. Wang, S.C.G. Leeuwenburgh, Y. Li, J.A. Jansen, The use of micro- and nanospheres as functional components for bone tissue regeneration. *Tissue Eng. Part B Rev.* **18**(1), 24–39 (2012). <https://doi.org/10.1089/ten.teb.2011.0184>
61. C.C. Wachesk et al., Cell viability and adhesion on diamond-like carbon films containing titanium dioxide nanoparticles. *Appl. Surf. Sci.* **266**, 176–181 (2013). <https://doi.org/10.1016/j.apsusc.2012.11.124>
62. R. Florencio-Silva, G.R.D.S. Sasso, E. Sasso-Cerri, M.J. Simões, P.S. Cerri, Biology of bone tissue: Structure, function, and factors that influence bone cells. *Biomed. Res. Int.* **2015**, 1–17 (2015). <https://doi.org/10.1155/2015/421746>
63. M. Ansari, Bone tissue regeneration: biology, strategies and interface studies. *Prog. Biomater.* **8**(4), 223–237 (2019). <https://doi.org/10.1007/s40204-019-00125-z>
64. K. Oya et al., Differences in the bone differentiation properties of MC3T3-E1 cells on polished bulk and sputter-deposited titanium specimens. *J. Biomed. Mater. Res. Part A.* (2010). <https://doi.org/10.1002/jbm.a.32751>
65. P. Santiago-Medina, P.A. Sundaram, N. Diffoot-Carlo, Titanium oxide: a bioactive factor in osteoblast differentiation. *Int. J. Dent.* **2015**, 1–9 (2015). <https://doi.org/10.1155/2015/357653>
66. L. Zhang, L. Chen, A review on biomedical titanium alloys: recent progress and prospect. *Adv. Eng. Mater.* **21**(4), 1801215 (2019). <https://doi.org/10.1002/adem.201801215>
67. B. Feng, J. Weng, B.C. Yang, S.X. Qu, X.D. Zhang, Characterization of surface oxide films on titanium and adhesion of osteoblast. *Biomaterials* **24**(25), 4663–4670 (2003). [https://doi.org/10.1016/S0142-9612\(03\)00366-1](https://doi.org/10.1016/S0142-9612(03)00366-1)
68. C.N. Elias, J.H.C. Lima, R. Valiev, M.A. Meyers, Biomedical applications of titanium and its alloys. *JOM* **60**(3), 46–49 (2008). <https://doi.org/10.1007/s11837-008-0031-1>
69. L. Mullen, R.C. Stamp, W.K. Brooks, E. Jones, C.J. Sutcliffe, Selective laser melting: a regular unit cell approach for the manufacture of porous, titanium, bone in-growth constructs, suitable for orthopedic applications. *J. Biomed. Mater. Res. Part B Appl. Biomater.* **89**(2), 325–334 (2009). <https://doi.org/10.1002/jbm.b.31219>
70. L. Zhao, L. Liu, Z. Wu, Y. Zhang, P.K. Chu, Effects of micropitted/nanotubular titania topographies on bone mesenchymal stem cell osteogenic differentiation. *Biomaterials* **33**(9), 2629–2641 (2012). <https://doi.org/10.1016/j.biomaterials.2011.12.024>
71. K. Deshmukh, T. Kovářik, T. Křenek, D. Docheva, T. Stich, J. Pola, Recent advances and future perspectives of sol–gel derived porous bioactive glasses: a review. *RSC Adv.* **10**(56), 33782–33835 (2020). <https://doi.org/10.1039/D0RA04287K>
72. K. Yun, M. Vang, H. Yang, Wettability and drug delivery of functionally graded nano-micro porous titanium surface. *J. Korean Acad. Prosthodont.* **43**(3), 307–319 (2008)
73. S. Cavalu et al., Nanoparticles and nanostructured surface fabrication for innovative cranial and maxillofacial surgery. *Materials (Basel)* **13**(23), 5391 (2020). <https://doi.org/10.3390/ma13235391>
74. A.B. Novaes Jr., S.L.S. de Souza, R.R.M. de Barros, K.K.Y. Pereira, G. Iezzi, A. Piattelli, Influence of implant surfaces on osseointegration. *Braz. Dent. J.* **21**(6), 471–481 (2010). <https://doi.org/10.1590/S0103-64402010000600001>
75. W. Zhou et al., The effect of surface roughness and wettability of nanostructured TiO<sub>2</sub> film on TCA-8113 epithelial-like cells. *Surf. Coatings Technol.* **200**(20–21), 6155–6160 (2006). <https://doi.org/10.1016/j.surfcoat.2005.09.029>

**Publisher's Note** Springer Nature remains neutral with regard to jurisdictional claims in published maps and institutional affiliations.

Springer Nature or its licensor (e.g. a society or other partner) holds exclusive rights to this article under a publishing agreement with the author(s) or other rightsholder(s); author self-archiving of the accepted manuscript version of this article is solely governed by the terms of such publishing agreement and applicable law.

APPENDIX III

1. Experimental procedure for core-shell TiC-coated CBs via molten salt synthesis method

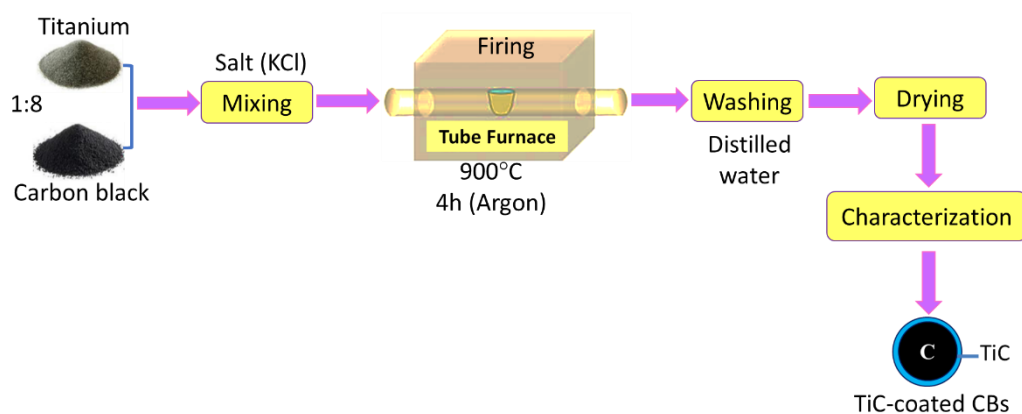


**Figure 14.** Schematic diagram of sample preparation procedure via molten salt synthesis method.

2. Experimental procedure for the fabrication of TiC/TiO<sub>2</sub>/SrCO<sub>3</sub>-coated CBs by hydrothermal method

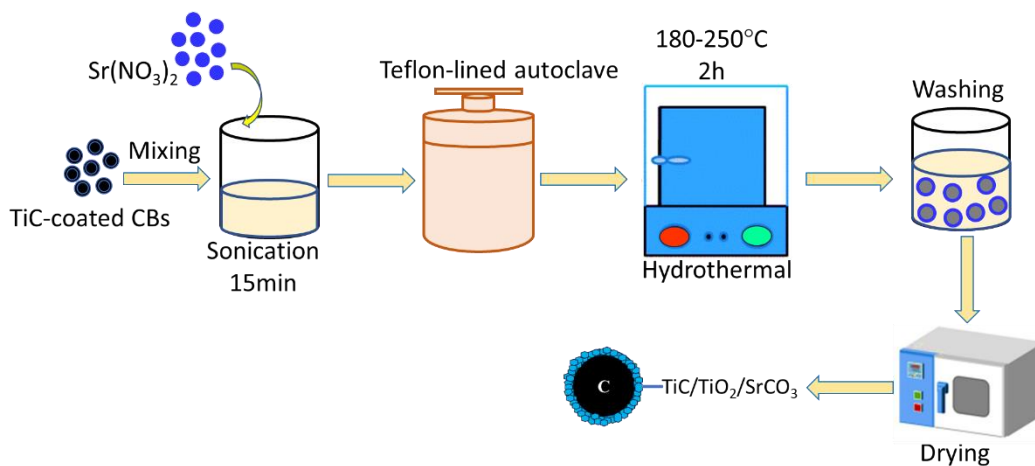


**Figure 15.** Schematic diagram of sample preparation procedure by hydrothermal method.

3. Formation mechanism of core-shell TiC/TiO<sub>2</sub>/SrCO<sub>3</sub>-coated CBs via molten salt synthesis method and hydrothermal treatment

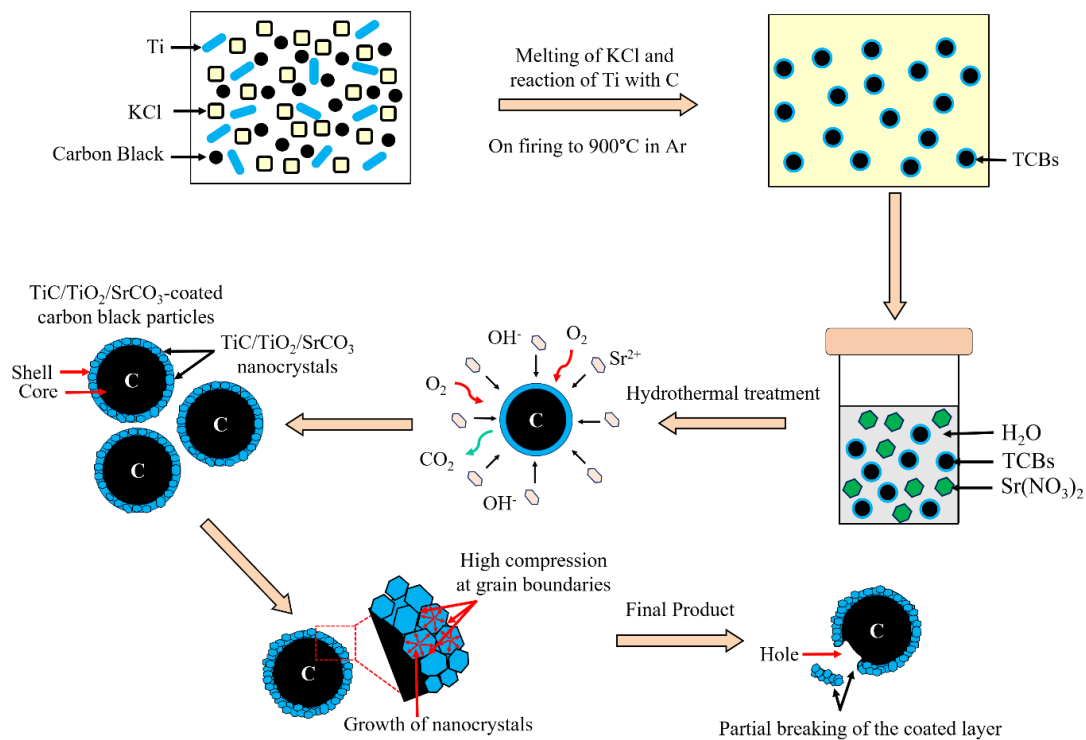


**Figure 16.** Schematic diagram of formation mechanism of the core-shell TiC/TiO<sub>2</sub>/SrCO<sub>3</sub>-coated CBs via molten salt synthesis method and hydrothermal treatment.

4. Experimental procedure for core-shell porous mixed oxide phases with TiC on CBs via calcination

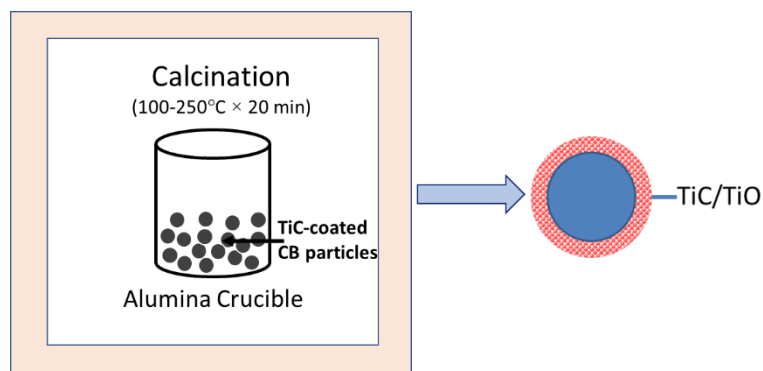


**Figure 17.** Schematic diagram of sample preparation procedure via calcination.

5. Formation mechanism of core-shell porous mixed oxide phases with TiC on CBs via calcination

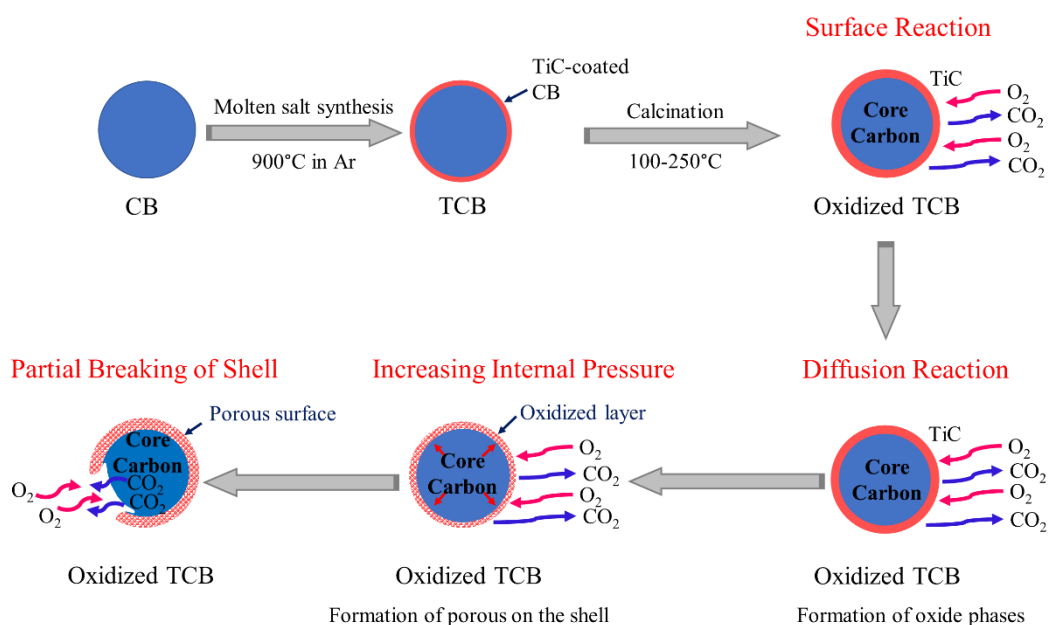


**Figure 18.** Schematic diagram of formation mechanism of core-shell porous mixed oxide phases with TiC on CBs via calcination.

## VITAE

**Name** Miss Hnin Nandar Soe

**Student ID** 6210130009

### **Educational Attainment**

<b>Degree</b>	<b>Name of Institution</b>	<b>Year of Graduation</b>
Bachelor of Engineering (Metallurgy)	Kyaukse Technological Universtiy, Myanmar	2012
Master of Engineering (Metallurgical and Materials Science)	Yangon Technological Universtiy, Myanmar	2016
Master of Engineering (Materials Engineering)	Prince of Songkla University, Thailand	2018

### **Scholarship Awards during Enrolment**

1. The National Science, Research and Innovation Fund (NSRF) and Prince of Songkla University (Grant no. ENG6505057S).
2. PSU. GS. Financial Support for Thesis (Fiscal Year 2019)

## List of Publications

- Paper 1.** Soe, H.N., Meesane, J, Kokoo, R, Khangkhamano, M. Bioactive core–shell structure of TiC/TiO<sub>2</sub>/SrCO<sub>3</sub> coating on carbon black particles for bone tissue formation: Fabrication, characterization, and biological functions. J Am Ceram Soc; Vol. 106: pp. 2689-2701, 2023. <https://doi.org/10.1111/jace.18942>
- Paper 2.** Soe, H.N., Khangkhamano, M., Meesane, J. et al. A material-based core–shell bioactive compound of mixed oxide phases with TiC on carbon black particles for bone augmentation in oral and maxillofacial surgery. Journal of Materials Research; Vol. 38: pp. 3504–3518, 2023. <https://doi.org/10.1557/s43578-023-01074-x>
- Paper 3.** Soe, H.N., Khangkhamano, M., Sangkert, S., Meesane, J. et al. TiC-coated carbon particles as bioactive substrates for inducing of mineralization in bone healing, Mater. Lett., Vol. 229: pp. 118-121, 2018. <https://doi.org/10.1016/j.matlet.2018.06.125>
- Paper 4.** Soe, H.N., Khangkhamano, M., Sangkert, S., Meesane, J. et al. TiC-coated carbon black particles as a bioactive ceramic compound for application of bone tissue engineering, , Solid State Phenomena Vol. 280: pp. 109-114, 2018. <http://dx.doi.org/10.4028/www.scientific.net/SSP.280.109>